universe

MDPI

Article

Black Hole Gravitational Phenomena in Higher-Order Curvature–Scalar Gravity

Adailton A. Araújo Filho [1,2], Narges Heidari [2,3,4] and Iarley P. Lobo [1,2,*]

[1] Departamento de Física, Universidade Federal da Paraíba, Caixa Postal 5008, João Pessoa 58051-970, Paraíba, Brazil; dilto@fisica.ufc.br
[2] Departamento de Física, Universidade Federal de Campina Grande, Caixa Postal 10071, Campina Grande 58429-900, Paraíba, Brazil; heidari.n@gmail.com
[3] Center for Theoretical Physics, Khazar University, 41 Mehseti Street, Baku AZ-1096, Azerbaijan
[4] School of Physics, Damghan University, Damghan 3671641167, Iran
* Correspondence: iarley_lobo@fisica.ufpb.br

Abstract

This work aims to explore the gravitational consequences of a recently proposed black hole solution previously introduced, which incorporates quantum gravitational corrections of General Relativity. We initiate our analyses by taking into account the horizon structure, focusing on both the event and Cauchy horizons. Subsequently, we examine the quasinormal modes by considering all types of perturbations—scalar, vector, tensor, and spinorial. To strengthen these results, we also compute the time domain for each perturbation. Next, we turn to the study of optical properties of the black hole. In particular, we investigate null geodesics, the photon sphere and its stability, and the corresponding black hole shadows. Following this, we analyze gravitational lensing phenomena in two regimes: the weak-field limit, utilizing the Gauss–Bonnet theorem, and the strong deflection limit, employing Tsukamoto's approach. In addition, we address the lensing observables with Event Horizon Telescope (EHT) data for $SgrA^*$ and $M87^*$. Finally, constraints on the parameter ξ—which is introduced by higher-order curvature–scalar gravity, thereby differing from the Schwarzschild solution—are estimated using Solar System measurements such as the precession of Mercury's orbit, gravitational light bending, and time delay (or the Shapiro effect).

Keywords: black hole; quantum gravity; modified gravity; shadows; lensing; perturbations; solar system tests

Check for updates

Academic Editor: Jose Navarro-Salas

Received: 18 May 2026
Revised: 31 July 2026
Accepted: 3 August 2026
Published: 10 August 2026

Copyright: © 2026 by the authors. Licensee MDPI, Basel, Switzerland. This article is an open access article distributed under the terms and conditions of the Creative Commons Attribution (CC BY) license.

1. Introduction

General Relativity (GR) transformed our understanding of gravity by describing it as a manifestation of spacetime curvature rather than a force acting at a distance. Its predictions have been confirmed across a broad range of astrophysical and cosmological settings, from black hole mergers to the evolution of the early Universe. Nevertheless, cosmic acceleration, the gravitational effects attributed to dark matter, and the difficulty of reconciling GR with quantum theory suggest that Einstein's description may require modification at sufficiently large or small scales [1–8]. These open questions have motivated numerous extensions of GR, including higher-curvature theories, scalar–tensor models, and alternative geometric formulations [9–12].

A common strategy is to modify the gravitational action itself. Representative examples include $f(R)$ gravity [9,13–17], $f(T)$ gravity formulated in terms of the torsion

scalar [12,18–23], and extensions such as $f(R,\mathcal{T})$ and $f(T,\mathcal{T})$, where $\mathcal{T}$ is the trace of the energy–momentum tensor [24–26]. Models based on the Gauss–Bonnet invariant, including $f(G)$ gravity, provide another important direction [27], while related constructions combining modified gravity with generalized electrodynamics have also been explored [28,29].

The motivation for these theories is closely tied to the limitations of GR in describing cosmic acceleration, galactic rotation curves, and possible exotic structures such as wormholes and modified black hole interiors [9,11,17,30]. An early influential example was Starobinsky's quadratic-curvature model of inflation [31]. Since then, $f(R)$ gravity has been widely studied in cosmology and astrophysics, including applications to massive neutron stars [32–37]. Its richer field equations admit broad classes of exact and numerical solutions and have been used to study dark-energy dynamics and cosmic evolution [11,14,38–52].

Among the higher-curvature extensions of GR, $f(R,G)$ gravity is particularly useful because it combines the Ricci scalar with the Gauss–Bonnet invariant G [53–59]. Although the Gauss–Bonnet term is topological in four dimensions, it can contribute dynamically when coupled to additional fields. The inclusion of scalar fields introduces further degrees of freedom that naturally arise in scalar–tensor theories, string-inspired models, and inflationary scenarios [9,11,17]. The resulting curvature–scalar framework therefore provides a flexible setting for investigating strong-gravity phenomena beyond GR.

A wide variety of compact-object solutions have been obtained in modified gravity. Exact vacuum solutions with spherical symmetry have been reported in $f(R)$ theories [60–64], while the Noether symmetry approach has been used to construct both spherical and axial geometries [17,65,66]. Other nontrivial black hole configurations have been obtained for specific forms of $f(R)$ [37,67], together with extensive studies of static black holes [68–74] and neutron stars [34,75–86]. Moreover, $f(R)$ gravity can be recast in a Brans–Dicke-like form with a scalar potential of geometric origin [87–91], which clarifies the role of the additional scalar degree of freedom.

More recently, Ref. [92] constructed black hole configurations in $f(R,G)$ gravity coupled to a scalar field. In this approach, the Ricci scalar, the Gauss–Bonnet invariant, and the scalar sector are incorporated into a unified framework. The resulting static and spherically symmetric geometry deforms the Schwarzschild spacetime and provides a setting in which higher-curvature and scalar-field effects can be studied explicitly [93,94].

Recent observational advances have also turned black holes into powerful laboratories for testing gravity. The first direct detections of gravitational waves by the LIGO and Virgo collaborations opened a new window onto compact-object mergers [95], while the Event Horizon Telescope provided horizon-scale images of the supermassive black holes in $M87$ and $SgrA^*$ [5,6]. These developments extend tests of gravity beyond the traditional weak-field domain [96–98] and make the strong-field region particularly relevant for probing modifications of GR and additional matter sectors, including nonlinear electrodynamics [29,99,100].

Black hole shadows provide one of the most direct probes of the near-horizon geometry. They arise from the capture and strong deflection of photons near the unstable photon region, producing a dark silhouette against the surrounding emission. Early theoretical studies date back to Bardeen [101] and were later developed by Falcke, Melia, and Agol [102]. The observations of $M87^*$ and $SgrA^*$ have since motivated numerous studies testing modified black hole geometries against observational data [103–120].

Gravitational lensing offers a complementary probe. The formulation developed by Virbhadra and Ellis enabled the study of highly deflected images around asymptotically flat black holes [121,122] and provided the basis for later investigations of relativistic images and strong lensing [123–125]. The subject has since been extended to a broad range of spacetimes [126–130], including black holes in modified gravity [131–135] and geometries

with nontrivial topology [136–142]. Recent work has also emphasized image distortions and the extraction of physical information from strong-lensing observables [143].

Perturbations provide another sensitive probe of black hole geometry. Following a disturbance, a black hole undergoes damped oscillations described by quasinormal modes [144–150]. The real part of the complex frequency determines the oscillation rate, whereas the imaginary part governs the damping time. Quasinormal modes therefore encode characteristic information about the spacetime and are closely related to both the shadow and the greybody spectrum [151–153]. Although tentative evidence for their direct detection has been reported, its statistical significance remains sensitive to uncertainty treatment [154].

In this work, we investigate the physical properties of the black hole geometry introduced in Ref. [92] within higher-order curvature–scalar gravity. We first determine the event and Cauchy horizons and examine their dependence on the deformation parameter ξ. We then study null geodesics, the photon sphere, and the black hole shadow, comparing the predicted shadow size with Event Horizon Telescope observations of $SgrA^*$ and $M87^*$.

The dynamical response of the spacetime is examined through scalar, vector, tensor, and spinor perturbations. We derive the corresponding effective potentials and calculate the quasinormal frequencies using the WKB method, supplemented by time-domain profiles. Gravitational lensing is studied in both weak- and strong-field regimes using the Gauss–Bonnet and Tsukamoto approaches, respectively. Finally, the parameter ξ is constrained using Solar System tests, including Mercury's perihelion advance, solar light deflection, and the Shapiro time delay.

2. Higher-Order Curvature Gravity with a Scalar Field

We briefly review the theoretical framework underlying the black hole geometry studied in this work. Following Ref. [92], we consider an extension of General Relativity in which the gravitational action depends on the Ricci scalar R and the Gauss–Bonnet invariant G. Rather than working with a completely general function $f(R, G)$, the theory is written in the separable form

$$f(R, G) = f(R) + f_1(G).$$

The Gauss–Bonnet sector can then be represented through a scalar field ϕ_1 coupled to G by a function $H(\phi_1)$. This formulation provides a convenient way to describe the additional degrees of freedom associated with the higher-curvature sector and has been discussed in Refs. [58,155,156].

The action in a D-dimensional spacetime is

$$S = \int \mathrm{d}^D x \sqrt{-g}\left[\frac{1}{2\kappa^2} f(R) - \frac{1}{2}\partial_\mu \phi_1 \partial^\mu \phi_1 + V(\phi_1) + H(\phi_1) G\right], \tag{1}$$

where $V(\phi_1)$ is the scalar-field potential and

$$G = R^2 - 4R_{\mu\nu}R^{\mu\nu} + R_{\mu\nu\rho\sigma}R^{\mu\nu\rho\sigma} \tag{2}$$

is the Gauss–Bonnet invariant. Although the integral of G is topological in four dimensions, the coupling $H(\phi_1)G$ contributes nontrivially to the dynamics whenever $H(\phi_1)$ is not constant. In other words, it is the scalar-dependent coupling that activates the Gauss–Bonnet sector in four-dimensional spacetime. Matter fields are assumed to couple minimally to the metric and not directly to ϕ_1, thereby avoiding an additional long-range interaction.

Varying the action with respect to the scalar field gives

$$\nabla^2\phi_1 - V'(\phi_1) + H'(\phi_1)G = 0. \tag{3}$$

Variation with respect to $g_{\mu\nu}$ produces the modified gravitational field equations. These equations contain the usual $f(R)$ contributions together with terms arising from the scalar kinetic sector, its potential, and derivatives of the coupling function $H(\phi_1)$. Since our purpose is to investigate the physical properties of the resulting black hole rather than to reproduce its full derivation, one can refer to the complete form, together with the required Bianchi identities and the corresponding trace equation given in Ref. [92].

An important limiting case follows when the scalar–Gauss–Bonnet coupling is constant. In that situation, the Gauss–Bonnet contribution reduces to a boundary term and drops out of the four-dimensional field equations. The nontrivial corrections considered in the following arise from the radial variation in the scalar sector and its coupling to the curvature.

2.1. Static and Spherically Symmetric Configuration

We now restrict the theory to a static and spherically symmetric spacetime, described by

$$\mathrm{d}s^2 = -D_1(r)\mathrm{d}t^2 + \frac{\mathrm{d}r^2}{D_2(r)} + r^2\left(\mathrm{d}\theta^2 + \sin^2\theta\,\mathrm{d}\phi^2\right). \tag{4}$$

Here, $D_1(r)$ and $D_2(r)$ are independent metric functions. The Ricci scalar corresponding to Equation (4) is

$$R = \frac{r^2D_2D_1'^2 - r^2D_1D_1'D_2' - 2r^2D_1D_2D_1'' - 4rD_1\left(D_2D_1' - D_1D_2'\right) + 4D_1^2(1-D_2)}{2r^2D_1^2}, \tag{5}$$

where a prime denotes differentiation with respect to r.

After imposing spherical symmetry, the modified field equations reduce to a system of radial differential equations involving

$$D_1(r),\ D_2(r),\ F(r) = f_R,\ H(r),\ \text{and}\ \phi_1(r).$$

Excluding the trace relation, only three independent equations remain for these five unknown functions. The system is therefore underdetermined, and two additional choices are required to close it.

Ref. [92] follows a reconstruction approach. Instead of fixing $f(R)$, $H(\phi_1)$, and $V(\phi_1)$ in advance and then solving for the geometry, one first specifies the two metric functions. The remaining functions of the theory are subsequently reconstructed from the modified field equations. In this sense, the resulting geometry is not introduced independently of the gravitational model: it is supported by a definite scalar profile, curvature coupling, gravitational function, and potential determined by the field equations.

The general relativistic limit is recovered when the additional curvature and scalar contributions are switched off. In this case, the gravitational Lagrangian reduces to $f(R) = R$, and the two metric functions coincide with the Schwarzschild form as $D_1(r) = D_2(r) = 1 - \frac{2M}{r}$. Nonzero contributions from the higher-curvature and scalar sectors therefore generate departures from the Schwarzschild geometry, which will be discussed below.

2.2. Black Hole Solution

After imposing static spherical symmetry, the reduced field equations involve five unknown radial functions, $D_1(r)$, $D_2(r)$, $F(r) = f_R$, $H(r)$, and $\phi_1(r)$, whereas only three independent differential equations remain after excluding the trace relation. The system is therefore underdetermined and requires two additional conditions.

Following the reconstruction approach of Ref. [92], the metric functions $D_1(r)$ and $D_2(r)$ are specified first, while the scalar profile and the functions defining the underlying gravitational theory are subsequently reconstructed from the reduced field equations. The adopted ansatz describes a deformation of the Schwarzschild geometry controlled by the parameter ξ, with the Schwarzschild solution recovered smoothly in the limit $\xi \to 0$. In particular, Ref. [92] considered

$$D_1(r) = 1 - \frac{c}{r} + \frac{\xi}{r^2}, \qquad D_2(r) = 1 - \frac{c}{r} + \frac{c,\xi^{3/2}}{r^4}, \tag{6}$$

where $c = 2M$ is associated with the gravitational mass, while ξ has dimensions of length squared and measures the departure from the Schwarzschild spacetime.

Once Equation (6) is substituted into the reduced field equations, the corresponding functions $F(r) = f_R$, $H(r)$, $\phi_1(r)$, $f(r)$, and $V(r)$ can be reconstructed consistently. Their explicit forms contain lengthy nested expressions and are reported in Ref. [92]. The reconstructed scalar field must also satisfy the associated reality condition; otherwise, the resulting branch would contain ghost-like degrees of freedom.

The solution is static, spherically symmetric, and asymptotically flat. Moreover, the Schwarzschild geometry is recovered smoothly in the limit $\xi \to 0$. The correction terms decay more rapidly than the Schwarzschild mass term, so their effects are expected to be most relevant in the strong-field region. The different radial orders appearing in $D_1(r)$ and $D_2(r)$ should not be regarded as unrelated phenomenological corrections. They characterize the two independent metric functions permitted by spherical symmetry, while the remaining quantities of the theory are reconstructed so that the complete configuration satisfies the modified field equations.

In the present work, we take this reconstructed solution as the background geometry and investigate its causal, perturbative, and optical properties.

3. The Black Hole Spacetime

Using $c = 2M$, the solution in Equation (6) is written as

$$\mathrm{d}s^2 = -\left(1 - \frac{2M}{r} + \frac{\xi}{r^2}\right)\mathrm{d}t^2 + \frac{\mathrm{d}r^2}{1 - \frac{2M}{r} + \frac{2M\xi^{3/2}}{r^4}} + r^2\left(\mathrm{d}\theta^2 + \sin^2\theta\,\mathrm{d}\phi^2\right). \tag{7}$$

For convenience, we define

$$A(r,\xi) \equiv 1 - \frac{2M}{r} + \frac{\xi}{r^2}, \tag{8}$$

and

$$B(r,\xi) \equiv 1 - \frac{2M}{r} + \frac{2M\xi^{3/2}}{r^4}. \tag{9}$$

The temporal metric function $A(r,\xi)$ resembles that of the Reissner–Nordström spacetime under the formal identification

$$\xi \leftrightarrow Q^2.$$

This resemblance concerns only the radial form of the metric component, since ξ represents a higher-curvature deformation rather than an electric charge. In contrast, the radial function

$B(r,\xi)$ shows a close analogy with Loop Quantum Gravity-inspired black holes [157,158] under the formal correspondence

$$\alpha G^2 M^2 \leftrightarrow 2M\xi^{3/2}, \tag{10}$$

where

$$\alpha = 16\sqrt{3}\,\pi\,\gamma^3 l_P, \tag{11}$$

with l_P denoting the Planck length and γ the Barbero–Immirzi parameter.

The geometry therefore combines an RN-like temporal component with an LQG-inspired radial component. Nevertheless, both corrections originate from the same higher-order curvature–scalar construction and are governed by the single parameter ξ. Since $A(r,\xi)$ and $B(r,\xi)$ have different radial dependences, they can affect the causal structure, perturbative dynamics, and optical behavior of the spacetime in distinct ways. These effects are examined in the following sections.

To begin, we examine the event horizon r_h. It is determined by imposing $1/g_{rr} = 0$ and solving the resulting equation. This, therefore, yields

$$\begin{aligned} r_h = \frac{M}{2} &+ \frac{1}{2}\sqrt{\left(\frac{2}{3}\right)^{2/3}\sqrt[3]{\eta} + M^2 + \frac{4\sqrt[3]{\frac{2}{3}}M\xi^{3/2}}{\sqrt[3]{\eta}}} \\ &+ \frac{1}{2}\sqrt{-\left(\frac{2}{3}\right)^{2/3}\sqrt[3]{\eta} + 2M^2 + \frac{2M^3}{\sqrt{\left(\frac{2}{3}\right)^{2/3}\sqrt[3]{\eta} + M^2 + \frac{4\sqrt[3]{\frac{2}{3}}M\xi^{3/2}}{\sqrt[3]{\eta}}}} - \frac{4\sqrt[3]{\frac{2}{3}}M\xi^{3/2}}{\sqrt[3]{\eta}}} \\ &\approx 2M - \frac{\xi^{3/2}}{4M^2}. \end{aligned} \tag{12}$$

For the above short notation, we assumed ξ to be small; here, $\eta \equiv 9M^3\xi^{3/2} + \sqrt{81M^6\xi^3 - 96M^3\xi^{9/2}}$. As will be shown in the following sections, the assumption that ξ is small is fully supported by the bounds derived in the final section of the manuscript. Notably, the horizon radius r_h in this case is smaller than in the Schwarzschild solution. Since ξ carries dimensions of $[\mathrm{L}^2]$, it must be strictly positive; otherwise, r_h would become imaginary, as is it straightforwardly verified from Equation (12).

To corroborate our results, we examine their behavior for different configurations of ξ and the mass M. For this purpose, we provide both a plot and a table to offer qualitative and quantitative perspectives. Figure 1 illustrates the dependence of the event horizon r_h on the mass M for various values of the deformed parameter ξ, while Table 1 reports the corresponding quantitative values for different choices of M and ξ. In general lines, this latter parameter tends to decrease the magnitude of the event horizon, as anticipated by the shape of Equation (12).

Another finding is worth pointing out: besides the solution ascribed to the event horizon, there also exists another one (real and positive definite), which is related to the Cauchy horizon, r_{cau}:

$$r_{\mathrm{cau}} \approx \sqrt{\xi} + \frac{\xi}{6M} + \frac{\xi^{3/2}}{12M^2}. \tag{13}$$

Unlike the behavior of r_h, the Cauchy horizon r_{cau} increases as either ξ or M increases, as shown in Figure 2 and Table 2.

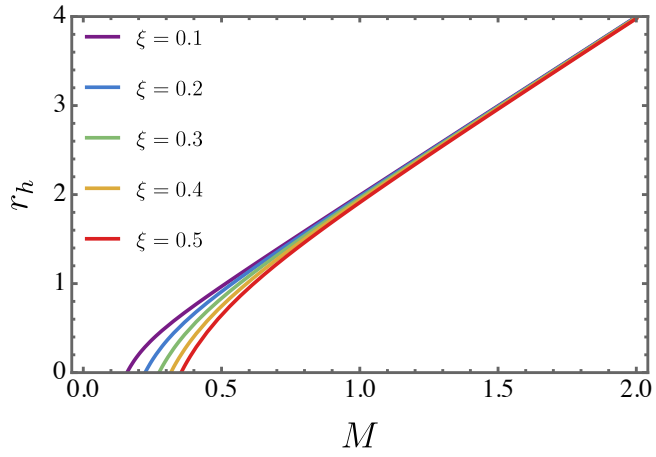

Figure 1. The dependence of the event horizon r_h on the mass M is illustrated for various configurations of the deformed parameter ξ.

Table 1. The quantitative values of the event horizon are presented for several configurations of M and ξ.

ξ	M	r_h	ξ	M	r_h
0.1	1.0	1.99209	0.1	1.1	2.19347
0.2	1.0	1.97764	0.1	1.2	2.39451
0.3	1.0	1.95892	0.1	1.3	2.59532
0.4	1.0	1.93675	0.1	1.4	2.79597
0.5	1.0	1.91161	0.1	1.5	2.99649

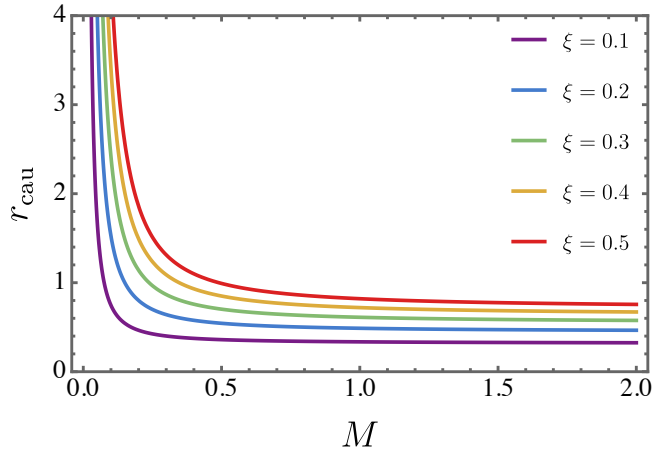

Figure 2. The behavior of the Cauchy horizon $r_{\rm cau}$ as a function of the mass M is shown for different configurations of the deformed parameter ξ.

Table 2. Table reporting the numerical values of the Cauchy horizon $r_{\rm cau}$ corresponding to various choices of M and ξ.

ξ	M	$r_{\rm cau}$	ξ	M	$r_{\rm cau}$
0.1	1.0	0.33553	0.1	1.1	0.333557
0.2	1.0	0.48800	0.1	1.2	0.331947
0.3	1.0	0.611416	0.1	1.3	0.330608
0.4	1.0	0.720204	0.1	1.4	0.329477
0.5	1.0	0.819903	0.1	1.5	0.328510

Domain Where the Spacetime Is a Black Hole

The existence of a black hole structure in the present geometry is determined by the behavior of the radial metric function $B(r,\xi)$, since the horizon locations follow from the condition $g_{rr}^{-1} = B(r,\xi) = 0$. Using the explicit form of the metric, this condition leads to

$$B(r,\xi) = 1 - \frac{2M}{r} + \frac{2M\xi^{3/2}}{r^4} = 0. \tag{14}$$

Introducing the dimensionless variables $x = r/M$ and $z = \xi/M^2$, the horizon equation can be rewritten as

$$x^4 - 2x^3 + 2z^{3/2} = 0. \tag{15}$$

For a given value of z, the spacetime represents a black hole if this equation admits at least one real and positive root. When two such roots exist, the larger one corresponds to the event horizon r_h, while the smaller one defines the Cauchy horizon r_{cau}.

By solving this equation numerically, one finds that the black hole configuration persists within a finite interval of the deformation parameter ξ. In particular, the existence of real and positive horizons requires

$$0 \leq \frac{\xi}{M^2} \leq \left(\frac{351}{256}\right)^{2/3}, \tag{16}$$

within which the condition $r_h > 0$ is always satisfied. In this domain, the spacetime maintains a well-defined black hole structure with $r_h > r_{cau}$. Outside this interval, the horizons cease to exist as real solutions, and the geometry no longer represents a black hole.

In the perturbative regime $\xi \ll 1$, the exact numerical solution for the event horizon smoothly reduces to the approximate expression

$$r_h \approx 2M - \frac{\xi^{3/2}}{4M^2}, \tag{17}$$

which is the form adopted for the sake of a more compact notation.

4. Quasinormal Mode Spectra

This section is devoted to the study of quasinormal oscillations of the black hole background. The analysis is performed for a wide range of perturbations, including scalar, vector, tensor, and spinor fields. The procedure begins with the field equations in the curved geometry, which are decomposed through a separation of variables to yield the radial master equations. From these, the effective potential associated with each perturbing field is identified. The resulting Schrödinger-like equations are then solved by applying the WKB approximation, allowing, therefore, the computation of the complex quasinormal frequencies that characterize the dissipative response of the spacetime.

4.1. Scalar Field Fluctuations

One of the most commonly used techniques for calculating quasinormal mode spectra is the Wentzel–Kramers–Brillouin (WKB) method. This semi-analytic approach, first developed by Will and Iyer [159,160] and, after that, generalized to higher orders by Konoplya [161], provided a reliable way to approximate the solutions by taking into account their perturbation versions. In the present investigation, we focus on scalar field fluctuations and examine the propagation of the Klein–Gordon field for the metric tensor of Equation (7). Solving the resulting radial equation within this framework yields the complex quasinor-

mal frequencies that encode the characteristic damped oscillations of the system. To do so, let us, initially, start with

$$\frac{1}{\sqrt{-g}}\partial_\mu(g^{\mu\nu}\sqrt{-g}\,\partial_\nu\phi)=0. \tag{18}$$

At this point, it is important to mention that while the inclusion of backreaction effects would bring about a more complete description of the system, such contributions lie beyond the scope of this work. Here, the scalar field is regarded purely as a probe, evolving on a fixed spacetime geometry without influencing the background metric. Under this assumption, the dynamics reduce to Equation (18), which serves as the master equation of such a field, therefore governing its corresponding evolution. In other words, Equation (18) can be decomposed as

$$\begin{aligned}&-\frac{1}{\left(1-\frac{2M}{r}+\frac{\xi}{r^2}\right)}\frac{\partial^2\phi}{\partial t^2}+\frac{1}{r^2}\left\{\frac{\partial}{\partial r}\left[\left(1-\frac{2M}{r}+\frac{2M\xi^{3/2}}{r^4}\right)r^2\frac{\partial\phi}{\partial r}\right]\right\}\\&+\frac{1}{r^2\sin\theta}\left[\frac{\partial}{\partial\theta}\left(\sin\theta\frac{\partial}{\partial\theta}\phi\right)\right]+\frac{1}{r^2\sin^2\theta}\frac{\partial^2\phi}{\partial\varphi^2}=0.\end{aligned} \tag{19}$$

Taking advantage of the spherical symmetry of the spacetime, the scalar field can be expanded into angular and radial parts through a variable separation procedure. This step transforms the field equation into an ordinary differential equation for the radial component. To achieve this, we write

$$\phi(t,r,\theta,\varphi)=\sum_{\ell=0}^{\infty}\sum_{m=-\ell}^{\ell}\mathcal{Y}_{\ell m}(\theta,\varphi)\frac{e^{-i\omega t}\psi(r)}{r}. \tag{20}$$

By taking into account the above expression and expressing the angular part via the spherical harmonics $\mathcal{Y}_{\ell m}(\theta,\varphi)$, the field equation simplifies considerably.

Moreover, considering the tortoise coordinate defined as $r^*=1/\sqrt{A(r,\xi)B(r,\xi)}$, the system simplifies to a single radial equation that admits a Schrödinger-like representation as follows:

$$\frac{\partial^2\psi}{\partial r^{*2}}-\left[\omega^2-\mathcal{V}^s(r,\ell,\xi)\right]\psi=0. \tag{21}$$

where the effective potential reads the following expression:

$$\begin{aligned}\mathcal{V}^s(r,\ell,\xi)&=A(r,\xi)\left[\frac{\ell(\ell+1)}{r^2}+\frac{1}{r\sqrt{A(r,\xi)B(r,\xi)^{-1}}}\frac{\mathrm{d}}{\mathrm{d}r}\sqrt{A(r,\xi)B(r,\xi)}\right]\\&=\frac{(-2Mr+\xi+r^2)\left(\frac{\ell(\ell+1)}{r^2}+\frac{M^2\left(10\xi^{3/2}r-4r^4\right)+M\left(3\xi+2r^2\right)\left(r^3-2\xi^{3/2}\right)+\xi\left(-r^4\right)}{r^6\sqrt{\frac{-2Mr+\xi+r^2}{2M\left(\xi^{3/2}-r^3\right)+r^4}}\sqrt{(-2Mr+\xi+r^2)\left(2M\left(\xi^{3/2}-r^3\right)+r^4\right)}}\right)}{r^2}.\end{aligned} \tag{22}$$

In the limit $\xi\to 0$, we recover the familiar Schwarzschild result for the potential, as expected. Figure 3 shows the behavior of $\mathcal{V}^s(r,\ell,\xi)$ plotted against r for a variety of multipole numbers, ℓ and ξ. Increasing ξ (or ℓ) leads to a taller potential barrier. This behavior has a direct impact on the resulting quasinormal mode spectrum and also affects the time-domain profiles, as will be demonstrated in the following analysis. It is also worth noting that, due to the asymptotically flat nature of the spacetime, the potential vanishes as $r\to\infty$.

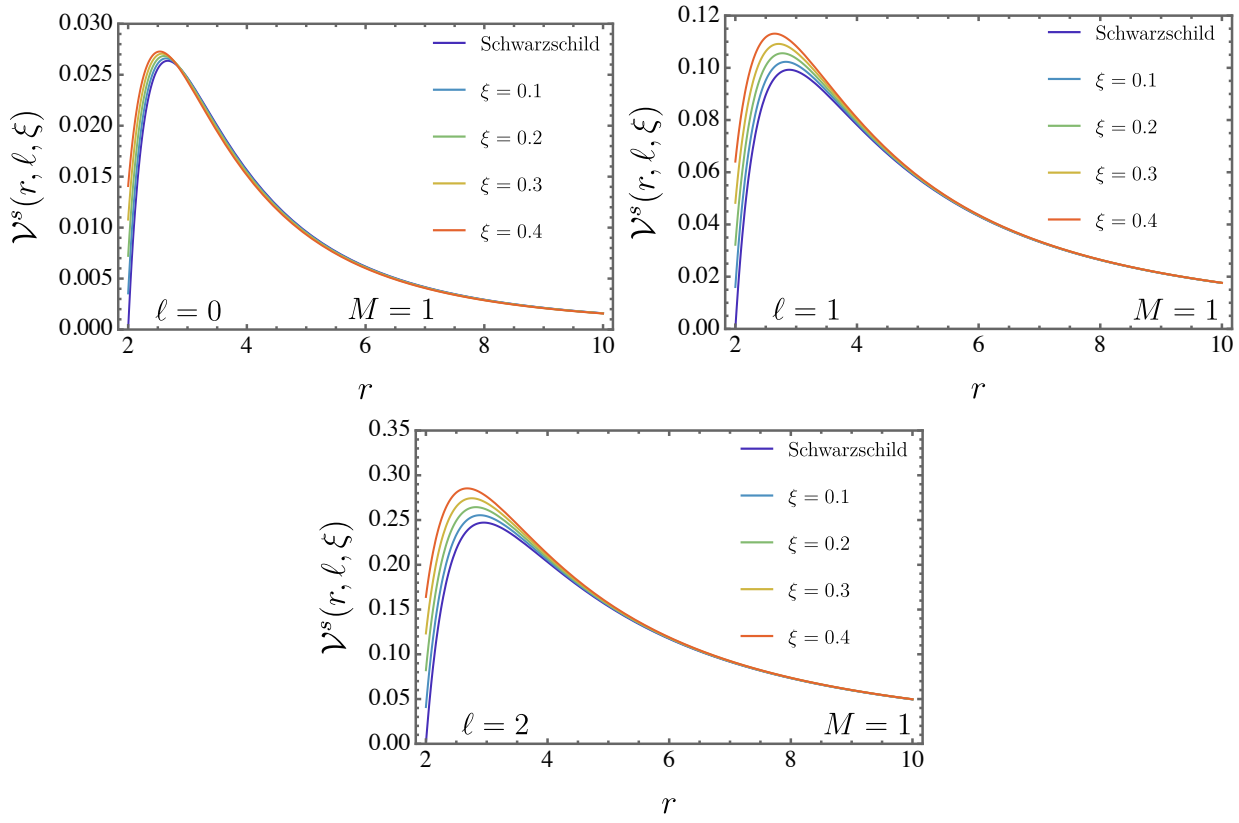

Figure 3. The behavior of the scalar potential $\mathcal{V}^s(r, \ell, \xi)$ is presented as a function of radial coordinate r, exploring various combinations of parameter ξ and the multipole number ℓ to highlight how both quantities influence its overall shape and amplitude.

The quasinormal mode spectrum is obtained by constructing the solution in the vicinity of the maximum of the effective potential, which naturally plays an essential role in identifying the classical turning points. Expanding the wave function around this peak and applying a WKB matching procedure leads to a semi-analytic expression for the complex frequencies that describe black hole ringdown. Using Konoplya's higher-order extension of the WKB method, the frequencies satisfy

$$\frac{i(\omega^2 - V_0)}{\sqrt{-2V_0''}} - \sum_{j=2}^{6} \Lambda_j = n + \frac{1}{2}, \tag{23}$$

where V_0'' is the second derivative of the potential evaluated at its maximum r_0. The term Λ_j represents successive higher-order corrections, constructed from V_0 and its derivatives, and is crucial for improving the precision of the computed quasinormal frequencies.

For clarity, we quantify the shift in the quasinormal frequencies from the Schwarzschild case by defining the relative deviations of their real and imaginary parts as

$$\Delta\omega_{R/I} = \frac{|\omega_{R/I}^{Sch}| - |\omega_{R/I}(\xi)|}{|\omega_{R/I}^{Sch}|} \times 100 \tag{24}$$

where the subscripts R and I refer to the real and imaginary parts, respectively, while $\omega_{R/I}^{Sch}$ denotes the corresponding Schwarzschild value obtained at $\xi = 0$.

Figure 3 illustrates the scalar potential $\mathcal{V}^s(r, \ell, \xi)$ plotted against the radial coordinate r for several combinations of ℓ and ξ. The figure reveals that larger values of either parameter lead to a taller and broader potential barrier, effectively shifting the corresponding peak. Since the background spacetime is asymptotically flat, as expected, the potential smoothly

decays to zero as $r \to \infty$. Complementing this analysis, Table 3 lists the quasinormal frequencies obtained for a range of ξ, and ℓ. Moreover, the real and imaginary relative deviations are shown in Figure 4. Across all cases studied, the data indicate that increasing ξ systematically increases the wave frequency and reduces the damping rate, leading to longer-lived oscillations.

Table 3. The quasinormal mode spectra related to scalar perturbations for the case $\ell = 1, 2, 3$ and corresponding overtone number n presented as a function of the deformation parameter ξ.

		$\xi = 0.0$	$\xi = 0.1$	$\xi = 0.2$	$\xi = 0.3$
$l = 1$	$n = 0$	$0.291114 - 0.0980014i$	$0.291622 - 0.0979666i$	$0.293090 - 0.0977933i$	$0.295561 - 0.0974385i$
	$n = 1$	$0.262212 - 0.307432i$	$0.262885 - 0.307234i$	$0.264517 - 0.306600i$	$0.267050 - 0.305436i$
$l = 2$	$n = 0$	$0.483211 - 0.0968049i$	$0.484038 - 0.0967998i$	$0.486499 - 0.0966682i$	$0.490690 - 0.0963572i$
	$n = 1$	$0.463192 - 0.295810i$	$0.464180 - 0.295743i$	$0.466838 - 0.295273i$	$0.471194 - 0.294259i$
	$n = 2$	$0.431660 - 0.503433i$	$0.432887 - 0.503228i$	$0.435819 - 0.502352i$	$0.440370 - 0.500605i$
$l = 3$	$n = 0$	$0.675206 - 0.0965121i$	$0.676351 - 0.0965133i$	$0.679793 - 0.0963893i$	$0.685676 - 0.0960846i$
	$n = 1$	$0.660414 - 0.292344i$	$0.661691 - 0.292318i$	$0.665302 - 0.291903i$	$0.671340 - 0.290940i$
	$n = 2$	$0.634839 - 0.494118i$	$0.636336 - 0.494004i$	$0.640215 - 0.493225i$	$0.646474 - 0.491541i$
	$n = 3$	$0.602182 - 0.701053i$	$0.603949 - 0.700803i$	$0.608158 - 0.699626i$	$0.614683 - 0.697225i$

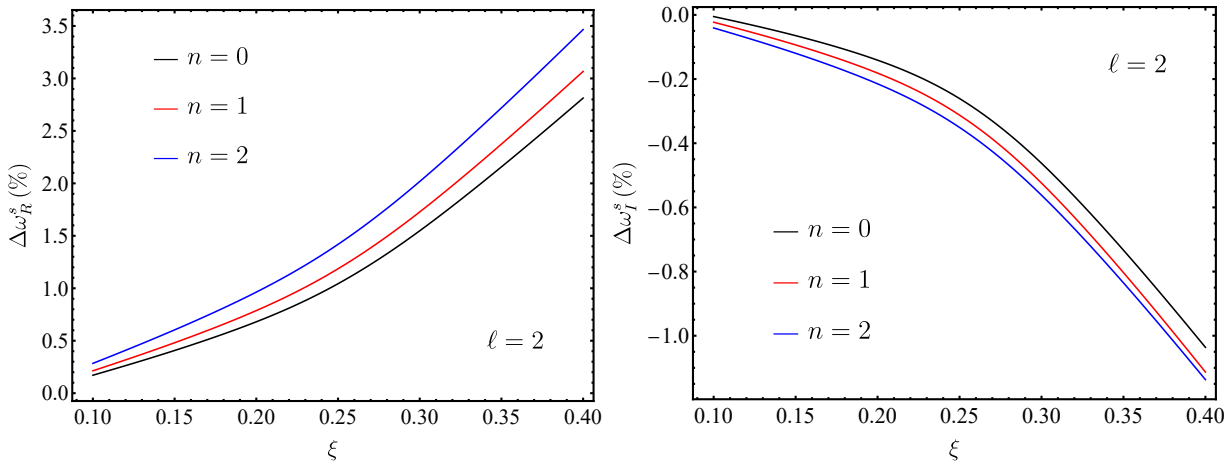

Figure 4. Relative percentage deviations of the real (left panel) and imaginary (right panel) parts of the scalar quasinormal frequencies from their Schwarzschild values are shown as functions of ξ for $\ell = 2$ and corresponding overtones.

4.2. Vector Field Fluctuations

The electromagnetic perturbations are analyzed within the tetrad formalism, following Refs. [162–164]. We introduce a set of tetrad vectors e^a_μ adapted to the background metric $g_{\mu\nu}$, satisfying

$$\begin{aligned} e^a_\mu e^\mu_b &= \delta^a_b, \qquad e^a_\mu e^\nu_a = \delta^\nu_\mu, \\ e^a_\mu &= g_{\mu\nu}\eta^{ab}e^\nu_b, \qquad g_{\mu\nu} = \eta_{ab}e^a_\mu e^b_\nu = e_{a\mu}e^a_\nu. \end{aligned} \tag{25}$$

Applying the Bianchi identity,

$$\mathcal{F}_{[ab|c]} = 0,$$

to the electromagnetic field-strength tensor gives

$$\left(r\sqrt{A(r,\xi)}\,\mathcal{F}_{t\phi}\right)_{,r}+r\sqrt{B(r,\xi)}\,\mathcal{F}_{\phi r,t}=0, \tag{26}$$

$$\left(r\sqrt{A(r,\xi)}\,\mathcal{F}_{t\phi}\sin\theta\right)_{,\theta}+r^2\sin\theta\,\mathcal{F}_{\phi r,t}=0. \tag{27}$$

The corresponding source-free Maxwell equation is

$$\eta^{bc}(\mathcal{F}_{ab})_{|c}=0. \tag{28}$$

Here, the vertical bar denotes the covariant derivative in the tetrad frame, while the comma indicates differentiation along the corresponding tetrad direction. The antisymmetrization is defined as

$$\mathcal{F}_{[ab|c]}=\mathcal{F}_{ab|c}+\mathcal{F}_{bc|a}+\mathcal{F}_{ca|b}.$$

In spherical polar coordinates, the relevant Maxwell equation becomes

$$\left(r\sqrt{A(r,\xi)}\,\mathcal{F}_{\phi r}\right)_{,r}+\sqrt{A(r,\xi)B(r,\xi)}\,\mathcal{F}_{\phi\theta,\theta}+r\sqrt{B(r,\xi)}\,\mathcal{F}_{t\phi,t}=0. \tag{29}$$

Taking the time derivative of Equation (29) and using Equations (26) and (27), we obtain

$$\begin{aligned}&\left[\sqrt{A(r,\xi)B(r,\xi)^{-1}}\left(r\sqrt{A(r,\xi)}\,\mathcal{F}\right)_{,r}\right]_{,r}\\&+\frac{A(r,\xi)\sqrt{B(r,\xi)}}{r}\left(\frac{\mathcal{F}_{,\theta}}{\sin\theta}\right)_{,\theta}\sin\theta-r\sqrt{B(r,\xi)}\,\mathcal{F}_{,tt}=0.\end{aligned} \tag{30}$$

We then define

$$F\equiv\mathcal{F}_{t\phi}\sin\theta$$

and perform a Fourier decomposition in time, $\partial_t\to-i\omega$. The angular dependence is separated as

$$F(r,\theta)=F(r)\frac{Y_{,\theta}}{\sin\theta},$$

where $Y(\theta)$ is the Gegenbauer function [164–170], satisfying

$$\frac{1}{\sin\theta}\frac{\mathrm{d}}{\mathrm{d}\theta}\left(\sin\theta\frac{\mathrm{d}Y}{\mathrm{d}\theta}\right)+\ell(\ell+1)Y=0. \tag{31}$$

With these definitions, Equation (30) reduces to

$$\begin{aligned}&\left[\sqrt{A(r,\xi)B(r,\xi)^{-1}}\left(r\sqrt{A(r,\xi)}\,F\right)_{,r}\right]_{,r}\\&+\omega^2r\sqrt{B(r,\xi)}\,F-\frac{A(r,\xi)\sqrt{B(r,\xi)}}{r}\ell(\ell+1)F=0.\end{aligned} \tag{32}$$

Finally, introducing the master variable

$$\psi^{\mathrm{vec}}=r\sqrt{A(r,\xi)}\,F,$$

and the tortoise coordinate r^*, Equation (32) can be written in the Schrödinger-like form

$$\partial_{r_*}^2 \psi^{\text{vec}} + \omega^2 \psi^{\text{vec}} = \mathcal{V}^v(r, \ell, \xi)\psi^{\text{vec}}, \tag{33}$$

where

$$\mathcal{V}^v(r, \ell, \xi) = A(r, \xi)\frac{\ell(\ell+1)}{r^2}. \tag{34}$$

Figure 5 displays the vector perturbation potential $\mathcal{V}^v(r, \ell, \xi)$ as a function of r, explicitly comparing multiple values of ℓ and ξ. The plot clearly shows that increasing either the ξ or ℓ parameter increases the potential barrier. Another important observation is that, because the spacetime treated here is asymptotically flat, the potential approaches zero in the limit $r \to \infty$. In addition, Table 4 presents the quasinormal frequencies for different choices of ξ and ℓ. Furthermore, the real and imaginary relative deviations demonstrated in Figure 6 show that for all vector perturbation cases considered ($\ell = 1, 2, 3$ with the corresponding overtones), increasing ξ leads to a monotonic increase in the oscillation frequency (ω_R) and a decrease in the damping rate ($|\omega_I|$), resulting in longer-lived ringdown modes.

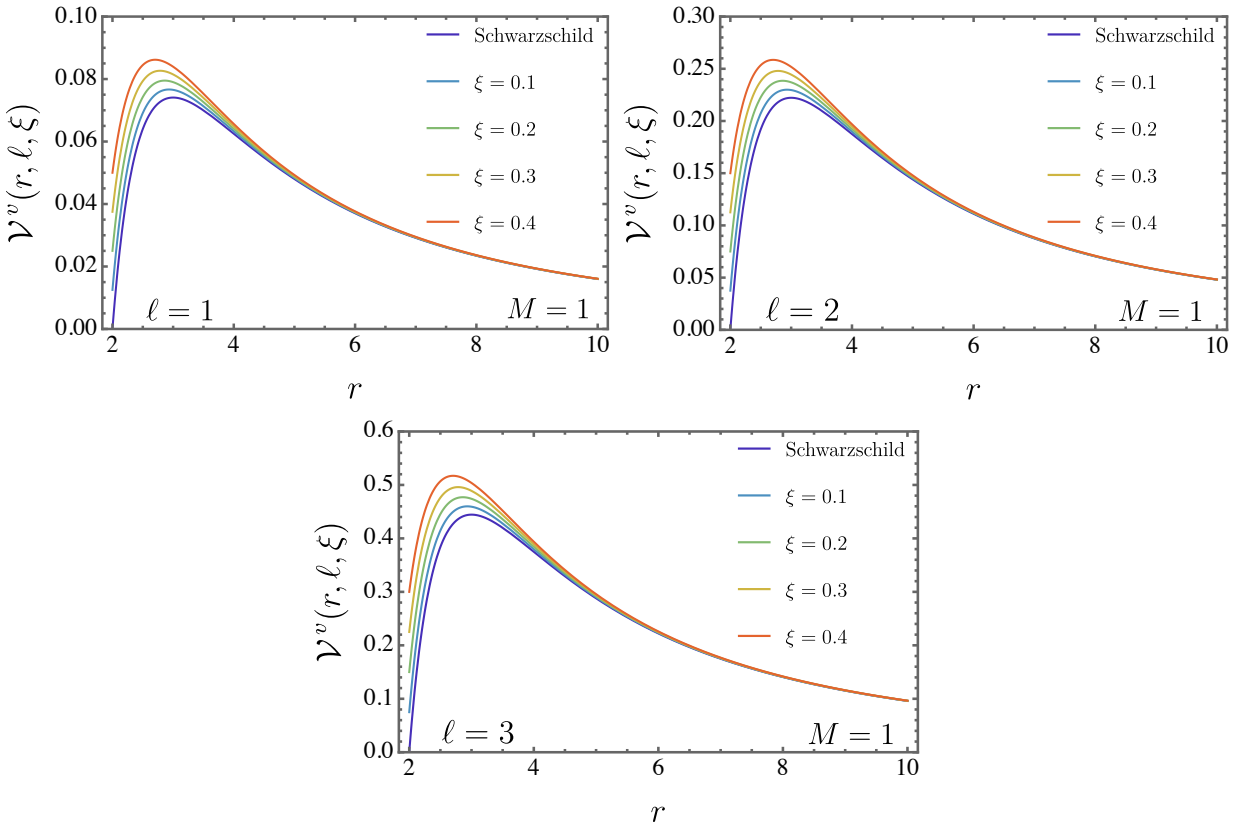

Figure 5. The profile of the vector perturbation potential $\mathcal{V}^v(r, \ell, \xi)$ is shown as a function of the radial coordinate r, considering different values of ℓ and ξ to illustrate how these parameters affect both the height and structure of the potential barrier.

Table 4. The table presents the quasinormal mode spectra regarding vector fluctuations with $\ell = 1, 2, 3$, highlighting how these modes change as the parameter ξ varies. The mass is fixed at $M = 1$.

		$\xi = 0.0$	$\xi = 0.1$	$\xi = 0.2$	$\xi = 0.3$
$l = 1$	$n = 0$	$0.291114 - 0.0980014i$	$0.291622 - 0.0979666i$	$0.293090 - 0.0977933i$	$0.295561 - 0.0974385i$
	$n = 1$	$0.262212 - 0.307432i$	$0.262885 - 0.307234i$	$0.264517 - 0.306600i$	$0.267050 - 0.305436i$

Table 4. *Cont.*

		$\xi = 0.0$	$\xi = 0.1$	$\xi = 0.2$	$\xi = 0.3$
$l = 2$	$n = 0$	$0.314866 - 0.151628i$	$0.315354 - 0.151612i$	$0.316675 - 0.151405i$	$0.318846 - 0.150934i$
	$n = 1$	$0.361537 - 0.386194i$	$0.362144 - 0.386139i$	$0.363507 - 0.385916i$	$0.365546 - 0.385435i$
	$n = 2$	$0.374275 - 0.589655i$	$0.375054 - 0.589453i$	$0.376763 - 0.589111i$	$0.379266 - 0.588571i$
$l = 3$	$n = 0$	$0.339306 - 0.196909i$	$0.339784 - 0.196923i$	$0.341017 - 0.196749i$	$0.342997 - 0.196292i$
	$n = 1$	$0.435568 - 0.454491i$	$0.436184 - 0.454520i$	$0.437484 - 0.454464i$	$0.439359 - 0.454213i$
	$n = 2$	$0.485523 - 0.662549i$	$0.486310 - 0.662453i$	$0.487920 - 0.662319i$	$0.490190 - 0.662071i$
	$n = 3$	$0.504339 - 0.858598i$	$0.505262 - 0.858287i$	$0.507237 - 0.857947i$	$0.510080 - 0.857556i$

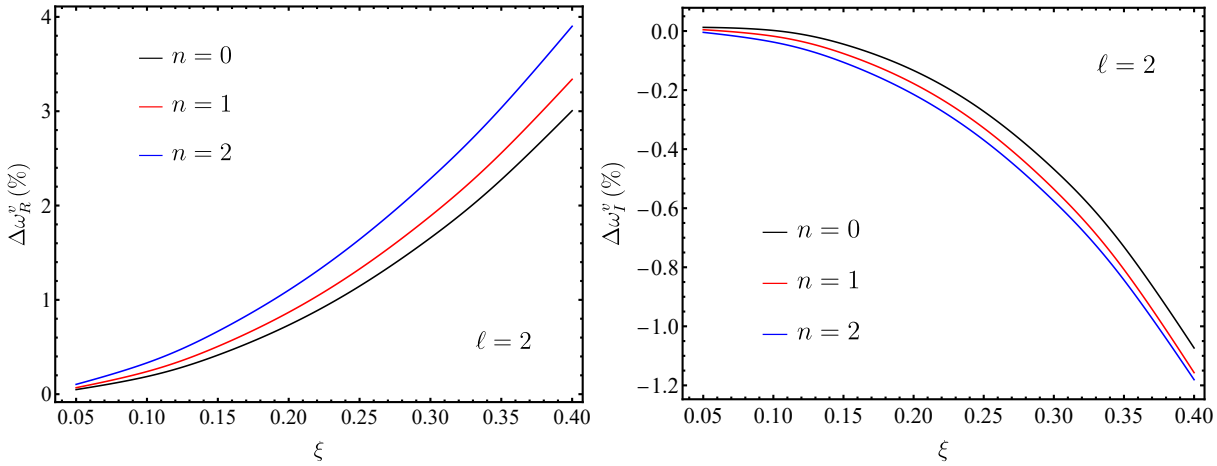

Figure 6. Dependence of the relative vector frequency shifts with respect to the Schwarzschild solution (real part on the left, imaginary part on the right) on the parameter ξ for $\ell = 2$. The distinct curves correspond to the radial overtone numbers $n = 0, 1, 2$.

4.3. Tensor Field Fluctuations

Unlike scalar and electromagnetic perturbations, tensor perturbations require consistent treatment of both the metric and the matter sector supporting the background geometry. Since no specific underlying theory is assumed here, we follow an effective description in which the spacetime is regarded as a solution of Einstein's equations sourced by an effective stress–energy tensor. This approach has been widely used in the study of modified and quantum-corrected black holes [165,171–173].

For a static and spherically symmetric background, the effective source can be modeled as an anisotropic fluid,

$$\mathcal{T}_{\mu\nu} = (\rho + p_2)u_\mu u_\nu + (p_1 - p_2)x_\mu x_\nu + p_2 g_{\mu\nu}, \tag{35}$$

where ρ, p_1, and p_2 denote the energy density, radial pressure, and tangential pressure, respectively. The timelike and radial unit vectors satisfy

$$u_\mu u^\mu = -1, \qquad x_\mu x^\mu = 1, \qquad u_\mu x^\mu = 0. \tag{36}$$

Following Ref. [174], we work in the comoving frame of the effective fluid, in which the background vectors take the form $u^\mu = (u^t, 0, 0, 0)$ and $x^\mu = (0, x^r, 0, 0)$. This choice is consistent with the static and spherically symmetric background geometry and specifies the anisotropic fluid ansatz employed in the perturbation analysis.

In the fluid rest frame, the nonvanishing mixed components of the background stress–energy tensor are

$$\mathcal{T}_t^t = -\rho, \qquad \mathcal{T}_r^r = p_1, \qquad \mathcal{T}_\theta^\theta = \mathcal{T}_\varphi^\varphi = p_2. \tag{37}$$

The background geometry fixes their radial dependence through the corresponding components of the Einstein tensor.

To study the axial, or odd-parity, gravitational perturbations, we adopt the standard axially symmetric line element [174],

$$\begin{aligned} \mathrm{d}s^2 = & -e^{2\nu}\left(\mathrm{d}x^0\right)^2 + e^{2\psi}\left(\mathrm{d}x^1 - \sigma\,\mathrm{d}x^0 - q_2\,\mathrm{d}x^2 - q_3\,\mathrm{d}x^3\right)^2 \\ & + e^{2\mu_2}\left(\mathrm{d}x^2\right)^2 + e^{2\mu_3}\left(\mathrm{d}x^3\right)^2, \end{aligned} \tag{38}$$

where $x^0 = t$, $x^1 = \varphi$, $x^2 = r$, and $x^3 = \theta$. The functions σ, q_2, and q_3 vanish in the static background and therefore enter only in linear order.

Following Ref. [174], the perturbation equations are projected onto an orthonormal tetrad adapted to Equation (38). In this frame, the perturbed anisotropic stress–energy tensor can be written as

$$\begin{aligned} \delta\mathcal{T}_{ab} = & (\rho + p_2)\delta(u_a u_b) + (\delta\rho + \delta p_2)u_a u_b \\ & + (p_1 - p_2)\delta(x_a x_b) + (\delta p_1 - \delta p_2)x_a x_b + \delta p_2 \eta_{ab}. \end{aligned} \tag{39}$$

Using the normalization and orthogonality conditions in Equation (36), its axial components vanish:

$$\delta\mathcal{T}_{10} = \delta\mathcal{T}_{12} = \delta\mathcal{T}_{13} = 0. \tag{40}$$

Thus, although the effective matter sector must be perturbed consistently, it does not directly source the odd-parity modes. This simplification is specific to the axial sector and does not generally apply to polar perturbations.

The axial field equations therefore reduce to

$$R_{ab}\big|_{\text{axial}} = 0. \tag{41}$$

Combining the relevant tetrad components as described in Ref. [174], one obtains a Schrödinger-like master equation for the tensor perturbations. The corresponding effective potential is [165,175]

$$\mathcal{V}^t(r,\ell,\xi) = A(r,\xi)\left[\frac{2}{r^2}(B(r,\xi)-1) + \frac{\ell(\ell+1)}{r^2} - \frac{1}{r\sqrt{A(r,\xi)B(r,\xi)^{-1}}}\frac{\mathrm{d}}{\mathrm{d}r}\sqrt{A(r,\xi)B(r,\xi)}\right]. \tag{42}$$

For the metric given in Equation (7), this potential takes the explicit form

$$\begin{aligned} \mathcal{V}^t(r,\ell,\xi) = & \left(1 - \frac{2M}{r} + \frac{\xi}{r^2}\right)\left[\frac{\ell(\ell+1)}{r^2} + \frac{4M\left(\xi^{3/2} - r^3\right)}{r^6}\right. \\ & \left. + \frac{6M\xi^{7/2} + 2Mr^4(2M-r) + \xi^2 r^3(r-3M) + 2M\xi^{3/2}r(2r-5M)}{r^6\sqrt{\frac{-2Mr+\xi^2+r^2}{2M\left(\xi^{3/2}-r^3\right)+r^4}}\sqrt{\left(-2Mr+\xi^2+r^2\right)\left[2M\left(\xi^{3/2}-r^3\right)+r^4\right]}}\right]. \end{aligned} \tag{43}$$

It is immediately apparent that, in the limit $\xi \to 0$, the effective potential reproduces the familiar result obtained for the Schwarzschild spacetime.

Figure 7 shows the behavior of the tensor potential $\mathcal{V}^t(r, \ell, \xi)$ as a function of the radial coordinate r for several values of ℓ and ξ. The curves demonstrate that larger ξ or ℓ shift the peak upward and broaden the barrier, indicating stronger confinement of the perturbations. Since the geometry is asymptotically flat, the potential smoothly falls to zero as $r \to \infty$, in accordance with the expected behavior at spatial infinity.

The associated quasinormal resonances are summarized in Table 5 for different combinations of ξ, and ℓ. A tensor QNM deviation is represented in Figure 8. As ξ increases, the real part, ω_R of the quasinormal frequency shifts toward larger values, whereas $|\omega_I|$ decreases. The tensor modes therefore oscillate more rapidly and decay more slowly than in the Schwarzschild limit.

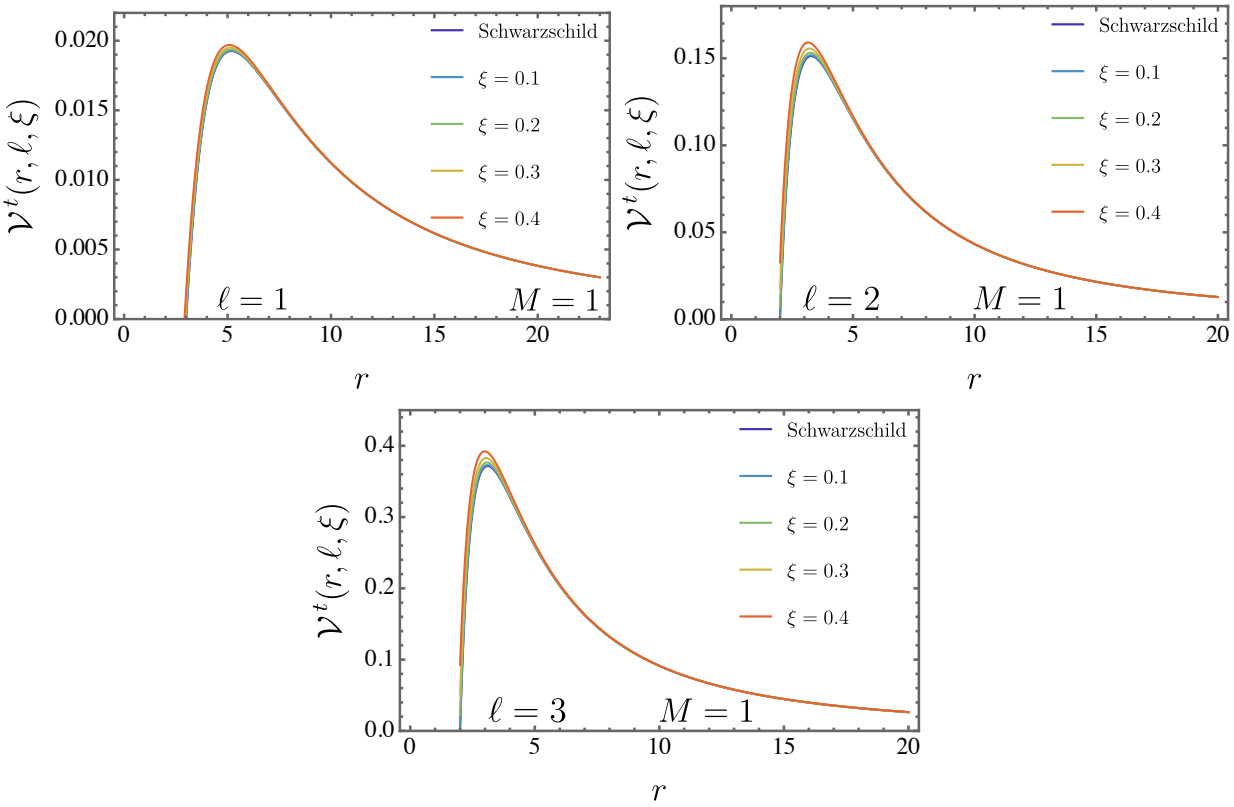

Figure 7. The tensor perturbation potential $\mathcal{V}^t(r, \ell, \xi)$ is plotted as a function of r, with several choices of ℓ and ξ, demonstrating pictorially how variations in these parameters modify the barrier's shape, peak position, and overall amplitude. The radial component is displayed over the interval $r \in [2, 20]$.

Table 5. The table presents the quasinormal mode spectra regarding tensor fluctuations for $\ell = 2, 3, 4$, highlighting how these modes change as the parameter ξ varies. The mass is fixed at $M = 1$.

		$\xi = 0.0$	$\xi = 0.1$	$\xi = 0.2$	$\xi = 0.3$
$\ell = 2$	$n = 0$	$0.373162 - 0.0892174i$	$0.373860 - 0.0891673i$	$0.375761 - 0.0889624i$	$0.378901 - 0.0885588i$
	$n = 1$	$0.346017 - 0.274915i$	$0.346934 - 0.274707i$	$0.349134 - 0.274010i$	$0.352569 - 0.272705i$
	$n = 2$	$0.302935 - 0.471064i$	$0.304206 - 0.470622i$	$0.306890 - 0.469370i$	$0.310794 - 0.467150i$
$\ell = 3$	$n = 0$	$0.599265 - 0.0927284i$	$0.600330 - 0.0927209i$	$0.603415 - 0.0925844i$	$0.608625 - 0.0922654i$
	$n = 1$	$0.582355 - 0.281406i$	$0.583581 - 0.281353i$	$0.586892 - 0.280898i$	$0.592338 - 0.279889i$
	$n = 2$	$0.553200 - 0.476684i$	$0.554706 - 0.476524i$	$0.558399 - 0.475677i$	$0.564224 - 0.473913i$
	$n = 3$	$0.515747 - 0.677429i$	$0.517618 - 0.677111i$	$0.521818 - 0.675833i$	$0.528157 - 0.673312i$

Table 5. *Cont.*

		$\xi = 0.0$	$\xi = 0.1$	$\xi = 0.2$	$\xi = 0.3$
$\ell = 4$	$n = 0$	$0.809098 - 0.0941711i$	$0.810500 - 0.0941707i$	$0.814652 - 0.0940442i$	$0.821714 - 0.0937360i$
	$n = 1$	$0.796499 - 0.284366i$	$0.798023 - 0.284347i$	$0.802341 - 0.283939i$	$0.809573 - 0.282981i$
	$n = 2$	$0.773636 - 0.478974i$	$0.775379 - 0.478891i$	$0.779989 - 0.478143i$	$0.787505 - 0.476478i$
	$n = 3$	$0.743312 - 0.678300i$	$0.745343 - 0.678106i$	$0.750335 - 0.676973i$	$0.758213 - 0.674573i$
	$n = 4$	$0.707214 - 0.881266i$	$0.709589 - 0.880926i$	$0.715046 - 0.879383i$	$0.723375 - 0.876257i$

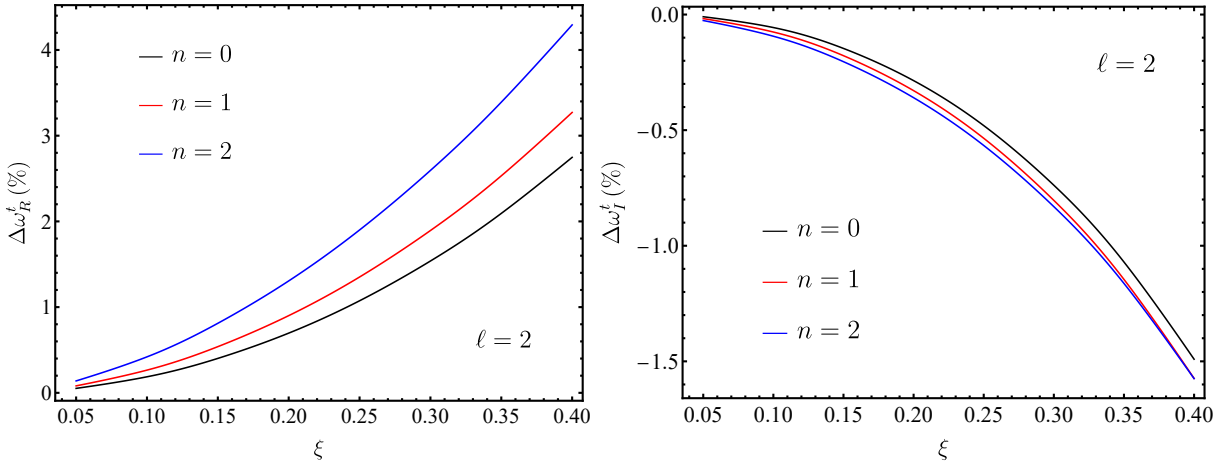

Figure 8. Relative shifts in the real (**left**) and imaginary (**right**) parts of the tensor quasinormal frequencies with respect to the Schwarzschild case ($\xi = 0$) as functions of ξ for $\ell = 2$. The curves correspond to $n = 0, 1$, and 2.

4.4. Spinor Field Fluctuations

This part of the study focuses on the evolution of massless Dirac fields propagating in a static, spherically symmetric black hole geometry. The dynamics of spin-$\frac{1}{2}$ perturbations are examined using the Newman–Penrose formalism, which provides a convenient framework for handling spinor equations in curved spacetime. Within this approach, the governing Dirac equations take the form [176,177]

$$(D + \epsilon - \rho)\psi_1 + (\bar{\delta} + \pi - \alpha)\psi_2 = 0, \tag{44}$$

$$(\Delta + \mu - \gamma)\psi_2 + (\delta + \beta - \mathrm{t})\psi_1 = 0. \tag{45}$$

Within this formalism, two spinor components, ψ_1 and ψ_2, are defined, and their evolution is described using directional derivatives taken along the null tetrad vectors: $D = l^\mu \partial_\mu$, $\Delta = n^\mu \partial_\mu$, $\delta = m^\mu \partial_\mu$, and $\bar{\delta} = \bar{m}^\mu \partial_\mu$.

The next step consists of building the null tetrad itself from the underlying metric, specifying the vectors l^μ, n^μ, m^μ, and $\bar{m}^\mu$ explicitly, which provides the basis required to express the Dirac equations in this spacetime.

$$\begin{aligned} l^\mu &= \left(\frac{1}{A(r,\xi)}, \sqrt{\frac{B(r,\xi)}{A(r,\xi)}}, 0, 0\right), \quad n^\mu = \frac{1}{2}\left(1, -\sqrt{A(r,\xi)B(r,\xi)}, 0, 0\right), \\ m^\mu &= \frac{1}{\sqrt{2}r}\left(0, 0, 1, \frac{i}{\sin\theta}\right), \quad \bar{m}^\mu = \frac{1}{\sqrt{2}r}\left(0, 0, 1, \frac{-i}{\sin\theta}\right). \end{aligned} \tag{46}$$

Using these definitions, one can compute the spin coefficients, obtaining the following nonvanishing terms:

$$\rho = -\frac{1}{r}\frac{B(r,\xi)}{A(r,\xi)}, \quad \mu = -\frac{\sqrt{A(r,\xi)B(r,\xi)}}{2r},$$
$$\gamma = \frac{A(r,\xi)'}{4}\sqrt{\frac{B(r,\xi)}{A(r,\xi)}}, \quad \beta = -\alpha = \frac{\cot\theta}{2\sqrt{2}r}. \tag{47}$$

Decoupling the coupled Dirac equations leads to a single differential equation that governs the evolution of ψ_1, fully characterizing the dynamics of the massless spin–$\frac{1}{2}$ field in this spacetime:

$$\left[(D-2\rho)(\Delta+\mu-\gamma)-(\delta+\beta)(\bar{\delta}+\beta)\right]\psi_1 = 0. \tag{48}$$

After inserting the explicit expressions for the directional derivatives and the computed spin coefficients into the Dirac equation, it can be reformulated and expressed in the form

$$\begin{aligned}
&\left[\frac{1}{2A(r,\xi)}\partial_t^2 - \left(\frac{\sqrt{A(r,\xi)B(r,\xi)}}{2r} + \frac{A(r,\xi)'}{4}\sqrt{\frac{B(r,\xi)}{A(r,\xi)}}\right)\frac{1}{A(r,\xi)}\partial_t\right.\\
&-\frac{\sqrt{A(r,\xi)B(r,\xi)}}{2}\sqrt{\frac{B(r,\xi)}{A(r,\xi)}}\partial_r^2\\
&\left.-\sqrt{\frac{B(r,\xi)}{A(r,\xi)}}\partial_r\left(\frac{\sqrt{A(r,\xi)B(r,\xi)}}{2} + \frac{A(r,\xi)'}{4}\sqrt{\frac{B(r,\xi)}{A(r,\xi)}}\right)\right]\psi_1\\
&+\left[\frac{1}{\sin^2\theta}\partial_\phi^2 + i\frac{\cot\theta}{\sin\theta}\partial_\phi\right.\\
&\left.+\frac{1}{\sin\theta}\partial_\theta(\sin\theta\partial_\theta) - \frac{1}{4}\cot^2\theta + \frac{1}{2}\right]\psi_1 = 0.
\end{aligned} \tag{49}$$

In order to separate the Dirac equation into its radial and angular components, the spinor field is expressed as $\psi_1 = \Psi(r)Y_{lm}(\theta,\phi)e^{-i\omega t}$, so that

$$\left[\frac{-\omega^2}{2A(r,\xi)} - \left(\frac{\sqrt{A(r,\xi)B(r,\xi)}}{2r} + \frac{A(r,\xi)'}{4} + \sqrt{\frac{B(r,\xi)}{A(r,\xi)}}\right)\frac{-i\omega}{A(r,\xi)}\right. \tag{50}$$
$$\left.-\frac{\sqrt{A(r,\xi)B(r,\xi)}}{2}\sqrt{\frac{B(r,\xi)}{A(r,\xi)}}\partial_r^2 - \lambda_{lm}\right. \tag{51}$$
$$\left.-\sqrt{\frac{B(r,\xi)}{A(r,\xi)}}\partial_r\left(\frac{\sqrt{A(r,\xi)B(r,\xi)}}{2r} + \frac{A(r,\xi)'}{4}\sqrt{\frac{B(r,\xi)}{A(r,\xi)}}\right)\right]\Psi(r) = 0. \tag{52}$$

Here, λ_{lm} acts as the separation constant connecting the angular and radial parts of the solution. By introducing r^*, we verify that the radial equation can be recast into a Schrödinger-type wave equation, taking the form

$$\left[\frac{\mathrm{d}^2}{\mathrm{d}r_*^2} + (\omega^2 - \mathcal{V}^{spin\pm}(r,\ell,\xi))\right]\Psi_\pm(r) = 0. \tag{53}$$

In addition, the effective potentials $\mathcal{V}^{\text{spin}\pm}(r,\ell,\xi)$ governing the propagation of the massless spin-$\frac{1}{2}$ field can be introduced, taking the form given in [178–180]:

$$\mathcal{V}^{spin\pm}(r,\ell,\xi) = \frac{(\ell+\frac{1}{2})^2}{r^2}A(r,\xi) \pm \left(\ell+\frac{1}{2}\right)\sqrt{A(r,\xi)B(r,\xi)}\partial_r\left(\frac{\sqrt{A(r,\xi)}}{r}\right). \tag{54}$$

In what follows, the potential $\mathcal{V}^{\text{spin+}}(r,\ell,\xi)$ is selected as the representative case, since the corresponding $\mathcal{V}^{\text{spin-}}(r,\ell,\xi)$ exhibits a qualitatively similar profile [175,178,181]. Hence,

the analysis concentrates on $\mathcal{V}^{\text{spin+}}(r, \ell, \xi)$. Its behavior is depicted in Figure 9, where the potential is shown as a function of r for different parameter choices. Consistent with the asymptotically flat nature of the spacetime, $\mathcal{V}^{\text{spin+}}(r, \ell, \xi)$ tends to zero as $r \to \infty$.

Figure 9 highlights the spinor potential $\mathcal{V}^{\text{spin+}}(r, \ell, \xi)$ plotted versus r for a range of ℓ and ξ values. The plots reveal that increasing either parameter raises the maximum of the potential and widens the barrier region, which enhances the trapping of perturbations near the black hole. Because the spacetime approaches flatness at large distances, the potential decays to zero as $r \to \infty$, which is naturally consistent with the expected asymptotic behavior.

The quasinormal frequencies obtained from this potential are listed in Table 6, covering several choices of ξ and ℓ. The relative deviations shown in Figure 10 indicate that the spinor spectrum is also sensitive to ξ. Larger values of the parameter ξ increase the oscillation frequency while weakening the damping, thereby extending the characteristic lifetime of the spinor modes.

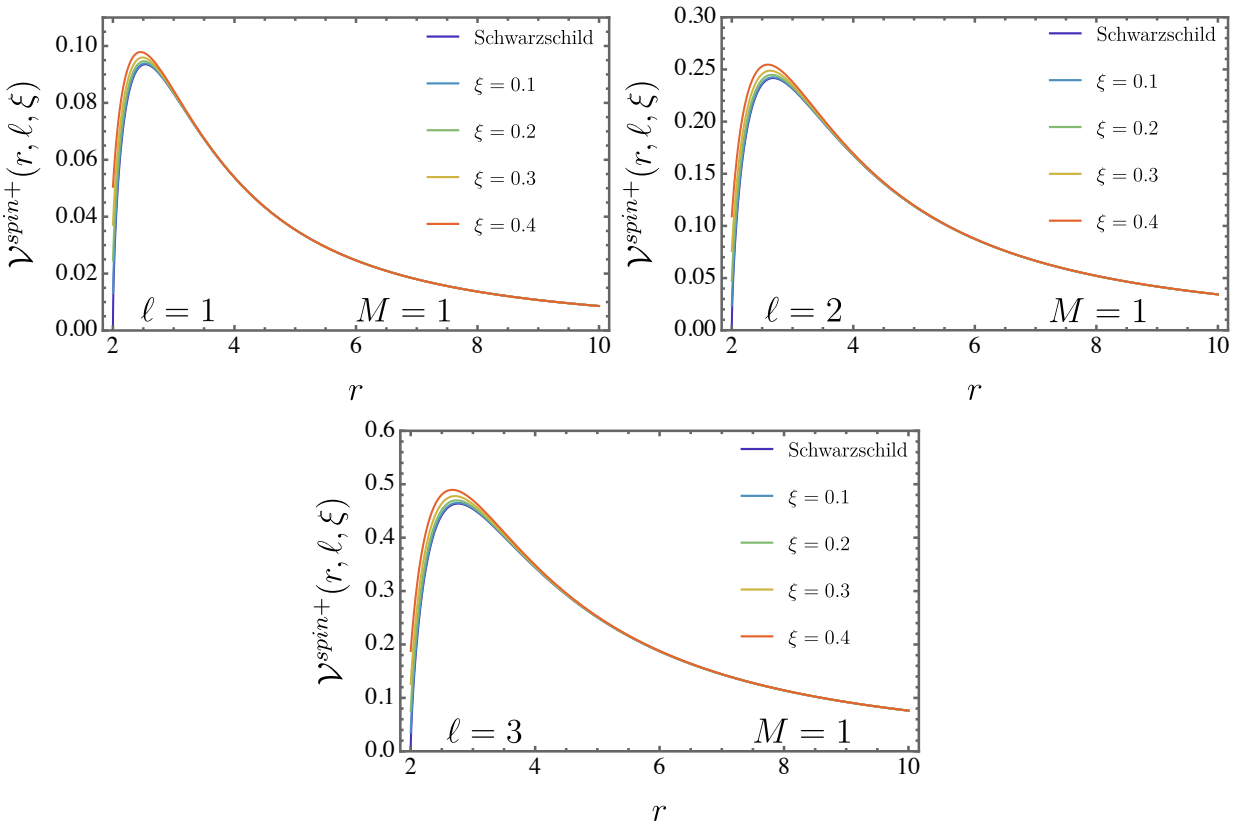

Figure 9. The spinor perturbation potential $\mathcal{V}^{\text{spin+}}(r, \ell, \xi)$ is shown as a function r for distinct values ξ and ℓ, clearly illustrating how changes in these parameters affect the potential barrier.

Table 6. This table reports the quasinormal spectra for spinor fluctuations in the case $\ell = 1, 2, 3$, presenting how the frequencies evolve as *xi* grows. The mass is fixed at $M = 1$.

		$\xi = 0.0$	$\xi = 0.1$	$\xi = 0.2$	$\xi = 0.3$
$\ell = 1$	$n = 0$	$0.279242 - 0.0971428i$	$0.279821 - 0.0971098i$	$0.281415 - 0.0969493i$	$0.284049 - 0.0966185i$
	$n = 1$	$0.249534 - 0.306401i$	$0.250419 - 0.306287i$	$0.252412 - 0.305497i$	$0.255415 - 0.303858i$
$\ell = 2$	$n = 0$	$0.476498 - 0.0963845i$	$0.477348 - 0.0963685i$	$0.479827 - 0.0962330i$	$0.484020 - 0.0959299i$
	$n = 1$	$0.455761 - 0.294988i$	$0.456782 - 0.294909i$	$0.459526 - 0.294400i$	$0.464017 - 0.293315i$
	$n = 2$	$0.423533 - 0.502794i$	$0.424851 - 0.502604i$	$0.427958 - 0.501613i$	$0.432752 - 0.499584i$

Table 6. *Cont.*

		$\xi = 0.0$	$\xi = 0.1$	$\xi = 0.2$	$\xi = 0.3$
$\ell = 3$	$n = 0$	$0.670533 - 0.0962939i$	$0.671692 - 0.0962879i$	$0.675135 - 0.0961606i$	$0.681001 - 0.0958597i$
	$n = 1$	$0.655450 - 0.291800i$	$0.656739 - 0.291759i$	$0.660373 - 0.291328i$	$0.666445 - 0.290352i$
	$n = 2$	$0.629465 - 0.493464i$	$0.630981 - 0.493342i$	$0.634919 - 0.492523i$	$0.641276 - 0.490761i$
	$n = 3$	$0.596416 - 0.700441i$	$0.598232 - 0.700199i$	$0.602540 - 0.698948i$	$0.609208 - 0.696369i$

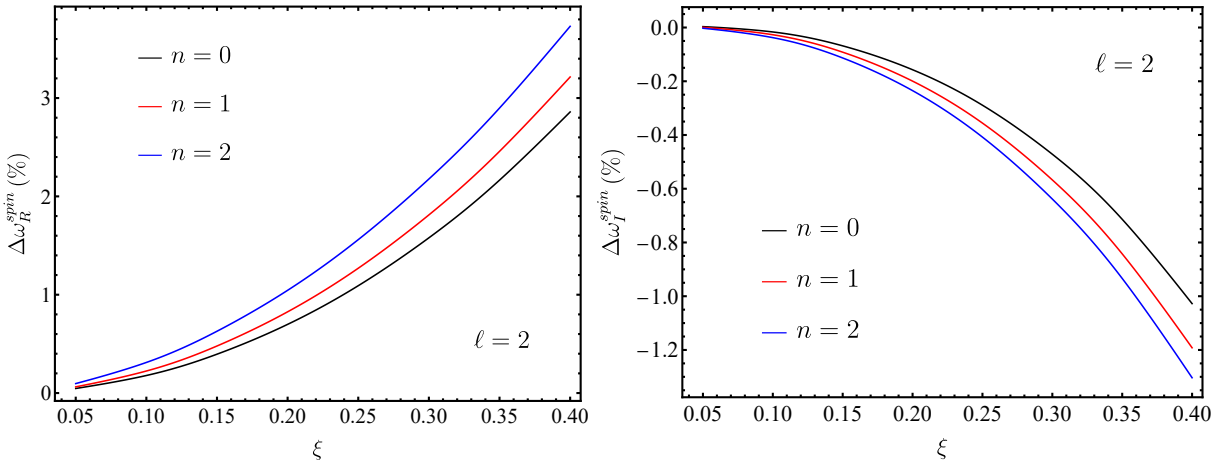

Figure 10. Relative shifts in the spinor quasinormal modes as functions of parameter ξ for $\ell = 2$. The left and right panels show the real and imaginary parts, respectively. Results are shown for the fundamental mode $n = 0$ and the first two overtones $n = 1, 2$.

5. Time-Domain Solution

To obtain the time evolution of scalar, vector, and tensor fluctuations, it is essential to perform a full dynamical analysis rather than relying solely on frequency-domain methods. This approach makes it possible to study how quasinormal modes influence scattering and decay processes. Because the effective potentials governing these perturbations are generally complicated, an accurate numerical scheme is required to evolve the system. Thereby, the characteristic integration method, first proposed by Gundlach et al. [182], is employed.

Following the procedure outlined in [182–188], the problem is reformulated in double-null coordinates defined by $u = t - r^*$ and $v = t + r^*$. This change in variables simplifies the wave equation and casts it into a form suitable for numerical integration. In terms of these coordinates, the equation is given by:

$$\left(4\frac{\partial^2}{\partial u\,\partial v} + V(u,v)\right)\tilde{\psi}(u,v) = 0. \tag{55}$$

A common method to solve the resulting equation numerically is to discretize the domain through a finite-difference approach, allowing the wave function to be evolved step by step across the grid:

$$\tilde{\psi}(N) = -\tilde{\psi}(S) + \tilde{\psi}(W) + \tilde{\psi}(E) - \frac{h^2}{8}V(S)\Big[\tilde{\psi}(W) + \tilde{\psi}(E)\Big] + \mathcal{O}(h^4). \tag{56}$$

Such a procedure begins by defining a grid on the (u, v) plane, where h represents the step size. Each cell is identified by four points: the starting position $S = (u, v)$, its neighbors $W = (u + h, v)$ and $E = (u, v + h)$, and the forward point $N = (u + h, v + h)$. The evolution is initialized along the characteristic lines $u = u_0$ and $v = v_0$, which act as

the initial boundaries for the integration scheme. To specify the initial data, a Gaussian pulse centered at $v = v_c$ with width σ is prescribed along $u = u_0$, providing the initial wave profile used to propagate the solution across the grid

$$\tilde{\psi}(\tilde{u} = u_0, v) = Ae^{-(v-v_0)^2}/2\sigma^2, \quad \tilde{\psi}(u, v_0) = \tilde{\psi}_0. \tag{57}$$

The numerical evolution starts by specifying the initial data along $v = v_0$ through the condition $\tilde{\psi}(u, v_0) = \tilde{\psi}_0$, which is set to zero to simplify the setup. The algorithm then advances the solution step by step along constant-u slices, updating the values as v increases according to the null-grid arrangement. For clarity and efficiency, the analysis is restricted to massless across all perturbations encountered in this paper with $M = 1$. The initial configuration is taken as a Gaussian wave packet centered at $v = 0$, with width $\sigma = 1$ and a vanishing starting amplitude. The integration domain is discretized uniformly over $u, v \in [0, 1000]$ with a grid spacing of $h = 0.1$, providing the resolution needed to track the propagation and decay of the signal.

5.1. Scalar Field

The temporal evolution of scalar fluctuations for the black hole background considered here is investigated in this part of the study. In Figure 11, the field $\tilde{\psi}$ is evolved for a fixed mass $M = 1$ while the parameter ξ is varied across 0.3, 0.5, 0.7, and 0.9. The results are displayed according to the angular mode: $\ell = 0$ (top left), $\ell = 1$ (top right), and $\ell = 2$ (bottom). Each curve exhibits exponentially damped oscillations, clearly signaling the presence of the quasinormal ringing phase characteristic of perturbed black hole spacetime considered in this paper (7) for the scalar perturbations.

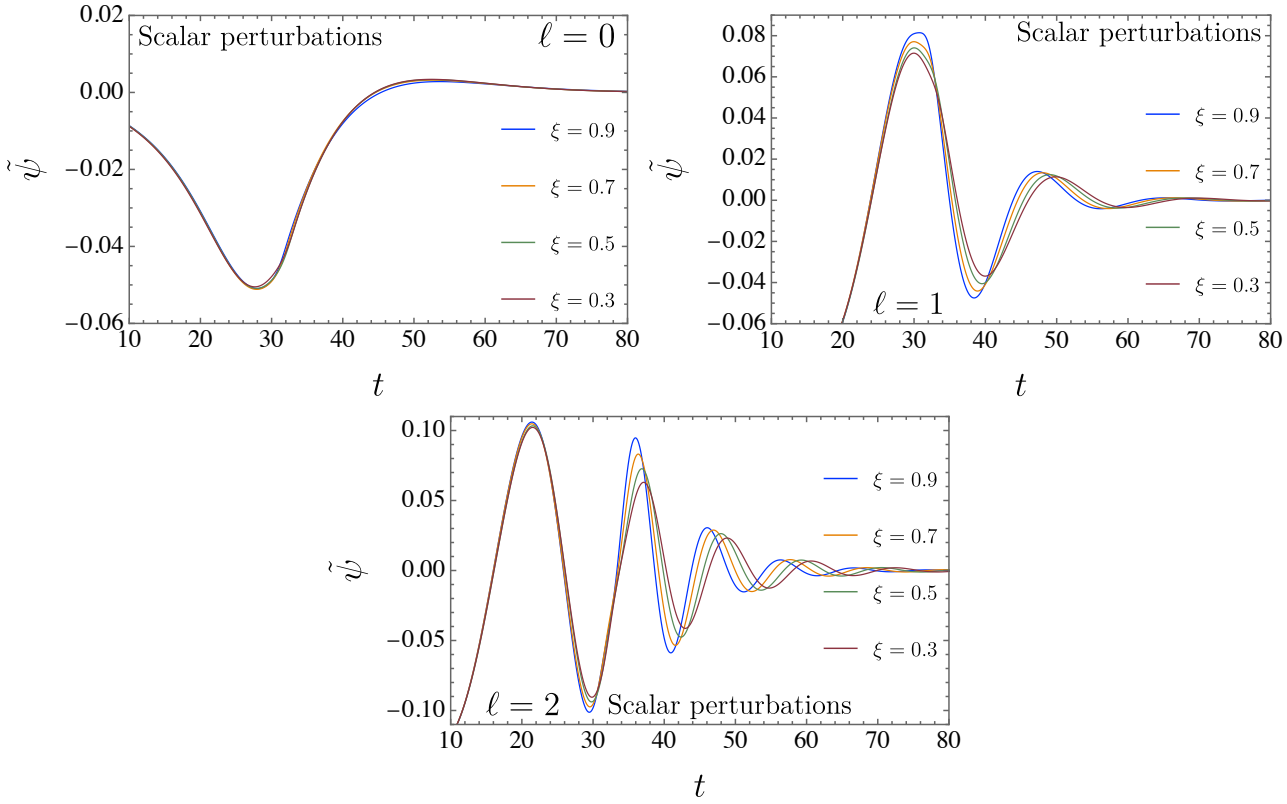

Figure 11. The dynamics of scalar perturbations are shown by evolving the waveform $\tilde{\psi}$ in time for a fixed black hole mass $M = 1$ and several values of the parameter ξ. The analysis considers $\xi = 0.3, 0.5, 0.7$, and 0.9, and the resulting waveforms are displayed according to the angular mode: the top-left panel corresponds to $\ell = 0$, the top-right to $\ell = 1$, and the bottom panel to $\ell = 2$.

In addition, a closer look at the damping behavior is provided in Figure 12, where the quantity $\ln|\tilde{\psi}|$ is plotted for the same set of ξ and ℓ values. These curves make the quasinormal phase more evident by displaying the exponential decay on a straight line, and they also highlight the point at which the system exits the oscillatory stage and enters the characteristic power-law tail regime at late times.

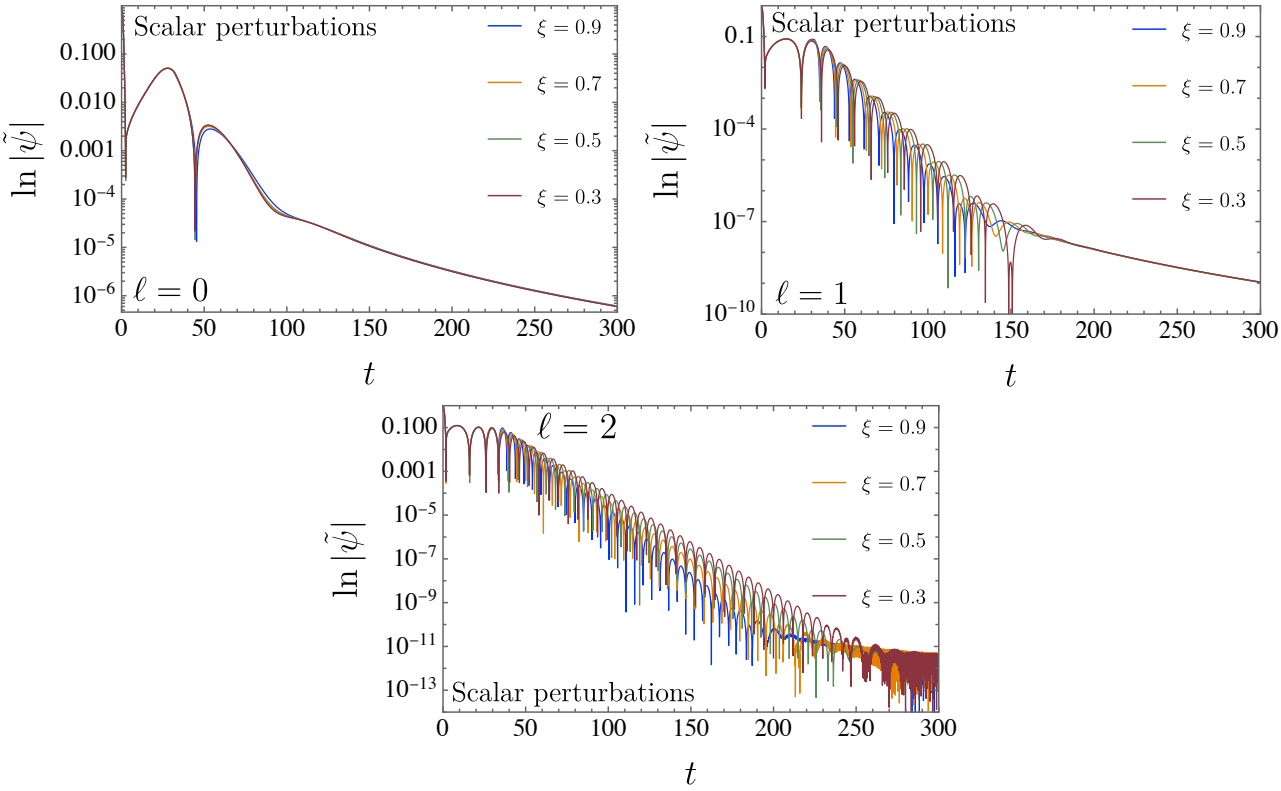

Figure 12. The logarithmic evolution of the scalar field amplitude, $\ln|\tilde{\psi}|$, is presented as a function of time t for a black hole with $M = 1$ and charge parameter values of $\xi = 0.3, 0.5, 0.7$, and 0.9. The plots are displayed by angular index, with $\ell = 0$ shown in the upper-left panel, $\ell = 1$ in the upper-right panel, and $\ell = 2$ in the bottom panel.

Lastly, Figure 13 presents the evolution of $\tilde{\psi}$ as a function of time on a logarithmic–logarithmic scale, using the same panel layout as before. This representation highlights the asymptotic regime, making the power-law decay at late times explicit and confirming the appearance of the characteristic tails that succeed the quasinormal ringing stage, as one should naturally expect.

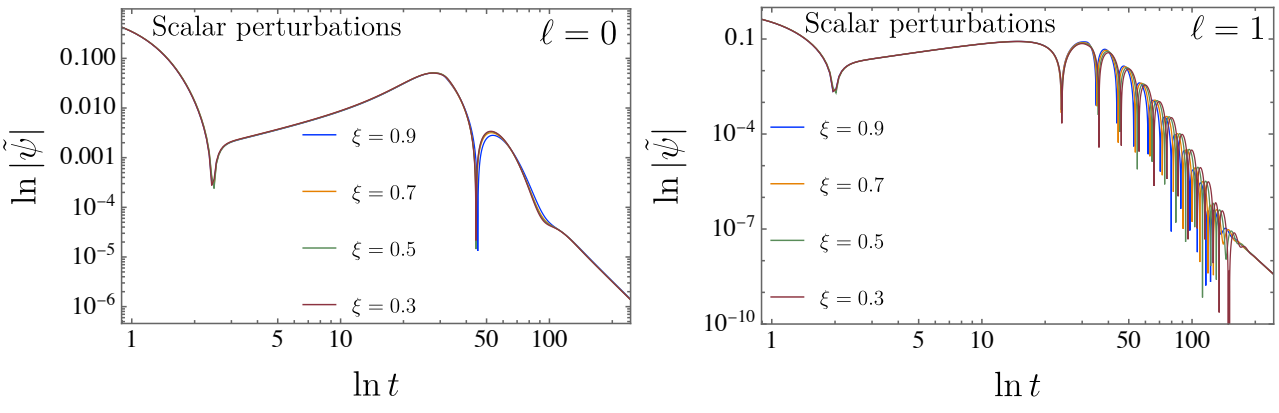

Figure 13. *Cont.*

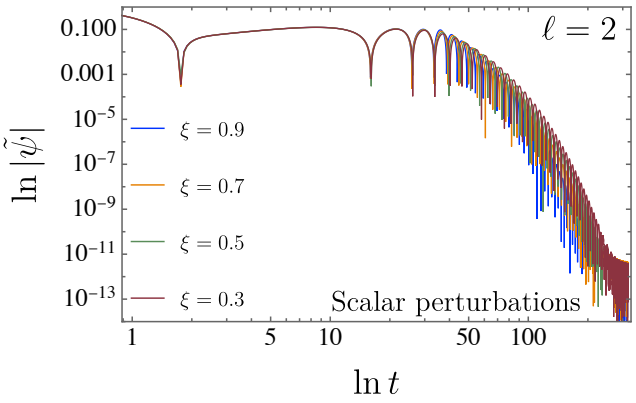

Figure 13. This figure shows the late-time behavior of the scalar field on a double-logarithmic scale, plotting $\ln|\tilde{\psi}|$ versus $\ln t$ for a fixed mass parameter $M = 1$ and charge values of $\xi = 0.3, 0.5, 0.7$, and 0.9. The panels are displayed by multipole number, with $\ell = 0$ in the top-left plot, $\ell = 1$ in the top-right, and $\ell = 2$ displayed in the bottom panel, which highlights the power-law decay characteristic of the tail regime.

5.2. Vector Field

The evolution of vector-type perturbations is analyzed by propagating the waveform $\tilde{\psi}$ over time for a fixed black hole mass $M = 1$ and several choices of the parameter ξ. The outcomes, shown in Figure 14 for $\xi = 0.3, 0.5, 0.7$, and 0.9, are shown by angular index: the left panel displays $\ell = 1$, while the right panel corresponds to $\ell = 2$ and the bottom one correspond to $\ell = 3$. Across all cases, the profiles reveal oscillatory behavior with amplitudes that steadily decay, characteristic of the quasinormal ringing phase.

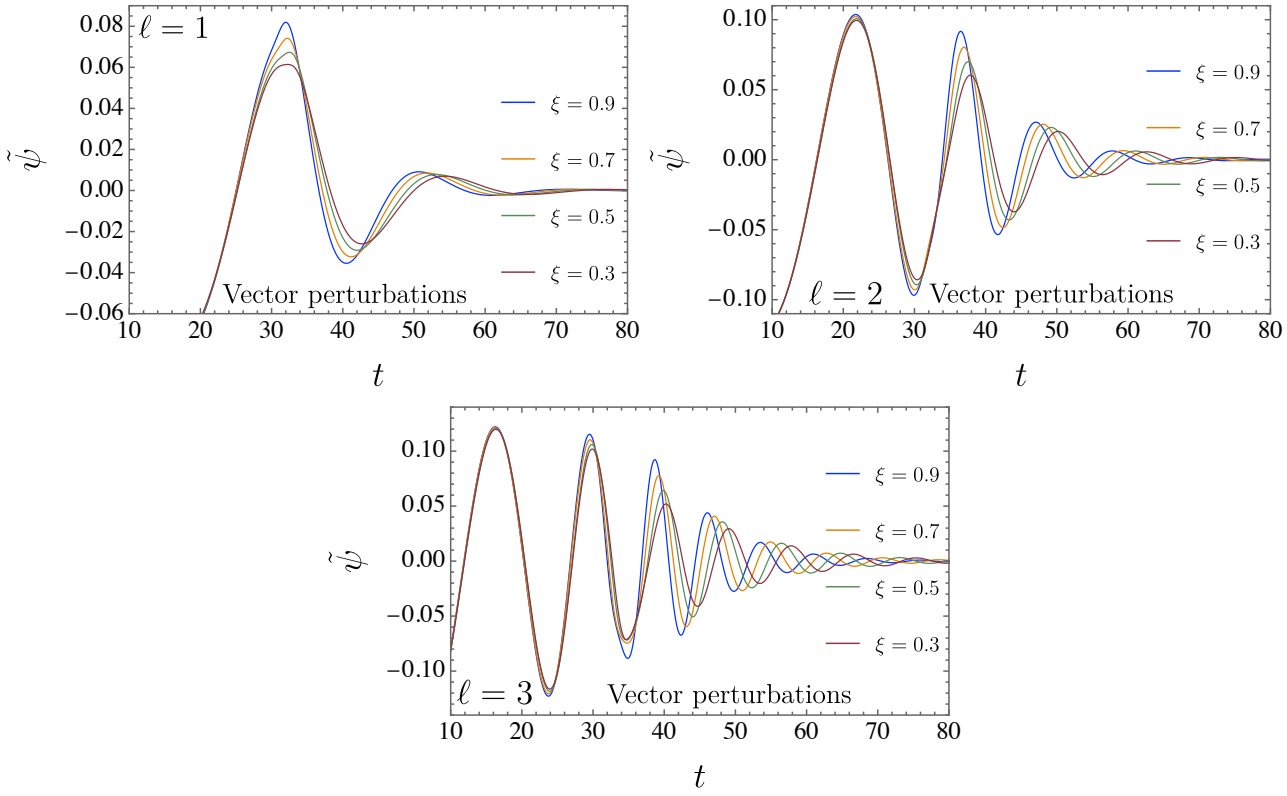

Figure 14. The temporal evolution of the vector perturbation $\tilde{\psi}$ concerning the time t is shown for a black hole with $M = 1$ and charge parameters of $\xi = 0.3, 0.5, 0.7$, and 0.9. The panels correspond to $\ell = 1$ (**left**), $\ell = 2$ (**right**), and $\ell = 3$ (**bottom**), illustrating the waveform's decay pattern for each multipole configuration.

Figure 15 displays the quantity $\ln|\tilde{\psi}|$ versus time, providing a clearer view of how the signal decays. The curves show that the evolution begins with a regime of exponential damping, after which the decay rate slows and follows a power-law profile. This crossover indicates the development of the late-time tail, a well-known effect caused by the scattering of perturbations by the spacetime considered here.

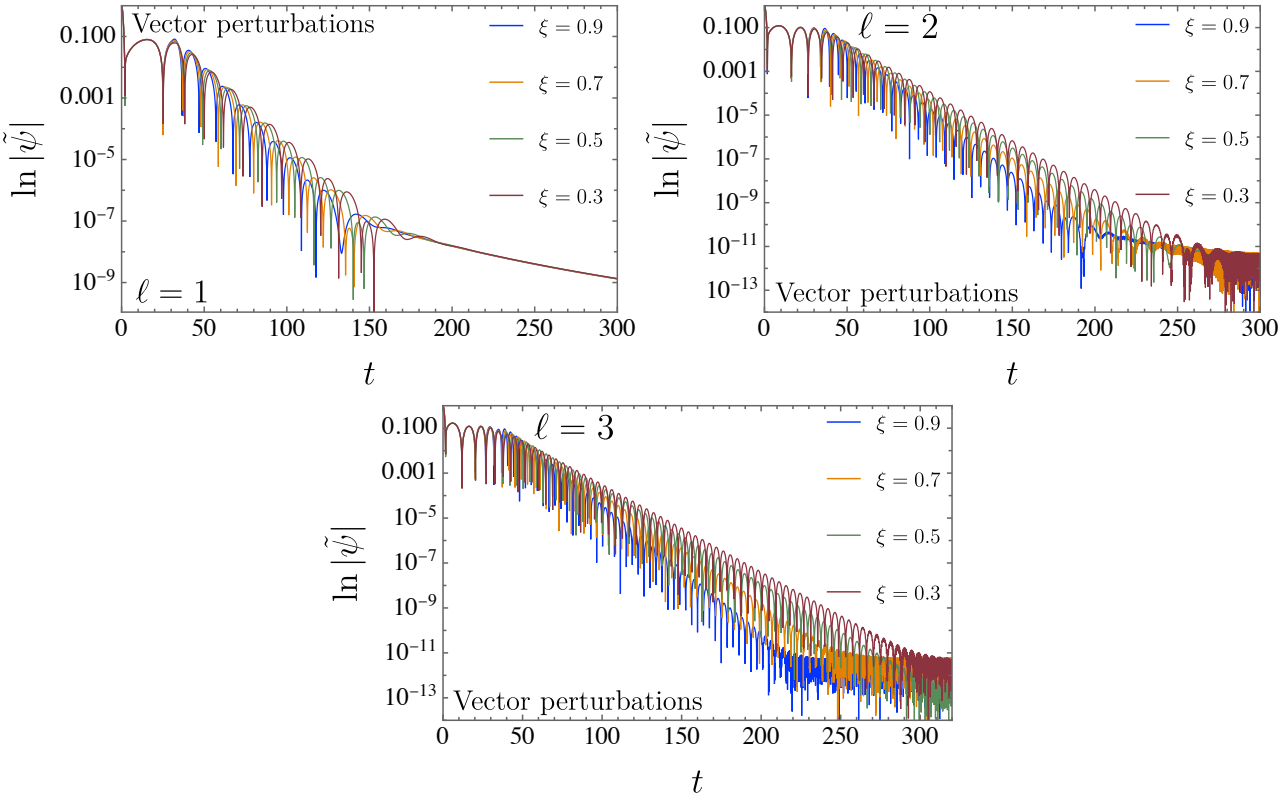

Figure 15. The time evolution of $\ln|\tilde{\psi}|$ with respect to the time t for vector perturbations against a background with $M = 1$. The analysis is performed for four distinct values of the parameter ξ (0.3, 0.5, 0.7, and 0.9). The results are shown by angular momentum number, with $\ell = 1$ shown in the left panel, $\ell = 2$ in the right panel, and $\ell = 3$ in the bottom panel.

In addition, Figure 16 presents the waveform evolution on a double-logarithmic scale, where $\ln|\tilde{\psi}|$ is plotted against $\ln t$. This representation highlights the late-time dynamics, clearly showing that the signal settles into a power-law decay. The slope of this tail remains nearly unchanged for different values of ξ and ℓ, indicating that the asymptotic behavior is largely universal.

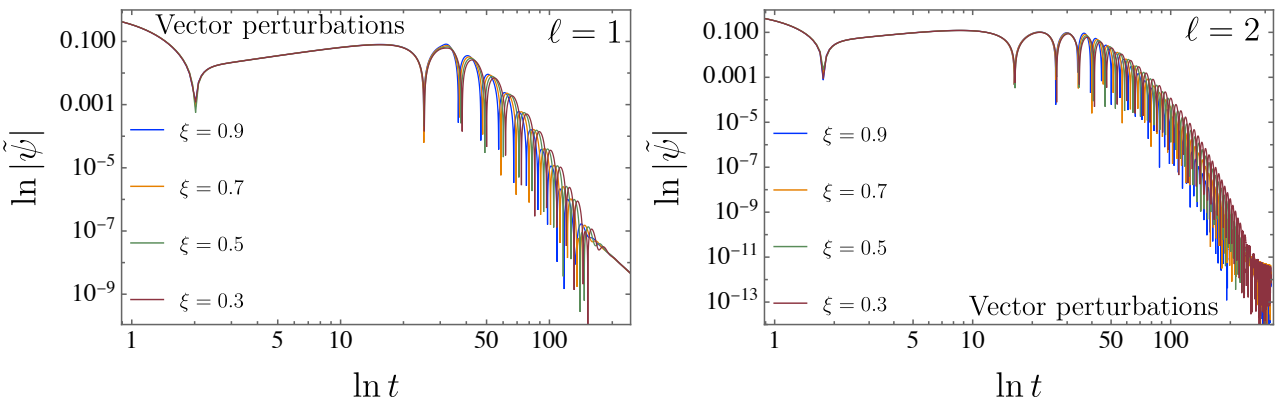

Figure 16. *Cont.*

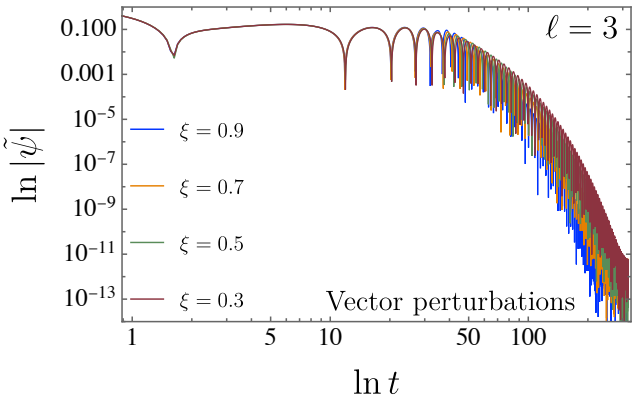

Figure 16. The double-logarithmic representation of $\tilde{\psi}$, plotting $\ln|\tilde{\psi}|$ against $\ln t$ for vector perturbations with $M = 1$. The analysis includes four values of the parameter ξ (0.3, 0.5, 0.7, and 0.9). The panels correspond to the three angular modes, $\ell = 1$ (**left**), $\ell = 2$ (**right**), and $\ell = 3$ (**bottom**), emphasizing the late-time power-law decay that characterizes the tail behavior.

5.3. Tensor Field

This subsection examines the time evolution of tensor fluctuations for our black hole. Figure 17 presents the waveform $\tilde{\psi}$ as a function of time for a fixed mass $M = 1$ and charge parameters $\xi = 0.3, 0.5, 0.7$, and 0.9. The results are displayed by angular mode, with $\ell = 1$ shown in the left panel, $\ell = 2$ in the right panel, and $\ell = 3$ in the bottom panel. To better visualize the damping behavior, Figure 18 plots $\ln|\tilde{\psi}|$ as a function of t, clearly revealing the exponential decay followed by a slower attenuation phase. Furthermore, Figure 19 uses a double-logarithmic scale, $\ln|\tilde{\psi}|$ versus $\ln t$, to highlight the late-time regime and therefore confirm the characteristic power-law tail behavior for each choice of ξ and ℓ.

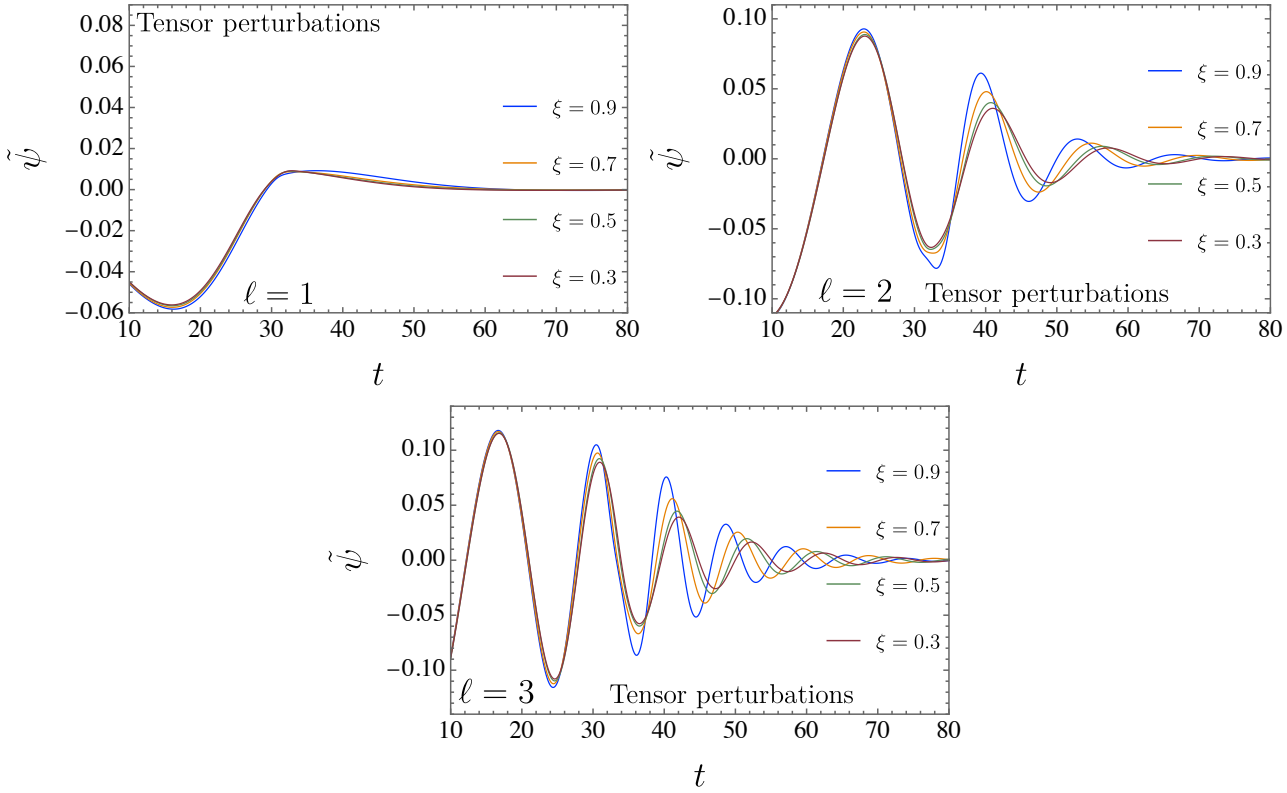

Figure 17. This figure shows the temporal evolution of the tensor perturbation $\tilde{\psi}$ with respect to the time t for a black hole with $M = 1$ and charge parameters of $\xi = 0.3, 0.5, 0.7$, and 0.9. The results are grouped by angular index, with $\ell = 1$ displayed in the left panel, $\ell = 2$ in the right panel, and $\ell = 3$ in the bottom panel, illustrating how the waveform evolves for each mode.

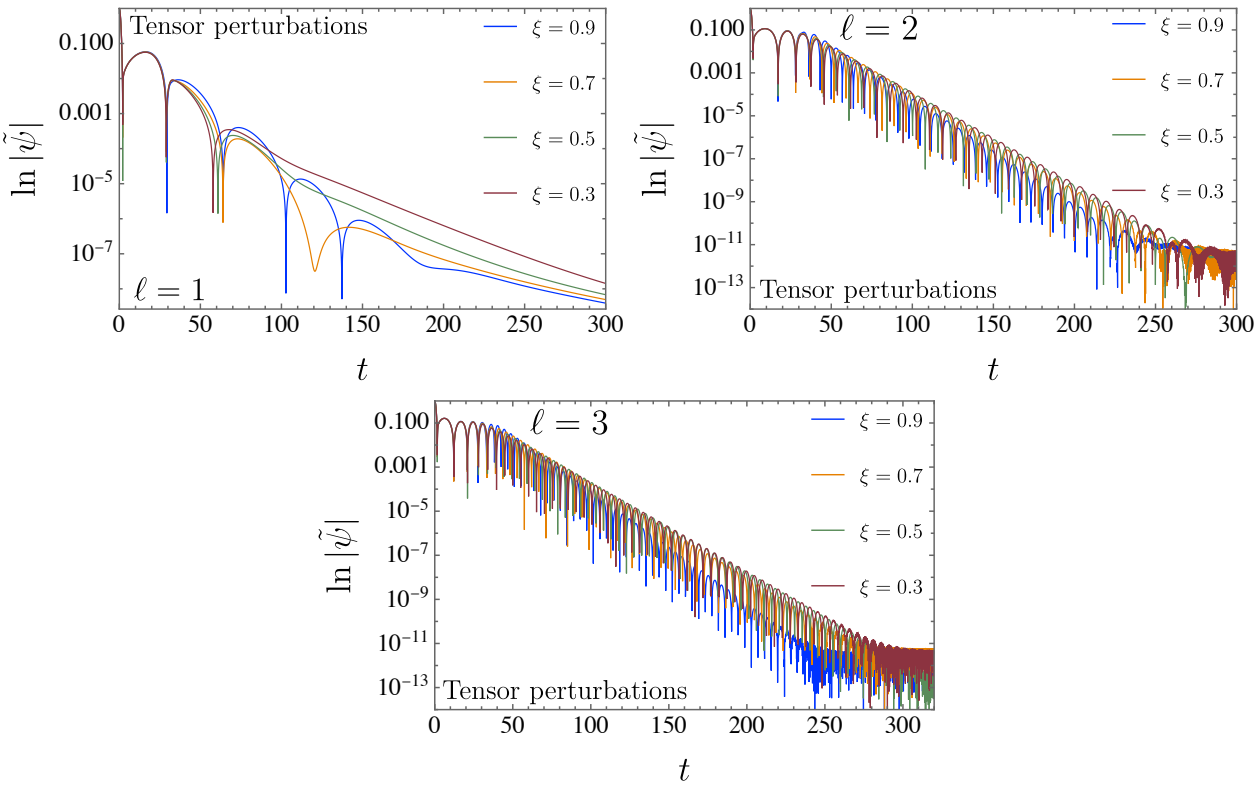

Figure 18. This figure displays the logarithmic time profile of the tensor perturbation, showing $\ln|\tilde{\psi}|$ as a function of t for $M = 1$ and $\xi = 0.3, 0.5, 0.7$, and 0.9. The plots are displayed by multipole number: $\ell = 1$ (**left**), $\ell = 2$ (**right**), and $\ell = 3$ (**bottom**).

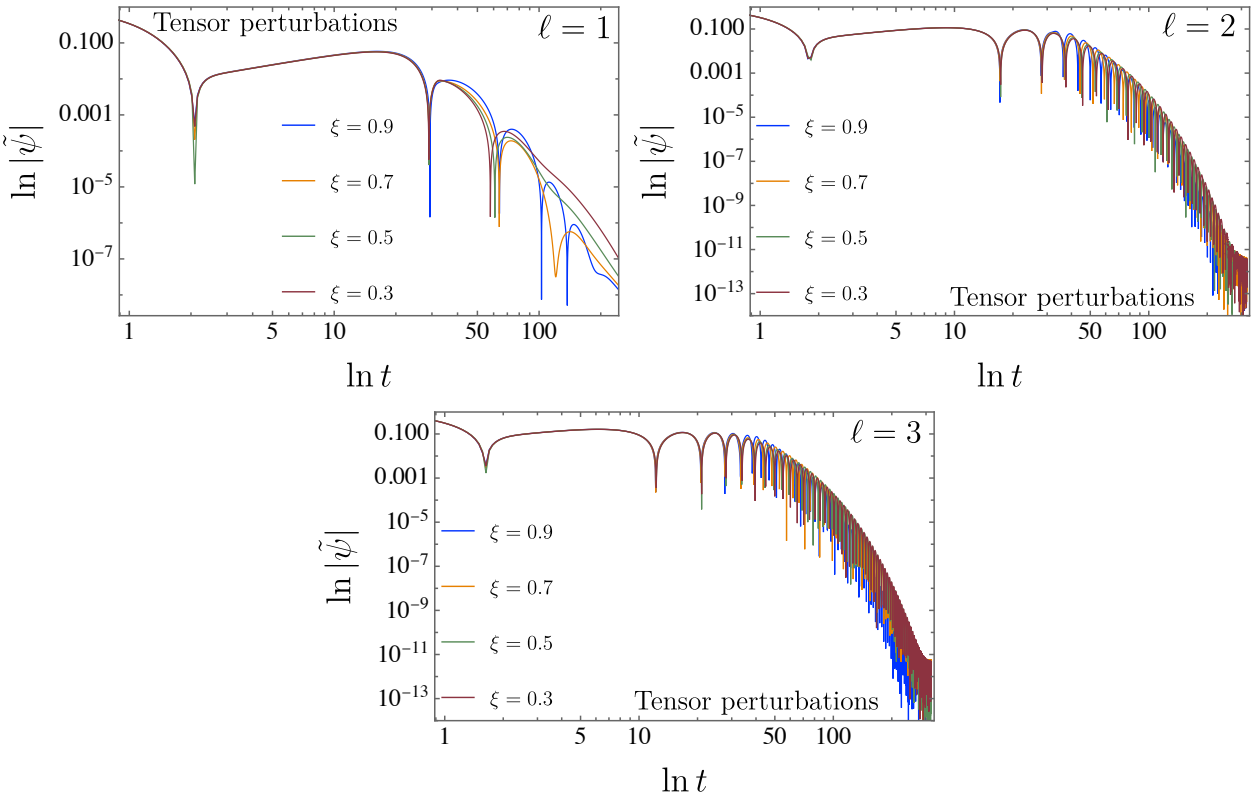

Figure 19. The asymptotic (late-time) regime of tensor perturbations using a double-logarithmic representation, where $\ln|\tilde{\psi}|$ is plotted as a function of $\ln t$ for a black hole with $M = 1$. The analysis considers $\xi = 0.3, 0.5, 0.7$, and 0.9, with the results separated by a multipole number: $\ell = 1$ in the left panel, $\ell = 2$ in the right panel, and $\ell = 3$ in the bottom panel.

5.4. Spinor Field

To complete the analysis, the final class of perturbations—those associated with spinor fields—is investigated in this subsection. Figure 20 displays the time evolution of the spinor waveform $\tilde{\psi}$ for $M = 1$ and charge parameters of $\xi = 0.3, 0.5, 0.7$, and 0.9. The panels correspond to the angular modes $\ell = 1$ (left), $\ell = 2$ (right), and $\ell = 3$ (bottom), showing how the signal evolves in each case.

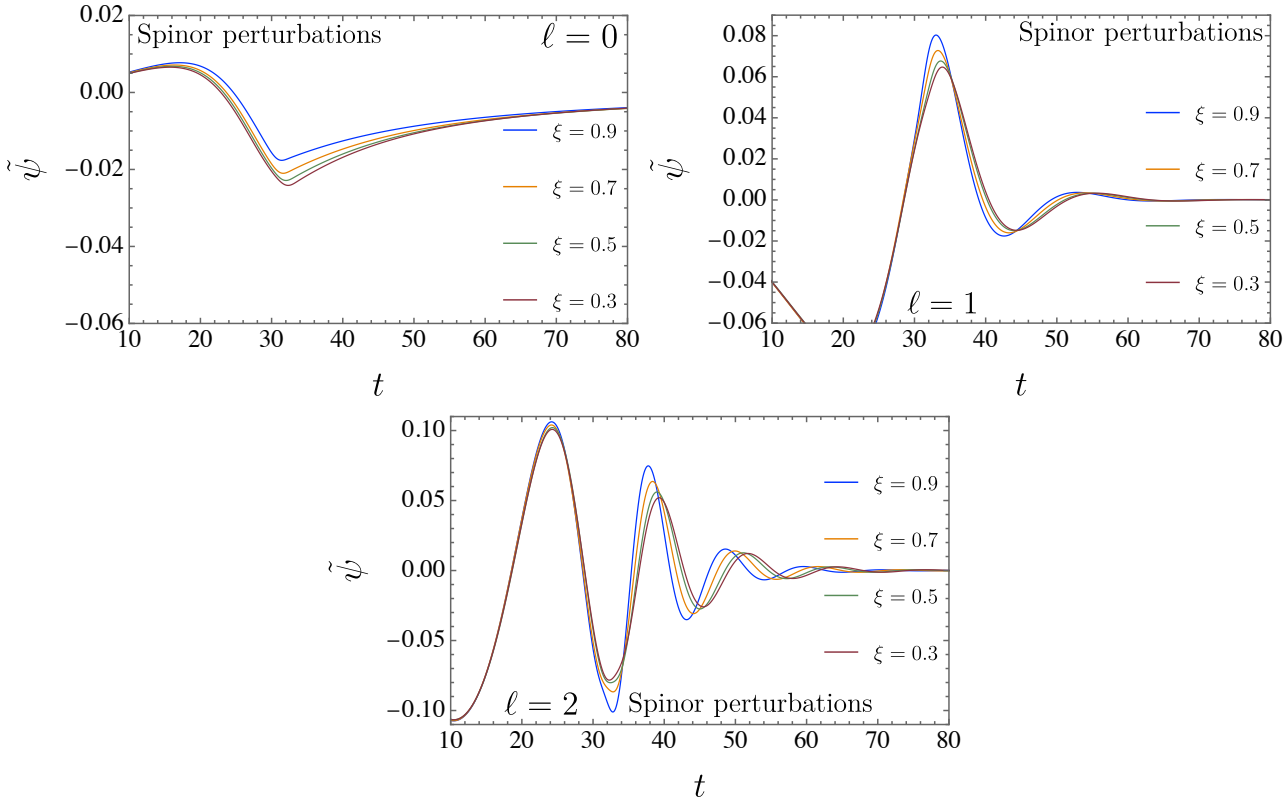

Figure 20. Temporal evolution of the tensor perturbation $\tilde{\psi}$ concerning the time t for $M = 1$ and $\xi = 0.3, 0.5, 0.7$, and 0.9. The panels show the results for $\ell = 0$ (**left**), $\ell = 1$ (**right**), and $\ell = 2$ (**bottom**), showing the distinct waveform profiles for each multipole configuration.

For a clearer view of the damping behavior, as we have done in the previous subsections, Figure 21 presents $\ln|\tilde{\psi}|$ as a function of time, making the quasinormal ringing and subsequent decay phase evident. Also, Figure 22 adopts a double-logarithmic representation, plotting $\ln|\tilde{\psi}|$ against $\ln t$, which therefore highlights the asymptotic regime and demonstrates the emergence of the expected power-law tails for all values of ξ and ℓ.

Here, a remark is in order in light of the cases discussed above: at late times, the decay of all perturbations is characterized by power-law tails, which arise from the backscattering of the fields off the asymptotic spacetime curvature. This behavior is governed by the far-region structure of the corresponding effective potentials. In our present model, the effective potentials associated with scalar, vector, tensor, and spinor perturbations can be expressed in the generic form

$$\mathcal{V}(r, \ell, \xi) = A(r, \xi)\left[\frac{\nu}{r^2} + \Delta(r, \xi)\right], \tag{58}$$

where $\nu = \ell(\ell+1)$ for the bosonic sectors and $\nu = (\ell + \frac{1}{2})^2$ for the spinor sector, while $\Delta(r, \xi)$ collects derivative contributions involving the metric functions. Using the corre-

sponding metric components $A(r,\xi)$ and $B(r,\xi)$, we find that, for all perturbation types, the effective potentials admit the asymptotic expansion

$$\mathcal{V}(r,\ell,\xi) = \frac{\nu}{r^2} + \mathcal{O}(r^{-3}) + \mathcal{O}(\xi\, r^{-4}) + \cdots, \qquad r \to \infty. \tag{59}$$

Therefore, the higher-order curvature parameter ξ enters only through subleading terms in the far region, while the leading long-range behavior responsible for the late-time tails remains unchanged. As a consequence, the power-law decay exponents are expected to coincide with those of the corresponding General Relativity case, with ξ primarily affecting the amplitude of the tails and the transition time between the quasinormal ringing and the late-time regime. Moreover, notice that this interpretation is consistent with the numerical time-domain profiles obtained for all perturbation sectors.

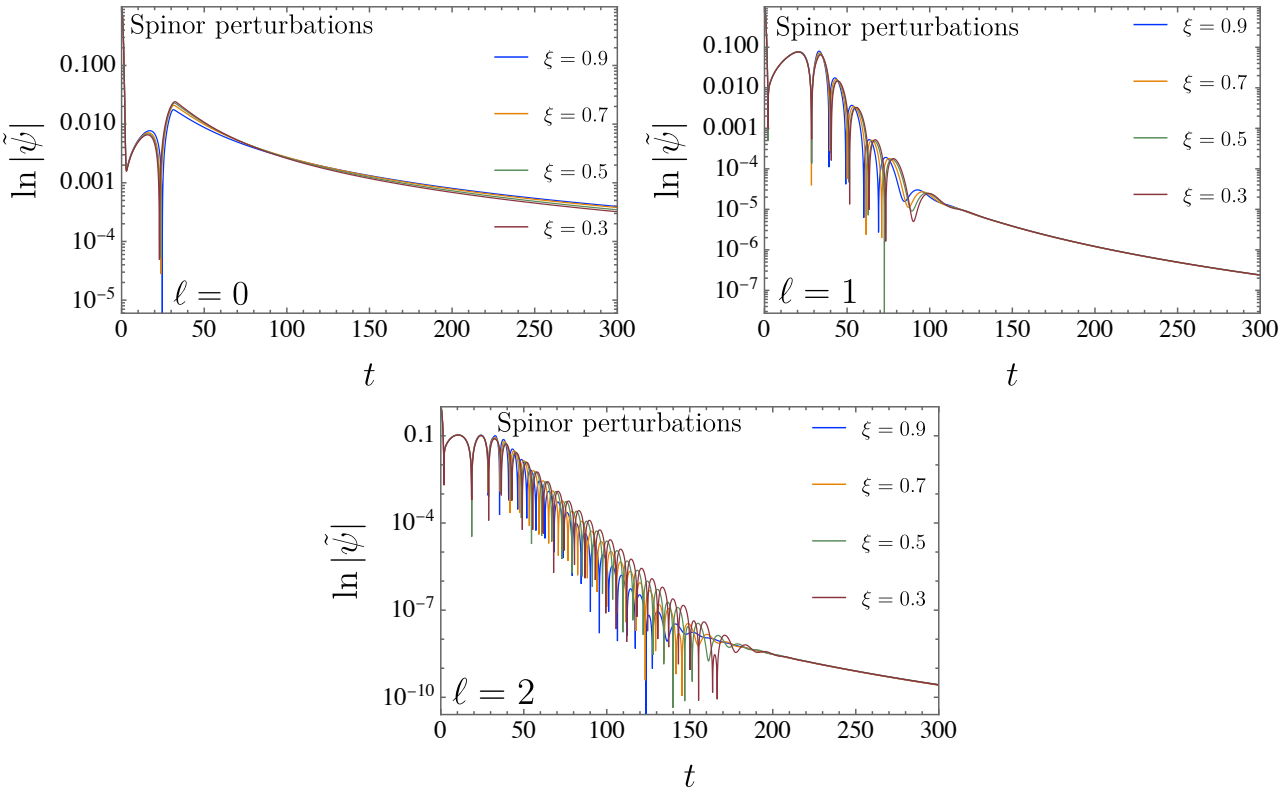

Figure 21. Logarithmic representation of the tensor perturbation, with $\ln|\tilde{\psi}|$ shown as a function of t for $M = 1$ and $\xi = 0.3, 0.5, 0.7$, and 0.9. The results are arranged by multipole number: $\ell = 0$ in the left panel, $\ell = 1$ in the right panel, and $\ell = 2$ in the bottom panel.

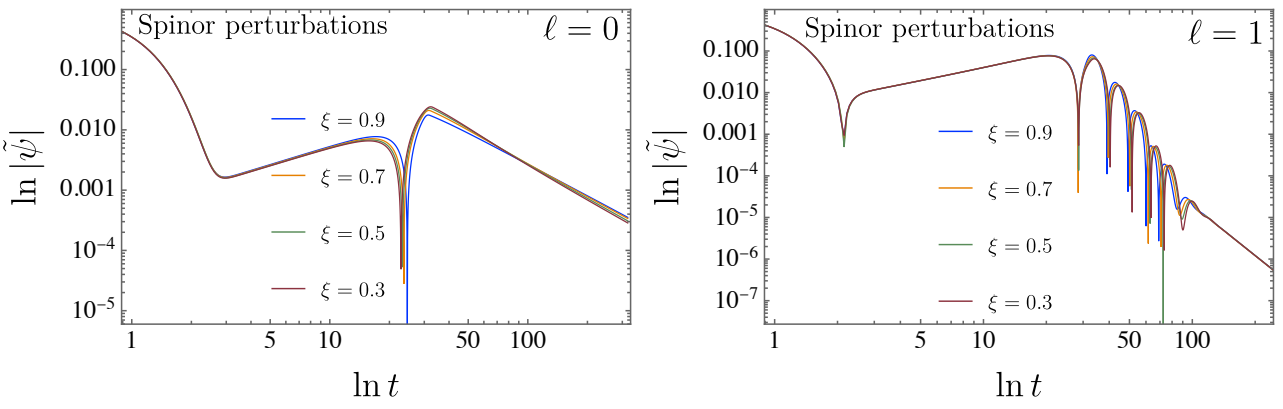

Figure 22. *Cont.*

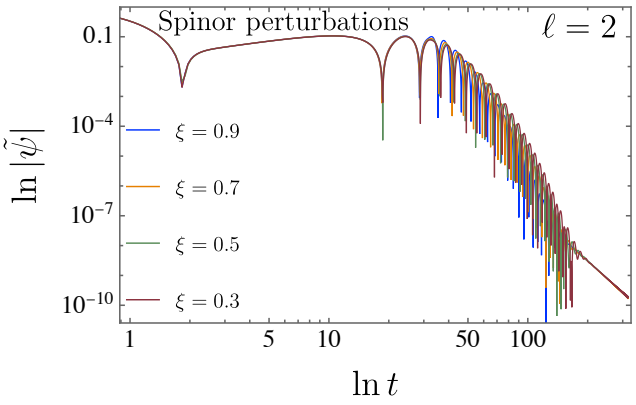

Figure 22. Late-time behavior of tensor perturbations shown in a double-logarithmic plot, with $\ln|\tilde{\psi}|$ versus $\ln t$ for $M = 1$ and $\xi = 0.3, 0.5, 0.7$, and 0.9. The panels correspond to: $\ell = 0$ (**left**), $\ell = 1$ (**right**), and $\ell = 2$ (**bottom**).

6. Geodesics

In gravitational physics, geodesics play a essential role by connecting the geometry of spacetime to the motion of free particles. When considered in the setting of higher-order curvature–scalar gravity, analyzing geodesic motion becomes a powerful tool to explore how the presence of curvature–scalar couplings reshapes the underlying geometry and influences particle trajectories. In the case of null geodesics, this approach is particularly effective for examining how the HOCG parameter ξ modifies light propagation and the causal structure of the spacetime.

Thereby, the geodesic equation takes the general form

$$\frac{\mathrm{d}^2 x^\mu}{\mathrm{dt}^2} + \Gamma^\mu_{\nu\lambda} \frac{\mathrm{d}x^\nu}{\mathrm{dt}} \frac{\mathrm{d}x^\lambda}{\mathrm{dt}} = 0. \tag{60}$$

Here, Γ denotes the Christoffel symbols and t is an affine parameter along the geodesic. The main objective is to investigate how the parameter ξ influences the motion of massless particles. This requires solving the coupled system of differential equations derived from Equation (60). The equation produces four separate relations, one for each spacetime coordinate, which must be integrated simultaneously using the metric given in Equation (7).

$$\frac{\mathrm{d}t'}{\mathrm{dt}} = -\frac{2r't'\left(Mr - \xi^2\right)}{r(-2Mr + \xi^2 + r^2)}, \tag{61}$$

$$\frac{\mathrm{d}r'}{\mathrm{dt}} = \frac{\left(2M\xi^{3/2} - 2Mr^3 + r^4\right)\left((t')^2(\xi^2 - Mr) + r^4\left((\theta')^2 + \sin^2(\theta)(\varphi')^2\right)\right)}{r^7} + \frac{M\left(r^3 - 4\xi^{3/2}\right)(r')^2}{-2Mr^4 + 2M\xi^{3/2}r + r^5}, \tag{62}$$

$$\frac{\mathrm{d}\theta'}{\mathrm{dt}} = \sin(\theta)\cos(\theta)\left(\varphi'\right)^2 - \frac{2\theta' r'}{r}, \tag{63}$$

$$\frac{\mathrm{d}\varphi'}{\mathrm{dt}} = -\frac{2\varphi'(r' + r\theta'\cot(\theta))}{r}, \tag{64}$$

with the prime ($'$) indicating derivatives taken with respect to the affine parameter.

Figure 23 displays the numerically integrated null geodesics for $M = 1$ with ξ varying from 0 to 0.5. The filled disk marks the event horizon, the dashed circles indicate the photon sphere, and the solid curves trace the light trajectories.

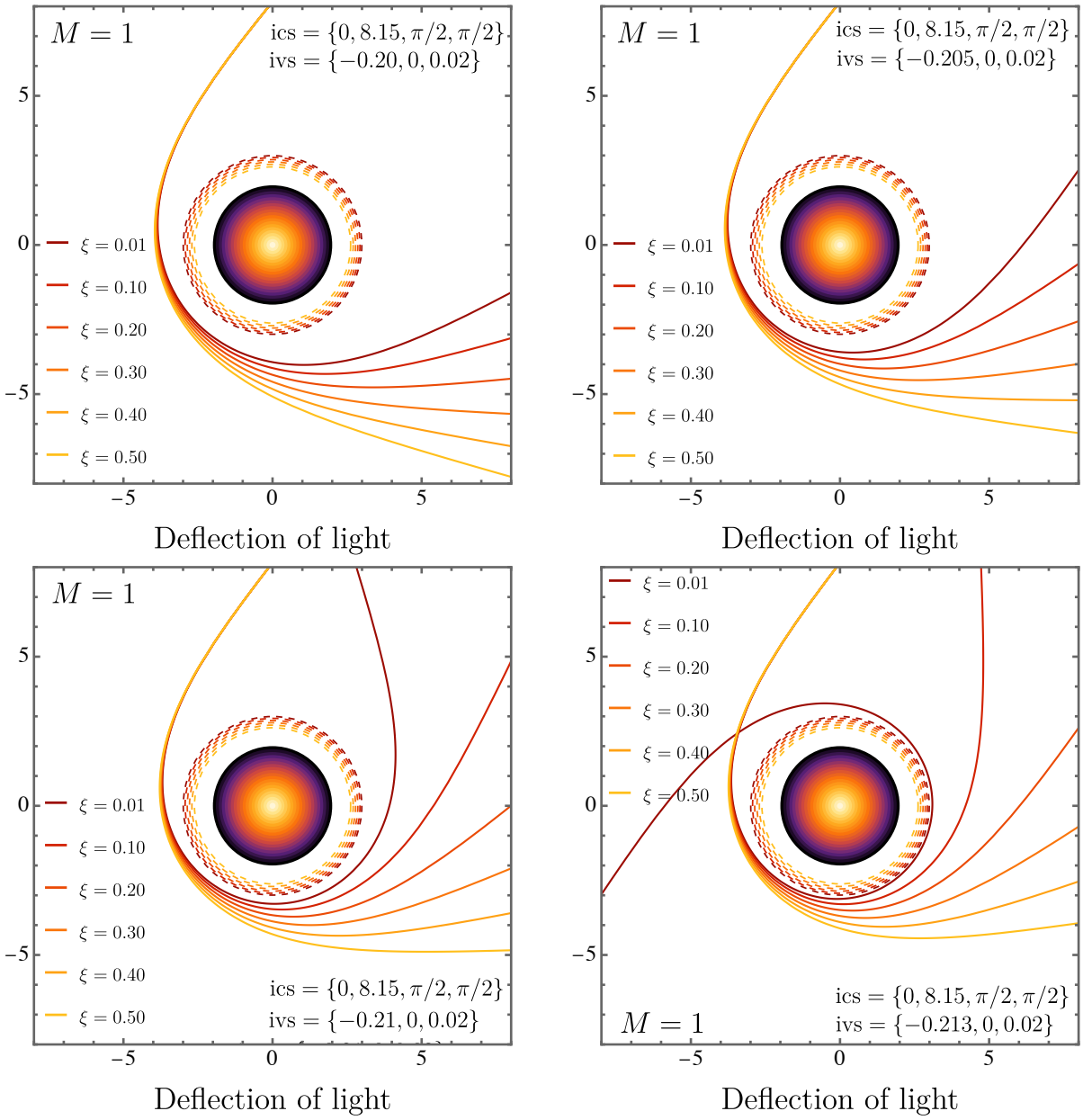

Figure 23. The geodesic trajectories are obtained through numerical integration using $M = 1$ and several choices of ξ. Dashed circles in the plots mark the locations of the corresponding photon spheres.

The results illustrate how photon paths respond to changes in the HOCG parameter ξ. As ξ decreases, light rays experience stronger bending, whereas larger values of ξ lead to trajectories that are less deflected, reflecting a weaker effective curvature near the black hole. This behavior signals that the parameter ξ directly modulates the gravitational field felt by photons, subtly modifying their propagation and thus influencing observable lensing patterns. These implications for gravitational lensing will be analyzed in detail in the next section.

7. Critical Orbits and Shadows

The study of black hole shadows has become a major focus in modern gravitational research [189–192], receiving renewed attention after the groundbreaking Event Horizon Telescope (EHT) images of $SgrA^*$ and $M87$ [193–195]. These observations have transformed shadows into a powerful method for testing strong-field gravity and probing the near-horizon structure of compact objects, for instance.

To investigate the shadow in the present context, we take the background metric given in Equation (7) as the starting point and analyze the propagation of photons through the Lagrangian formalism, expressed as

$$\mathcal{L} = \frac{1}{2} g_{\mu\nu} \dot{x}^{\mu} \dot{x}^{\nu}. \tag{65}$$

Equivalently, it can be written as

$$\mathcal{L} = \frac{1}{2}\Big[- A(r,\xi)\dot{t}^2 + \frac{1}{B(r,\xi)}\dot{r}^2 + C(r,\xi)\dot{\theta}^2 + D(r,\xi)\sin^2\theta\dot{\varphi}^2\Big]. \tag{66}$$

Using the Euler–Lagrange equations and restricting motion to the equatorial plane ($\theta = \pi/2$), one obtains two constants of motion, namely the conserved energy E and angular momentum L, as commonly reported in the literature. Their explicit forms are derived as

$$E = A(r,\xi)\dot{t} \quad \text{and} \quad L = D(r,\xi)\dot{\varphi}, \tag{67}$$

and taking into account solely the massless scenario, we obtain

$$-A(r,\xi)\dot{t}^2 + \frac{1}{B(r,\xi)}\dot{r}^2 + D(r,\xi)\dot{\varphi}^2 = 0. \tag{68}$$

Substituting the conserved quantities from Equation (67) into the null geodesic condition of Equation (68) and simplifying the equation leads to the following expression:

$$\frac{\dot{r}^2}{\dot{\varphi}^2} = \left(\frac{\mathrm{d}r}{\mathrm{d}\varphi}\right)^2 = D(r,\xi)B(r,\xi)\left(\frac{D(r,\xi)}{A(r,\xi)}\frac{E^2}{L^2} - 1\right). \tag{69}$$

In addition, we also have

$$\frac{\mathrm{d}r}{\mathrm{d}\lambda} = \frac{\mathrm{d}r}{\mathrm{d}\varphi}\frac{\mathrm{d}\varphi}{\mathrm{d}\lambda} = \frac{\mathrm{d}r}{\mathrm{d}\varphi}\frac{L}{D(r,\xi)}, \tag{70}$$

with

$$\dot{r}^2 = \left(\frac{\mathrm{d}r}{\mathrm{d}\lambda}\right)^2 = \left(\frac{\mathrm{d}r}{\mathrm{d}\varphi}\right)^2 \frac{L^2}{D(r,\xi)^2}, \tag{71}$$

which allows the effective potential $\mathrm{V}(\Theta,\ell)$ to be expressed in the form given by:

$$\mathrm{V}(r,\xi,\ell) = D(r,\xi)B(r,\xi)\left(\frac{D(r,\xi)}{A(r,\xi)}\frac{E^2}{L^2} - 1\right)\frac{L^2}{D(r,\xi)^2}. \tag{72}$$

Having set up the necessary framework, the next step is to locate the photon spheres. This is accomplished by applying the constraint

$$\mathrm{V}(r,\xi,\ell) = 0, \qquad \frac{\mathrm{d}\,\mathrm{V}(r,\xi,\ell)}{\mathrm{d}r} = 0. \tag{73}$$

Defining the critical impact parameter as $b_c = L/E$, the above requirement reduces to

$$b_c = \sqrt{\frac{D(r,\xi)}{A(r,\xi)}}\Big|_{r=r_{\mathrm{photon}}}. \tag{74}$$

Proceeding by inserting the expression for the impact parameter from Equation (74) into the effective potential of Equation (72) and then taking the derivative with respect to r, one arrives at:

$$\frac{\mathrm{d}\,\mathrm{V}(r,\xi,\ell)}{\mathrm{d}r} = \frac{B(r,\xi)\,L^2\Big[A(r,\xi)D'(r,\xi) - D(r,\xi)A'(r,\xi)\Big]}{A(r,\xi)D(r,\xi)^2}. \tag{75}$$

The next step involves imposing the condition $\frac{\mathrm{d}V(r,\xi,\ell)}{\mathrm{d}r} = 0$ to determine the allowed radii. Solving this equation yields six possible roots; however, only one is physically relevant, as it is both real, positive, and located outside the event horizon. This admissible solution is given by

$$r_{\text{photon}} = \frac{1}{2}\left(3M + \sqrt{9M^2 - 8\xi}\right), \tag{76}$$

where a restriction naturally arises due to the presence of the square root

$$9M^2 - 8\xi > 0, \tag{77}$$

to ensure that the solution remains real and positive (see the Table 7). In the limit $\xi \to 0$, the photon sphere coincides with the Schwarzschild value, $r_{\text{ph-Sch}} = 3M$, as expected. Moreover, Equation (76) bears a close resemblance to the expression for the photon sphere radius in the Reissner–Nordström spacetime, given by $r_{\text{ph-RN}} = \frac{1}{2}\left(3M + \sqrt{9M^2 - 8Q^2}\right)$.

Table 7. The critical photon orbit radii r_{photon} are listed for various choices of M and ξ.

ξ	M	r_{photon}	ξ	M	r_{photon}
0.1	1.0	2.93178	0.1	1.1	3.23824
0.2	1.0	2.86015	0.1	1.2	3.54356
0.3	1.0	2.78452	0.1	1.3	3.84803
0.4	1.0	2.70416	0.1	1.4	4.15183
0.5	1.0	2.61803	0.1	1.5	4.45511

We now turn to the analysis of the black hole shadow radius. For the spacetime under consideration, it can be expressed as

$$\begin{aligned} R &= \sqrt{\frac{D(r,\xi)}{A(r,\xi)}}\bigg|_{r=r_{\text{photon}}} = r^2_{\text{photon}}\sqrt{\frac{1}{-2Mr_{\text{photon}} + \xi + r^2_{\text{photon}}}} \\ &\approx 3\sqrt{3}M - \frac{\sqrt{3}\xi}{2M}. \end{aligned} \tag{78}$$

It is clear that the leading term in the expression corresponds to the Schwarzschild black hole result, while the remaining terms represent corrections arising from the presence of the parameter ξ in the metric of Equation (7).

In Table 8, we present the values of the shadow radii by taking into account different values of M and ξ. In a general panorama, we notice that when increasing ξ (keeping M fixed), the values of R decreases. On the other hand, when we keep ξ fixed, and vary M, R increases. In addition, to corroborate our interpretations, in Figure 24, we display the polar projection for the shadow radii, which are shown for diverse values of M and ξ. On the left side, M is considered fixed and ξ varies from 0.1 to 0.5. On the right side, ξ is kept constant while M varies from 1.1 to 1.5.

Table 8. The computed shadow radii R are reported for different combinations of M and ξ.

ξ	M	R	ξ	M	R
0.1	1.0	5.10955	0.1	1.1	5.63704
0.2	1.0	5.02295	0.1	1.2	6.16321
0.3	1.0	4.93634	0.1	1.3	6.68838
0.4	1.0	4.84974	0.1	1.4	7.21275
0.5	1.0	4.76314	0.1	1.5	7.73649

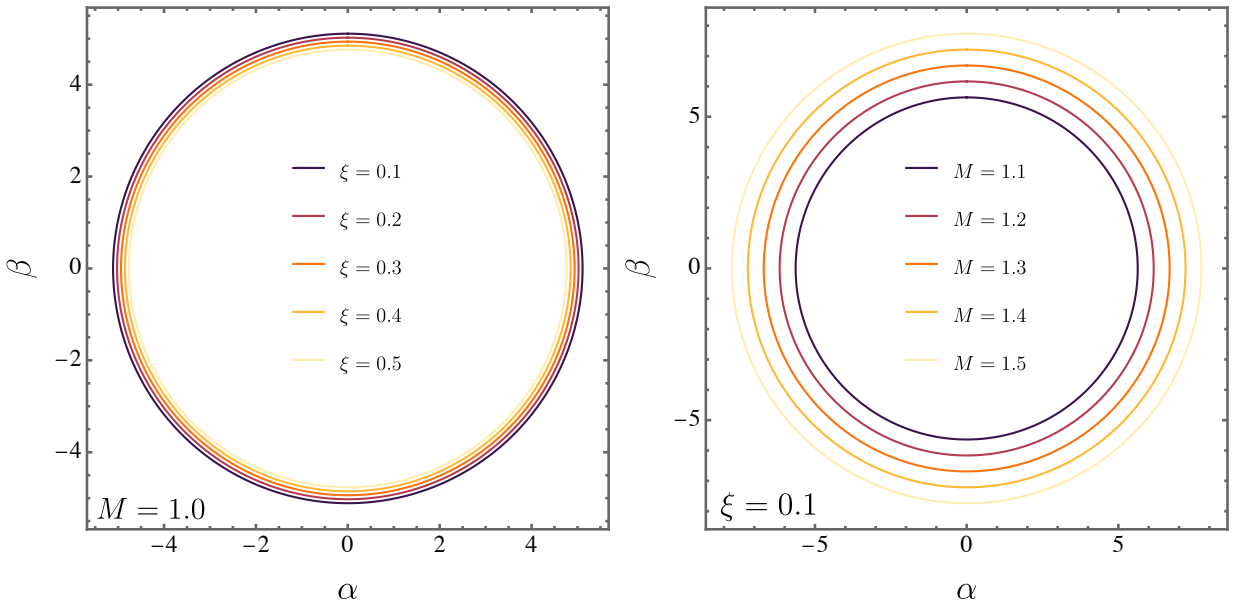

Figure 24. The shadow radius R is plotted for several combinations of M and ξ. In the left panel, M is held fixed while ξ ranges from 0.1 to 0.5, whereas in the right panel, ξ is kept constant and M is varied between 1.1 and 1.5.

8. Lensing Effects: Weak Field Approximation

This part of the work addresses gravitational lensing in the weak-deflection regime. The analysis is carried out using the Gauss–Bonnet method [196], which provides the basis for computing the corresponding deflection angle.

We begin by examining the stability of the photon spheres described in Equation (76). To this end, we compute the Gaussian curvature, which is essential in assessing the nature of the critical orbits. As will be shown, the sign of the curvature determines the stability: positive curvature indicates stable orbits, while negative curvature corresponds to instability.

8.1. Stability of the Critical Orbits

The behavior of photon rings (or critical orbits) around black holes is governed by the geometry of the optical manifold, whose curvature dictates the stability of circular light paths. The existence of conjugate points plays a decisive role in identifying whether such orbits are stable or unstable. Small perturbations prevent photons from staying on perfectly circular paths: in unstable configurations, they either plunge into the black hole or escape to infinity, whereas in stable configurations, the photons remain confined near their initial orbit, repeatedly circling in a localized region [197–200].

The stability of photon trajectories can be reformulated within a geometric framework, where the intrinsic properties of the optical manifold play essential roles. In particular, the Gaussian curvature $\mathcal{K}(r)$ dictates whether neighboring light rays converge or diverge along their paths. The Cartan–Hadamard theorem states that in regions with $\mathcal{K}(r) \leq 0$,

conjugate points do not arise, implying that circular photon paths are inherently unstable. When $\mathcal{K}(r) > 0$, however, conjugate points may exist, opening the possibility of localized, stable photon orbits [201]. Within this perspective, null geodesics satisfying $ds^2 = 0$ can be reformulated and expressed as [173]:

$$dt^2 = \tilde{\gamma}_{ij} dx^i dx^j = \frac{1}{A(r,\xi)\, B(r,\xi)} dr^2 + \frac{\bar{D}(r,\xi)}{A(r,\xi)} d\varphi^2. \tag{79}$$

In this setup, the indices i and j run over the spatial coordinates 1 to 3, and $\tilde{\gamma}_{ij}$ denotes the metric components of the associated optical space. The quantity $\bar{D}(r,\xi)$ is introduced as the metric function restricted to the equatorial plane, namely $\bar{D}(r,\xi) = D(r,\xi,\theta = \pi/2)$. With these definitions, the intrinsic curvature of the optical manifold is fully described by the Gaussian curvature, which takes the form provided in [201]:

$$\mathcal{K}(r,\xi) = \frac{R}{2} = -\frac{A(r,\xi)\sqrt{B(r,\xi)}}{\sqrt{\bar{D}(r,\xi)}} \frac{\partial}{\partial r}\left[\frac{A(r,\xi)\sqrt{B(r,\xi)}}{2\sqrt{\bar{D}(r,\xi)}} \frac{\partial}{\partial r}\left(\frac{\bar{D}(r,\xi)}{A(r,\xi)}\right)\right]. \tag{80}$$

Here, R represents the Ricci scalar calculated for the two-dimensional optical geometry. Considering the regime in which ξ is taken to be small, the curvature expression can be expanded accordingly, yielding

$$\begin{aligned}\mathcal{K}(r,\xi) = {} & \frac{3M^2}{r^4} - \frac{2M}{r^3} + \frac{2\xi}{r^3(r-2M)} + \frac{6M^2\xi}{r^5(r-2M)} - \frac{6M\xi}{r^4(r-2M)} \\ & + \frac{24M^3\xi^{3/2}}{r^7(r-2M)} - \frac{22M^2\xi^{3/2}}{r^6(r-2M)} + \frac{4M\xi^{3/2}}{r^5(r-2M)},\end{aligned} \tag{81}$$

where we have considered up to $\xi^{3/2}$. Two observations are in order here. First, the Gaussian curvature exhibits a divergence at $r = 2M$, which becomes evident when examining the denominator of several terms in Equation (81). Second, a closer inspection reveals that this singular behavior originates from the third contribution in $B(r,\xi)$, specifically the term $2M\xi^{3/2}/r^4$.

Previous works [197–202] emphasize that the Gaussian curvature $\mathcal{K}(r,\xi)$ is the quantity that dictates whether circular photon orbits persist or disperse under small perturbations. In other words, as briefly commented previously, positive curvature indicates that nearby geodesics converge, favoring stable closed photon loops, while negative curvature causes geodesic deviation to grow, destabilizing the orbit and leading to capture or escape.

This feature is visualized in Figure 25, where $\mathcal{K}(r,\xi)$ is plotted against r for the representative case $M = 1$ and $\xi = 0.001$. The plot shows two clearly separated domains: a region of confinement (shaded light pink) where stability is possible and another region (shaded light orange) where instability dominates. The zero of $\mathcal{K}$ occurs at approximately $r \approx 1.50$, acting as the dividing line between these two regimes. Because the photon sphere radius lies outside this critical point, all circular photon paths in this background are unstable.

8.2. Weak Deflection Angle

The weak-field deflection angle is obtained by employing the Gauss–Bonnet theorem [196], starting from the curvature expression provided in Equation (81). To implement this approach, the analysis is restricted to the equatorial plane, i.e., $\theta = \pi/2$, reducing the

optical geometry to a two-dimensional surface. In this reduced setup, the corresponding area element can be written as:

$$\mathrm{d}S = \sqrt{\tilde{\gamma}}\,\mathrm{d}r\mathrm{d}\varphi = \sqrt{\frac{1}{A(r,\xi)}\frac{1}{B(r,\xi)}\frac{D(r,\xi)}{A(r,\xi)}}\,\mathrm{d}r\mathrm{d}\varphi. \tag{82}$$

To perform the integration and compute the deflection angle, we adopt the same treatment for ξ as outlined in this work and consider the impact parameter in the regime $b \gg 2M$, consistent with the original formulation in Ref. [196], where the Gauss–Bonnet theorem was first applied to gravitational lensing. In this context, the mass parameter M is expanded up to second order, following the procedure commonly employed in related studies [29,202–204].

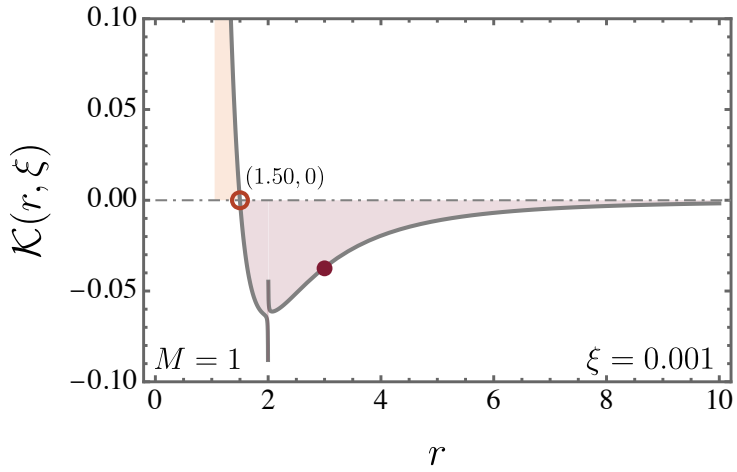

Figure 25. Gaussian curvature $\mathcal{K}(r,\xi)$ as a function of the radial coordinate r for $M = 1$ and $\xi = 0.001$. The red circle marks the radius where $\mathcal{K} = 0$, separating stable (on the left left) and unstable (on the right) photon regions, while the red dotted point indicates the photon sphere position r_{photon}, located in the unstable regime.

Using the previous relation as a starting point, the light deflection angle is given by:

$$\begin{aligned}\tilde{\alpha}(b,\xi) &= -\int\int_D \mathcal{K}\mathrm{d}S = -\int_0^{\pi}\int_{\left(\frac{\sin(\varphi)}{\beta}+\frac{\tilde{M}(1-\cos(\varphi))^2}{\beta^2}\right)^{-1}}^{\infty}\mathcal{K}\mathrm{d}S \\ &\simeq \frac{4M}{b}+\frac{15\pi M^2}{4b^2}-\frac{\pi\xi}{2b^2}-\frac{8M\xi}{b^3}-\frac{157\pi M^2\xi}{16b^4}-\frac{3\pi M\xi^{3/2}}{8b^4},\end{aligned} \tag{83}$$

where, again, we have considered up to $\xi^{3/2}$.

Equation (83) shows that the first two contributions on the second line reproduce the standard light-bending result for a Schwarzschild black hole, while the third, fourth, and fifth terms coincide, up to appropriate modifications of the constant factors, in line with the prediction for a Reissner–Nordström spacetime. The remaining terms encode the effects of the higher-order curvature–scalar modifications introduced in this work, incorporating various powers of the parameter ξ.

Figure 26 illustrates how the deflection angle $\tilde{\alpha}(b,\xi)$ varies with the black hole parameters. For a fixed impact parameter, e.g., $b = 2$, an increase in ξ leads to a reduction in the deflection angle. This behavior is corroborated by the geodesic analysis shown in Figure 23, where larger values of ξ render the light trajectories progressively more "open." Moreover, as shown in the next section, the same trend persists in the strong-deflection regime.

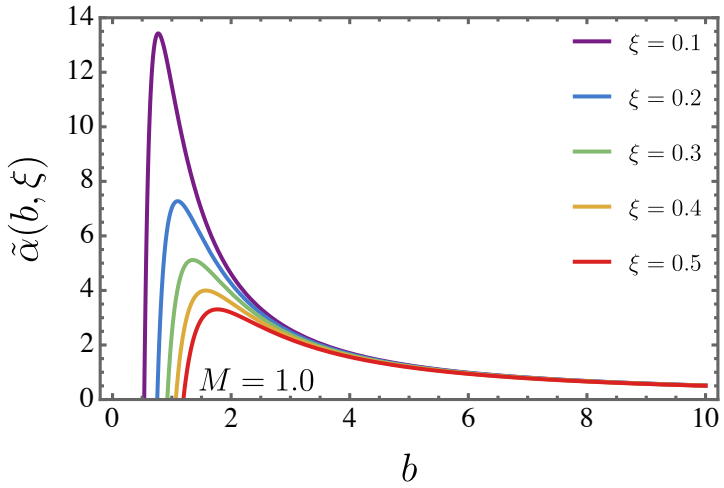

Figure 26. Deflection angle $\tilde{\alpha}(b,\xi)$ is plotted with respect to the impact parameter b for several choices of ξ, with the black hole mass kept fixed at $M = 1$.

9. Lensing Effects: Strong-Field Approximation

This section focuses on deriving the light-bending angle in the strong-field regime. Adopting the methodology used in several recent works [132,134,203,205], the computation was carried out assuming a static, spherically symmetric spacetime that becomes asymptotically flat at large r. The corresponding line element characterizing the background geometry takes the form [206]

$$ds^2 = -\tilde{A}(r)dt^2 + \tilde{B}(r)dr^2 + \tilde{C}(r)(d\theta^2 + \sin^2\theta d\phi^2). \tag{84}$$

To apply the analytical method proposed by Tsukamoto [206], the spacetime under consideration was required to satisfy asymptotic flatness. This condition enforces that, in the limit $r \to \infty$, the metric functions approach well-defined forms: $\tilde{A}(r)$ and $\tilde{B}(r)$ tend toward unity, while $\tilde{C}(r)$ grows as r^2, namely,

$$\lim_{r\to\infty} \tilde{A}(r) = 1, \quad \lim_{r\to\infty} \tilde{B}(r) = 1, \quad \lim_{r\to\infty} \tilde{C}(r) = r^2.$$

The calculation of the strong-field deflection angle begins by introducing an auxiliary function $\tilde{\tilde{D}}(r)$ to reformulate the radial dependence. This redefinition regularizes the expression close to the photon sphere and simplifies the analysis, allowing the light trajectory to be treated analytically without divergences dominating the result.

$$\tilde{\tilde{D}}(r) \equiv \frac{\tilde{C}'(r)}{\tilde{C}(r)} - \frac{\tilde{A}'(r)}{\tilde{A}(r)}, \tag{85}$$

where the primes indicate differentiation with respect to r. The auxiliary function $\tilde{\tilde{D}}(r)$ is constructed so that it possesses at least one positive root, and the photon sphere is determined by selecting the largest of these roots, denoted as r_{photon}. To ensure the validity of the formalism in this regime, the metric functions $\tilde{A}(r)$, $\tilde{B}(r)$, and $\tilde{C}(r)$ must stay smooth and strictly positive for all $r \geq r_{\text{photon}}$.

Because the background is invariant under time translations and rotations around the symmetry axis, null geodesics admit two constants of motion. The first is the energy, $E = \tilde{A}(r)\dot{t}$, and the second is the angular momentum, $L = \tilde{C}(r)\dot{\phi}$. When both quantities are nonzero, their ratio defines the impact parameter

$$b \equiv \frac{L}{E} = \frac{\tilde{C}(r)\dot{\phi}}{\tilde{A}(r)\dot{t}}. \tag{86}$$

Exploiting the axial symmetry of the metric allows the motion to be restricted to the equatorial plane by fixing $\theta = \pi/2$, which does not affect the generality of the solution. With this simplification, the equation describing the radial evolution of light-like geodesics takes the form

$$\dot{r}^2 = V(r). \tag{87}$$

Now, let us define the effective potential for photon motion as

$$V(r) = \frac{L^2\,\mathcal{R}(r)}{\tilde{\mathrm{B}}(r)\,\tilde{\mathrm{C}}(r)}, \qquad \text{and} \qquad \mathcal{R}(r) = \frac{\tilde{\mathrm{C}}(r)}{\tilde{\mathrm{A}}(r)b^2} - 1.$$

This expression plays the role of a radial potential for massless particles. The physically accessible domain is determined by the requirement $V(r) \geq 0$. Because the geometry becomes flat at large r, the potential approaches E^2 as $r \to \infty$, meaning photons can escape to infinity. Additionally, $\mathcal{R}(r) = 0$ is assumed to admit at least one positive real root, which sets the turning point of the trajectory.

In the context of gravitational lensing, the null geodesic of interest originates from spatial infinity, approaches the compact object, reaches a minimum radial distance r_{o}, and then travels back out to infinity. This turning point r_{o} must lie outside the photon sphere radius r_{photon}, ensuring that the trajectory does not correspond to a circular orbit. Mathematically, r_{o} is identified as the largest real root of $\mathcal{R}(r) = 0$, provided that $\tilde{\mathrm{B}}(r)$ and $\tilde{\mathrm{C}}(r)$ are finite and positive there. At this radius, the effective potential satisfies $V(r_{\mathrm{o}}) = 0$, making $\mathcal{R}(r_{\mathrm{o}}) = 0$ the fundamental condition defining the closest approach:

$$\tilde{\mathrm{A}}_{\mathrm{o}}\dot{t}_{\mathrm{o}}^2 = \tilde{\mathrm{C}}_{\mathrm{o}}\dot{\phi}_{\mathrm{o}}^2. \tag{88}$$

Hereafter, the following quantities carrying the subscript "o" are to be considered at the turning point $r = r_{\mathrm{o}}$. For the analysis of an individual photon trajectory, it is sufficient to consider a positive impact parameter b, as negative values merely reverse the direction of motion. Because b remains constant along the entire geodesic, it can be expressed as

$$b(r_{\mathrm{o}}) = \frac{L}{E} = \frac{\tilde{\mathrm{C}}_{\mathrm{o}}\dot{\phi}_{\mathrm{o}}}{\tilde{\mathrm{A}}_{\mathrm{o}}\dot{t}_{\mathrm{o}}} = \sqrt{\frac{\tilde{\mathrm{C}}_{\mathrm{o}}}{\tilde{\mathrm{A}}_{\mathrm{o}}}}. \tag{89}$$

It is important to note that $\mathcal{R}(r)$ can equivalently be expressed in the following form:

$$\mathrm{R}(r) = \frac{\tilde{\mathrm{A}}_{\mathrm{o}}\tilde{\mathrm{C}}(r)}{\tilde{\mathrm{A}}(r)\tilde{\mathrm{C}}_{\mathrm{o}}} - 1. \tag{90}$$

The condition that guarantees the presence of a circular null geodesic can be formulated using the approach described in Ref. [207]. Within this formalism, the photon trajectory is governed by the relation

$$\frac{\tilde{\mathrm{B}}(r)\,\tilde{\mathrm{C}}(r)\,\dot{r}^2}{E^2} + b^2 = \frac{\tilde{\mathrm{C}}(r)}{\tilde{\mathrm{A}}(r)}, \tag{91}$$

in a such way that we can write

$$\ddot{r} + \frac{1}{2}\left(\frac{\tilde{\mathrm{B}}(r)'}{\tilde{\mathrm{B}}(r)} + \frac{\tilde{\mathrm{C}}(r)'}{\tilde{\mathrm{C}}(r)}\dot{r}^2\right) = \frac{E^2\tilde{\tilde{D}}(r)}{\tilde{\mathrm{A}}(r)\tilde{\mathrm{B}}(r)}. \tag{92}$$

For radii satisfying $r \geq r_{\mathrm{photon}}$, the metric components $\tilde{\mathrm{A}}(r)$, $\tilde{\mathrm{B}}(r)$, and $\tilde{\mathrm{C}}(r)$ are required to remain smooth and strictly positive. With $E > 0$, the condition $\tilde{\tilde{D}}(r) = 0$ serves

as the criterion for the presence of a circular photon orbit. Additionally, evaluating the derivative of $\mathcal{R}(r)$ at the photon sphere yields

$$\mathcal{R}'_{\rm photon} = \frac{\tilde{\tilde{D}}_{\rm photon}\tilde{C}_{\rm photon}\tilde{A}_{\rm photon}}{b^2} = 0,$$

where the subscript "photon" indicates that all quantities are taken at $r = r_{\rm photon}$.

The next step is addressing the threshold value of the impact parameter, denoted as b_c, which separates photons that are scattered from those that spiral toward the photon sphere:

$$b_c(r_{\rm photon}) \equiv \lim_{r_{\rm o}\to r_{\rm photon}} \sqrt{\frac{\tilde{C}_{\rm o}}{\tilde{A}_{\rm o}}}. \tag{93}$$

Notice that this domain is identified as the strong-deflection regime. Taking the derivative of the effective potential $V(r)$ with respect to r leads to the condition

$$V'(r) = \frac{L^2}{\tilde{B}(r)\tilde{C}(r)}\left[\mathrm{R}(r)' + \left(\frac{\tilde{C}'(r)}{\tilde{C}(r)} - \frac{\tilde{B}'(r)}{\tilde{B}(r)}\right)\mathrm{R}(r)\right]. \tag{94}$$

Within such a regime, as the closest approach radius $r_{\rm o}$ approaches the critical orbit $r_{\rm photon}$, $V(r_{\rm o})$ and its derivative $V'(r_{\rm o})$ vanish all at once. Under these circumstances, the null geodesic equation simplifies to

$$\left(\frac{\mathrm{d}r}{\mathrm{d}\phi}\right)^2 = \frac{\mathrm{R}(r)\tilde{C}(r)}{\tilde{B}(r)}. \tag{95}$$

Consequently, the light-bending angle associated with a trajectory reaching the closest approach $r_{\rm o}$ can be written in the form

$$\alpha(r_{\rm o}) = I(r_{\rm o}) - \pi, \tag{96}$$

in which $I(r_{\rm o})$ reads as

$$I(r_{\rm o}) \equiv 2\int_{r_{\rm o}}^{\infty} \frac{\mathrm{d}r}{\sqrt{\frac{\mathrm{R}(r)\tilde{C}(r)}{\tilde{B}(r)}}}. \tag{97}$$

The evaluation begins by tackling the integral that defines the deflection angle—an operation known for its analytical complexity, as emphasized by Tsukamoto [206]. To facilitate this calculation, we introduce the auxiliary quantity defined in [206]:

$$z \equiv 1 - \frac{r_{\rm o}}{r}. \tag{98}$$

This redefinition makes it possible to rewrite the integral in the following form:

$$I(r_{\rm o}) = \int_0^1 f(z, r_{\rm o})\mathrm{d}z, \tag{99}$$

or, in other words,

$$f(z, z_0) \equiv \frac{2r_{\rm o}}{\sqrt{G(z, r_{\rm o})}}, \quad \text{and} \quad G(z, r_{\rm o}) \equiv \mathrm{R}(r)\frac{\tilde{C}(r)}{\tilde{B}(r)}(1-z)^4. \tag{100}$$

Alternatively, when rewritten using the variable z, the function $\mathcal{R}(r)$ therefore becomes

$$\mathrm{R}(r) = \tilde{\tilde{D}}_{\rm o}\, r_{\rm o} z + \left[\frac{r_{\rm o}}{2}\left(\frac{\tilde{C}''_{\rm o}}{\tilde{C}_{\rm o}} - \frac{\tilde{A}''_{\rm o}}{\tilde{A}_{\rm o}}\right) + \left(1 - \frac{\tilde{A}'_{\rm o} r_{\rm o}}{\tilde{A}_{\rm o}}\right)\tilde{\tilde{D}}_{\rm o}\right] r_{\rm o} z^2 + \mathcal{O}(z^3) + \ldots \ . \tag{101}$$

Expanding $G(z, r_o)$ in a Taylor series about $z = 0$ yields the following expression:

$$G(z, r_o) = \sum_{n=1}^{\infty} c_n(r_o) z^n, \tag{102}$$

where we can identify $c_1(r)$ and $c_2(r)$ as

$$c_1(r_o) = \frac{\tilde{C}_o \tilde{D}_o r_o}{\tilde{B}_o}, \tag{103}$$

and

$$c_2(r_o) = \frac{\tilde{C}_o r_o}{\tilde{B}_o}\left\{\tilde{\tilde{D}}_o\left[\left(\tilde{\tilde{D}}_o - \frac{\tilde{B}'_o}{\tilde{B}_o}\right) r_o - 3\right] + \frac{r_o}{2}\left(\frac{\tilde{C}''_o}{\tilde{C}_o} - \frac{\tilde{A}''_o}{\tilde{A}_o}\right)\right\}. \tag{104}$$

Moreover, applying the strong-deflection approximation leads to the result

$$c_1(r_{photon}) = 0, \quad \text{and} \quad c_2(r_{photon}) = \frac{\tilde{C}_{photon} r^2_{photon}}{2\tilde{B}_{photon}} \tilde{\tilde{D}}'_{photon}, \quad \text{with} \quad \tilde{\tilde{D}}'_{photon} = \frac{\tilde{C}''}{\tilde{C}_{photon}} - \frac{\tilde{A}''}{\tilde{A}_{photon}}, \tag{105}$$

where $G(z, r_o)$ can be rewritten in a simplified form as

$$G_{photon}(z) = c_2(r_{photon}) z^2 + \mathcal{O}(z^3). \tag{106}$$

When the closest approach radius r_o tends to the photon sphere r_{photon}, the function $f(z, r_o)$ develops a singularity whose leading term behaves as $1/z$. This singular nature causes the integral $I(r_o)$ to diverge logarithmically. To handle this, the integral is decomposed into two parts: a divergent contribution, $I_{Div}(r_o)$, which isolates the $1/z$ behavior, and a regular part, $I_{Reg}(r_o)$, which stays finite. The divergent term can then be written as

$$I_{Div}(r_o) \equiv \int_0^1 f_{Div}(z, r_o) \mathrm{d}z, \quad \text{with} \quad f_{Div}(z, r_o) \equiv \frac{2r_o}{\sqrt{c_1(r_o) z + c_2(r_o) z^2}}. \tag{107}$$

Carrying out the integration yields the following expression:

$$I_{Div}(r_o) = \frac{4r_o}{\sqrt{c_2(r_o)}} \ln\left[\frac{\sqrt{c_2(r_o)} + \sqrt{c_1(r_o) + c_2(r_o)}}{\sqrt{c_1(r_o)}}\right]. \tag{108}$$

Furthermore, a Taylor expansion of $c_1(r_o)$ and $b(r_o)$ about $r_o = r_{photon}$ gives

$$c_1(r_o) = \frac{\tilde{C}_{photon} r_{photon} \tilde{\tilde{D}}'_{photon}}{\tilde{B}_{photon}} (r_o - r_{photon}) + \mathcal{O}((r_o - r_{photon})^2), \tag{109}$$

and

$$b(r_o) = b_c(r_{photon}) + \frac{1}{4}\sqrt{\frac{\tilde{C}_{photon}}{\tilde{A}_{photon}}} \tilde{\tilde{D}}'_{photon} (r_o - r_{photon})^2 + \mathcal{O}((r_o - r_{photon})^3), \tag{110}$$

which results in:

$$\lim_{r_o \to r_{photon}} c_1(r_o) = \lim_{b \to b_c} \frac{2\tilde{C}_{photon} r_{photon} \sqrt{\tilde{\tilde{D}}'}}{\tilde{B}_{photon}} \left(\frac{b}{b_c} - 1\right)^{1/2}. \tag{111}$$

With these expansions, the divergent part of the integral $I_{Div}(b)$ can be expressed as

$$I_{\text{Div}}(b) = -\frac{r_{\text{photon}}}{\sqrt{c_2(r_{\text{photon}})}} \ln\left[\frac{b}{b_c} - 1\right] + \frac{r_{\text{photon}}}{\sqrt{c_2(r_{\text{photon}})}} \ln\left[r^2 \tilde{D}'_{\text{photon}}\right] + \mathcal{O}[(b - b_c)\ln(b - b_c)]. \tag{112}$$

Moreover, the finite (regular) contribution is defined by

$$I_{\text{Reg}}(b) = \int_1^0 f_{\text{Reg}}(z, b_c)\mathrm{d}z + \mathcal{O}[(b - b_c)\ln(b - b_c)]. \tag{113}$$

Introduce the function f_{Reg} by subtracting the divergent part from the full expression,

$$f_{\text{Reg}} = f(z, r_{\text{o}}) - f_{\text{Div}}(z, r_{\text{o}}).$$

Using this regularized quantity and working within the strong-deflection approximation, the resulting expression for the deflection angle becomes

$$a(b) = -\tilde{a}\ln\left[\frac{b}{b_c} - 1\right] + \tilde{b} + \mathcal{O}[(b - b_c)\ln(b - b_c)], \tag{114}$$

where we have particularly considered

$$\tilde{a} = \sqrt{\frac{2\,\tilde{\mathrm{B}}_{\text{photon}}\tilde{\mathrm{A}}_{\text{photon}}}{\tilde{\mathrm{C}}''_{\text{photon}}\tilde{\mathrm{A}}_{\text{photon}} - \tilde{\mathrm{C}}_{\text{photon}}\tilde{\mathrm{A}}''_{\text{photon}}}}, \tag{115}$$

and

$$\tilde{b} = \tilde{a}\ln\left[r^2_{\text{photon}}\left(\frac{\tilde{\mathrm{C}}''_{\text{photon}}}{\tilde{\mathrm{C}}_{\text{photon}}} - \frac{\tilde{\mathrm{A}}''_{\text{photon}}}{\tilde{\mathrm{C}}_{\text{photon}}}\right)\right] + I_{\text{Reg}}(r_{\text{photon}}) - \pi. \tag{116}$$

In the following subsection, the formalism developed above is applied to the specific black hole geometry given in Equation (7).

Bending Angle of a Black Hole in Higher-Order Curvature–Scalar Gravity

Here, it is worth emphasizing that, as in the previous sections, all calculations are carried out up to order $\xi^{3/2}$. With the general formalism in place, the next step is to specialize the analysis to the spacetime defined by Equation (7). Substituting this metric into Equation (89) yields the explicit expression for the impact parameter:

$$b_c \approx\ 3\sqrt{3}M - \frac{\sqrt{3}\xi}{2M}, \tag{117}$$

In this derivation, the result was expanded perturbatively, keeping terms up to ξ^2. Additionally, the parameters $\tilde{a}$ and $\tilde{b}$ are expressed explicitly as

$$\tilde{a} = 1 + \frac{5\xi}{18M^2} - \frac{\xi^{3/2}}{27M^3}. \tag{118}$$

Consequently, the relation can be rewritten in the following form:

$$\begin{aligned}\tilde{b} = &\left(1 + \frac{5\xi}{18M^2} - \frac{\xi^{3/2}}{27M^3}\right)\left(\ln[6] - \frac{\xi}{9M^2}\right)\\ &+ I_{\text{Reg}}(r_{\text{photon}}) - \pi.\end{aligned} \tag{119}$$

Unlike the Schwarzschild scenario, where $\tilde{a}$ has a simpler dependence, here its value is largely dictated by the effects ascribed to ξ. Moreover, the expression for the regular part of the integral, evaluated at $r = r_{\text{photon}}$, can be written as

$$
\begin{aligned}
&I_{\text{Reg}}(r_{\text{photon}}) = \\
&\int_0^1 \mathrm{d}z \left\{ \frac{2}{\sqrt{1-\frac{2z}{3}z}} + \frac{\xi(4z(2z-5)+15)}{3\sqrt{3}M^2(3-2z)^{3/2}z(2z+1)} - \frac{5\xi}{9M^2 z} - \frac{2\xi^{3/2}(z-1)^4}{9M^3\sqrt{9-6z}z(2z+1)} - \frac{2}{z}\frac{2\xi^{3/2}}{27M^3 z} \right\} \\
&= \ln[36] + \ln\left[7-4\sqrt{3}\right] - \frac{3\sqrt{3}\xi^{3/2}\coth^{-1}[2]}{8M^3} - \frac{\xi}{18M^2} + \frac{\xi}{6\sqrt{3}M^2} + \frac{5\xi\ln[3]}{9M^2} \\
&+ \frac{10\xi\ln\left[\sqrt{3}-1\right]}{9M^2} - \frac{3\sqrt{3}\xi\ln\left[\sqrt{3}+2\right]}{4M^2} + \frac{3\sqrt{3}\xi\coth^{-1}[2]}{4M^2} \\
&+ \frac{3\sqrt{3}\xi^{3/2}}{20M^3} - \frac{11\xi^{3/2}}{20M^3} + \frac{3\sqrt{3}\xi^{3/2}\ln\left[\sqrt{3}+2\right]}{8M^3} - \frac{2\xi^{3/2}\ln[3]}{27M^3} - \frac{4\xi^{3/2}\ln\left[\sqrt{3}-1\right]}{27M^3}.
\end{aligned}
\tag{120}
$$

This procedure yields a closed-form analytic result. An additional observation is that the regular contribution $I_{\text{Reg}}(r_{\text{photon}})$ in this spacetime coincides with its Schwarzschild counterpart plus extra terms proportional to ξ, as anticipated. Using this expression in Equation (114), the deflection angle in the strong-field regime is finally obtained as

$$
\begin{aligned}
a(b,\xi) = &-\left(1+\frac{5\xi}{18M^2}-\frac{\xi^{3/2}}{27M^3}\right)\times\ln\left[\frac{b}{3\sqrt{3}M-\frac{\sqrt{3}\xi}{2M}}-1\right] \\
&+\left(1+\frac{5\xi}{18M^2}-\frac{\xi^{3/2}}{27M^3}\right)\left(\ln[6]-\frac{\xi}{9M^2}\right)-\pi \\
&+\ln[36]+\ln\left[7-4\sqrt{3}\right]-\frac{3\sqrt{3}\xi^{3/2}\coth^{-1}[2]}{8M^3}-\frac{\xi}{18M^2}+\frac{\xi}{6\sqrt{3}M^2}+\frac{5\xi\ln[3]}{9M^2} \\
&+\frac{10\xi\ln\left[\sqrt{3}-1\right]}{9M^2}-\frac{3\sqrt{3}\xi\ln\left[\sqrt{3}+2\right]}{4M^2}+\frac{3\sqrt{3}\xi\coth^{-1}[2]}{4M^2} \\
&+\frac{3\sqrt{3}\xi^{3/2}}{20M^3}-\frac{11\xi^{3/2}}{20M^3}+\frac{3\sqrt{3}\xi^{3/2}\ln\left[\sqrt{3}+2\right]}{8M^3}-\frac{2\xi^{3/2}\ln[3]}{27M^3}-\frac{4\xi^{3/2}\ln\left[\sqrt{3}-1\right]}{27M^3} \\
&+\mathcal{O}\left\{\left[b-\left(3\sqrt{3}M-\frac{\sqrt{3}\xi}{2M}\right)\right]\times\ln\left[b-\left(3\sqrt{3}M-\frac{\sqrt{3}\xi}{2M}\right)\right]\right\}.
\end{aligned}
\tag{121}
$$

For better visualization, Figure 27 shows how the deflection angle varies with the impact parameter b for several parameter choices. The plots reveal that larger values of ξ fundamentally reduce $a(b,\xi)$. This behavior aligns with the geodesic results in Figure 23, where light rays move far away to the photon sphere as ξ grows. Additionally, to reinforce the conclusions drawn in the strong-deflection regime, the next subsection turns to phenomenological aspects, emphasizing observable quantities that can be compared with Event Horizon Telescope (EHT) measurements.

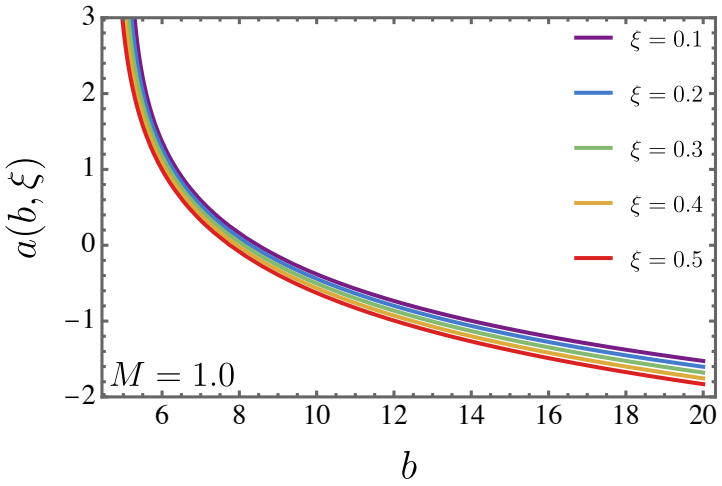

Figure 27. Deflection angle $a(b,\xi)$ is plotted with respect to the impact parameter b for several choices of ξ, with the mass parameter fixed at $M = 1$.

10. Lensing Observables

The shadow observations of $SgrA^*$ and $M87^*$ by the Event Horizon Telescope (EHT) [5,195,208,209] provide a natural testing ground for higher-order curvature–scalar gravity. In this framework, the HOCG parameter ξ modifies the photon sphere structure and therefore the shadow diameter. By confronting the theoretical predictions with the EHT data, one can delineate the observationally consistent range of ξ.

One of the relevant observables is the angular shadow diameter, $\Omega_{\rm sh}$, given in terms of the critical impact parameter b_c and the observer's distance $\mathcal{D}$ as [111,210,211]

$$\Omega_{\rm sh} = \frac{2b_c}{\mathcal{D}}. \tag{122}$$

In observational units, it can be expressed as [212,213]

$$\Omega_{\rm sh} = \frac{6.191165 \times 10^{-8}\gamma}{\pi\mathcal{D}/{\rm Mpc}} \frac{b_c}{M}\,(\mu{\rm as}), \tag{123}$$

where γ is the mass ratio of the black hole to the Sun. Now we check the impact of the HOCG parameter on the angular shadow diameter with both $SgrA^*$ and $M87^*$ data.

*10.1. Constraints with Image of M87**

The EHT collaboration reports the mass and distance of $M87^*$ to be $M \simeq 6.5 \times 10^9 M_\odot$ and $\mathcal{D} = 16.8$ Mpc, respectively [214–216]. Moreover, the angular diameter of the supermassive black hole $M87^*$ has been measured by EHT as 42 ± 3 μas [195,217]. Utilizing $M87^*$ parameters in Equation (123) and expanding up to order $\xi^{3/2}$ yields the following equation:

$$\Omega_{\rm sh}^{M87^*} = 39.61199 - 6.60199\left(\frac{\xi}{M^2}\right). \tag{124}$$

The relationship between $\Omega_{\rm sh}$ and ξ/M^2, shown in Figure 28, reveals a decreasing angular shadow size for increasing values of the HOCG parameter. The theoretical prediction falls below the EHT observational limit of 39.00 μas for $\xi/M^2 > 0.091$. Consequently, to remain consistent with the EHT results, the parameter ξ/M^2 is constrained to the range $0 \leq \xi/M^2 \lesssim 0.091$ for M87*.

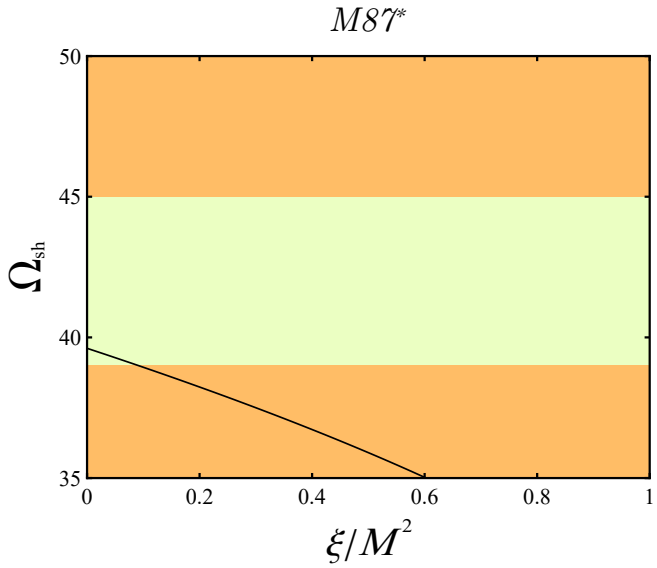

Figure 28. Angular shadow diameter Ω_{sh} of $M87^*$ as a function of the scaled HOCG parameter ξ/M^2. The green band indicates the EHT observational bounds.

10.2. Constraints with Image of $SgrA^*$

Based on the most recent measurements, the Gravity collaboration reports the mass of $SgrA^*$ to be $M = 4 \times 10^6 M_\odot$ and its distance to be $\mathcal{D} = 8.15$ kpc [218–220]. On the other hand, the EHT collaboration reports $\Omega_{sh} = 48.7 \pm 7$ μas [208,209], corresponding to an observational window of $41.7 \leq \Omega_{sh} \leq 55.7$ μas. Substituting the $SgrA^*$ property in Equation (123), and expanding it up to order $\xi^{3/2}$, results in the following expression:

$$\Omega_{sh}^{SgrA^*} = 53.23368 - 8.87226\left(\frac{\xi}{M^2}\right). \tag{125}$$

The theoretical prediction of $\Omega_{sh}^{SgrA^*}$ with respect to the HOCG parameter in the mass unit is displayed in Figure 29. The allowed range of angular diameter based on $SgrA^*$ is represented by the green region. We find that Ω_{sh} decreases monotonically with increasing ξ/M^2. A critical restriction point occurs at $\xi/M^2 \simeq 0.963$. For $\xi > 0.963M^2$, the predicted shadow size drops below the EHT lower bound of 41.7 μas and is therefore observationally excluded. This yields the constraint $0 \leq \xi/M^2 \lesssim 0.963$ for $SgrA^*$.

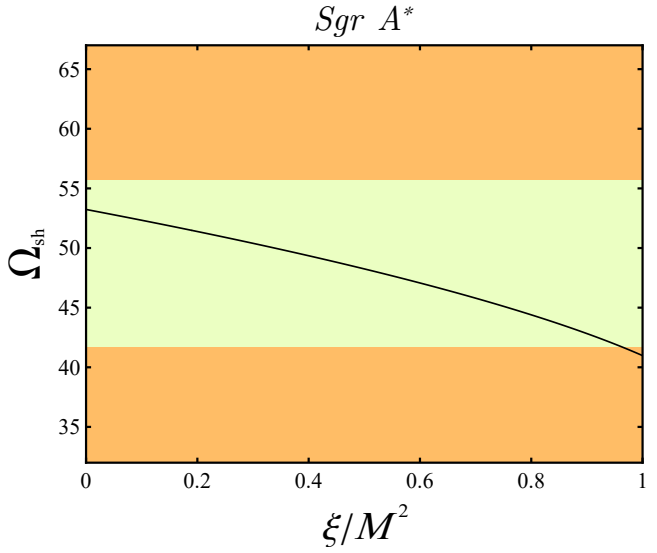

Figure 29. Angular shadow diameter Ω_{sh} of $SgrA^*$ as a function of the scaled HOCG parameter ξ/M^2. The green band corresponds to the EHT measurement range.

11. Bounds Inferred from Solar System Observations

Einstein's theory achieved its first confirmation through Solar System observations, where the Sun was modeled as a static, spherically symmetric source described by the Schwarzschild metric. These classical tests inevitably carry experimental uncertainties, which leave room for small deviations that could, in principle, be attributed to corrections to General Relativity. Taking advantage of this observational tolerance, we now turn to Equation (7) and explore how the parameter ξ modifies the geometry. The objective is to determine the size of this effect and ensure that such modifications remain compatible with present-day measurements.

For particle trajectories restricted to the equatorial plane ($\theta = \pi/2$), the starting point is the Lagrangian formalism. This framework encodes the dynamics of the system and provides the equations of motion needed to study geodesics in the spacetime under consideration:

$$A(r,\xi)\dot{t}^2 - B(r,\xi)^{-1}\dot{r}^2 - r^2\dot{\varphi}^2 = \eta\,. \tag{126}$$

To constrain the motion, the four-velocity model must satisfy a normalization rule, which is implemented by fixing the Lagrangian to $L(x,\dot{x}) = -\eta/2$.The symbol η encodes the nature of the trajectory: setting $\eta = 0$ selects null geodesics, relevant for light-like motion, whereas $\eta = 1$ singles out timelike paths traced by massive particles, whose evolution is described as a function of their proper time λ.

With this normalization in place, the spacetime symmetries lead directly to conserved quantities. Exploiting the time-translation and rotational invariance of the metric tensor, one defines two constants of motion: the energy E and the angular momentum L (as we introduced in the previous sections of the paper), both of which follow from the conjugate momenta associated with the coordinates t and ϕ, namely,

$$E = A(r,\xi)\dot{t} \quad \text{and} \quad L = D(r,\xi)\dot{\varphi}. \tag{127}$$

Starting from the Lagrangian in Equation (126) and using the relations that define the conserved energy and angular momentum given in Equation (127), the resulting combination leads to the following expression:

$$\left[\frac{\mathrm{d}}{\mathrm{d}\varphi}\left(\frac{1}{r}\right)\right]^2 = r^{-4}D^2(r,\xi)\left[\frac{E^2}{A(r,\xi)B(r,\xi)^{-1}L^2} - \frac{1}{B(r,\xi)^{-1}L^2}\left(\eta + \frac{L^2}{r^2\sin^2(\theta)}\right)\right]. \tag{128}$$

By defining the auxiliary quantity $u = \dfrac{L^2}{Mr}$ and taking the derivative of Equation (128) with respect to the azimuthal coordinate φ, one isolates the leading contributions that depend on the parameter ξ, which can then be expressed as follows:

$$\begin{aligned}
&\frac{\mathrm{d}^2u}{\mathrm{d}\varphi^2} = \eta - u + \frac{3M^2u^2}{L^2} \\
&+ \frac{E^2\xi\left(L^2u - M^2u^2\right)}{\left(A^2 - 2M^2u\right)^2} + \frac{2M^3\xi^{3/2}}{L^8(L^2 - 2M^2u)^2}\Big(2L^6E^2u^3 - 2L^6\eta u^3 - 3L^4E^2M^2u^4 + 8L^4\eta M^2u^4 \\
&-3L^4M^2u^5 - 8L^2\eta M^4u^5 + 12L^2M^4u^6 - 12M^6u^7\Big).
\end{aligned} \tag{129}$$

When both ξ and M are treated as perturbatively small, Equation (129) can be expanded and reorganized so that its leading contribution takes the simplified form:

$$u''(\varphi) = \eta - \left(1 - \frac{E^2\xi}{L^2}\right)u + \frac{3M^2\left(L^4 + L^2E^2\xi\right)}{L^6}u^2\,. \tag{130}$$

From the reorganized form of the equation, a few distinctive aspects can be highlighted. First, the parameter ξ couples explicitly with the test particle's energy, a feature often predicted in approaches inspired by quantum gravity [7,8]. Second, there is the fact that some of the ξ-dependent contributions remain completely independent of the central mass M, leading to direct modifications of the Newtonian regime. Such mass-independent corrections are consistent with the predictions of several quantum gravity frameworks, in which Planck-scale effects are expected to deform the classical Galilean and Minkowski limits [221].

11.1. The Precession of Mercury's Orbit

A classic test of any alternative to General Relativity is provided by Mercury's perihelion precession, observed as an angular shift accumulated over a hundred years. In this treatment, it is important to mention that Mercury is set as a massive particle ($\eta = 1$) traveling through the Sun's gravitational field, approximated by a static, spherically symmetric geometry. Setting $\xi = 0$ retrieves the usual general relativistic contribution, where the main post-Newtonian effect originates from the u-linear term in Equation (130).

To streamline the calculation, the mass and deformation parameter are rescaled by defining $m = M/L$ and $\epsilon = \xi E^2/L^2$. Expressed with these reparametrized quantities, the principal deviation from the Newtonian prediction becomes:

$$u''(\varphi) = 1 - u + \epsilon u + 3m^2u^2 \,. \tag{131}$$

Advancing the calculation requires rewriting the solution as a perturbative series in the small quantities M/L and ξ. For this purpose, we expand u in the form $u = u_0 + m^2u_m + \epsilon u_\epsilon$, where each term captures a distinct order of correction. The piece u_0 corresponds to the Newtonian result, including its leading adjustment, and can be explicitly expressed as:

$$u_0 = 1 + e\cos(\varphi) \,. \tag{132}$$

Substituting the perturbative decomposition of u back into Equation (131) and rearranging the resulting terms yields the differential equation in the form

$$m^2\Big(3(e\cos(\varphi)+1)^2 - u_m'' - u_m\Big) + \epsilon\big(1 + e\cos(\varphi) - u_\epsilon'' - u_\epsilon\big) = 0 \,. \tag{133}$$

After neglecting the mixed terms proportional to $m^2\epsilon$ and $m^2\lambda$, the surviving contribution proportional to m^2 corresponds to the standard post-Newtonian correction from General Relativity. This term can be written in the form

$$u_m = 3m^2\left[\left(1 + \frac{e^2}{2}\right) - \frac{e^2}{6}\cos(2\varphi) + e\varphi\sin(\varphi)\right] . \tag{134}$$

The terms that are either constant or purely periodic inside the brackets do not contribute to any long-term displacement of the perihelion. The constant piece simply shifts the reference level without evolving, while the oscillatory component cancels out over a complete revolution because of its symmetric nature. These contributions are therefore discarded. What remains significant is the part that grows linearly with φ, as it accumulates over successive orbits and leads to a measurable precession.

For the perturbation proportional to ϵ in Equation (133), consistency of the expansion demands that it introduce only higher-order corrections. The trigonometric terms generated in this step mostly average to zero when integrated over $0 \le \varphi \le 2\pi$, except for the secular piece $-\frac{1}{2}e\varphi\sin\varphi$, which steadily shifts the orbital configuration. After combining this effect with the Newtonian baseline and the post-Newtonian contribution from General Relativity,

and rewriting everything in terms of the original parameters, the final expression for $u(\varphi)$ is obtained as:

$$u(\varphi) = 1 + e\cos(\varphi) + \frac{3M^2}{L^2}\left(1 + \epsilon\frac{L^2}{6M^2}\right)e\varphi\sin(\varphi)\,. \tag{135}$$

Because the contribution proportional to $\varphi\sin\varphi$ is extremely small, it is omitted from the approximation. After dropping this term, the two surviving pieces can be combined using standard trigonometric relations, which leads to the compact expression

$$u(\varphi) \approx 1 + e\cos\left[\left(1 - \frac{3M^2}{L^2}\left(1 + \epsilon\frac{L^2}{6M^2}\right)\right)\varphi\right] \doteq 1 + e\cos\left[\left(1 - \frac{3\widetilde{M}^2}{L^2}\right)\varphi\right]. \tag{136}$$

This result can be interpreted as if the central mass were replaced by an effective quantity $\widetilde{M}^2 = M^2\left(1 + \frac{\epsilon L^2}{6M^2}\right)$, which modifies the standard general relativistic prediction. Using this redefined mass parameter, the extra term responsible for the perihelion shift is obtained as:

$$\Delta\Phi = 6\pi\frac{\widetilde{M}^2}{L^2} = 6\pi\frac{M^2}{L^2}\left(1 + \epsilon\frac{L^2}{6M^2}\right). \tag{137}$$

From this formulation, a dimensionless measure of the departure from the standard general relativistic result can be written as $\delta_{\text{Perih}} = \dfrac{\epsilon L^2}{6M^2}$. Since Mercury completes roughly one revolution every 88 days, it performs approximately $415 \approx 100 \times 365.25/88$ orbits in a century. Multiplying this number by the per-orbit angular shift gives the net precession accumulated over 100 years. In the framework of General Relativity, the predicted value is $\Delta\Phi_{\text{GR}} = 42.9814''$ per century, which is in excellent agreement with the observed result $\Delta\Phi_{\text{Exp}} = (42.9794 \pm 0.0030)''/\text{century}$ [222,223]. This near-perfect match not only confirms Einstein's theory but also allows one to place stringent limits on the parameter ϵ, and consequently on the corrections induced by ξ.

To express the orbital quantities explicitly, the angular momentum is written as $L^2 = Ma(1 - e^2)$, where a and e denote the semi-major axis and eccentricity of the orbit, respectively. The specific orbital energy is given by $E = -M/(2a)$ [224]. Adopting natural units and Mercury's orbital parameters, one sets $M = M_\odot = 9.138 \times 10^{37}$, $a = 3.583 \times 10^{45}$, $e = 0.2056$, which yields $L = 5.600 \times 10^{41}$, confirming that M^2/L^2 is indeed very small, validating a perturbative expansion. The corresponding energy squared is $E^2 = 1.627 \times 10^{-16}$, implying that any energy-dependent correction is negligible.

Finally, inserting these values into $\epsilon = \xi\dfrac{E^2}{L^2}$ leads to the allowed range for the deformation parameter: $-9.15 \times 10^{18}\,\text{m}^2 \leq \xi \leq 1.83 \times 10^{18}\,\text{m}^2$.

11.2. Deflection of Light

When a photon travels near a gravitating object, its path no longer follows a straight line, producing an apparent shift in the position of the distant source as seen by the observer. This effect, usually referred to as gravitational light deflection, is described mathematically by the null geodesics of the spacetime. In this case, one enforces $\eta = 0$ in Equation (130) to represent massless particles. For convenience, the radial coordinate is inverted through the change in variable $u = 1/r$, which transforms the equation into the form

$$u''(\varphi) = \frac{-L^2 + E^2\xi}{L^2}u + \frac{3M\left(L^2 + \xi E^2\right)}{L^2}u^2\,. \tag{138}$$

Within this framework, the quantity $b = L/E$ is identified as the impact parameter, characterizing how closely the photon approaches the central object, as we have introduced in the previous sections. To examine exclusively the influence of the deformation

parameter ξ, one separates its contributions from those depending on M. Interestingly, the ξ-dependent terms survive even in the limit where the central mass vanishes, indicating that these corrections deform the light path independently of the gravitational potential and therefore alter the Newtonian prediction at the very first order. After redefining the mass contribution for convenience, the dominant terms take the form

$$u''(\varphi) + \left(1 - \frac{\xi}{b^2}\right) u = 3\widetilde{M} u^2 \,. \tag{139}$$

In this formulation, the parameter of mass may be rewritten in an effective form, $\widetilde{M} = M\left(1 + \frac{\xi}{b^2}\right)$, which encodes the deformation effects. By imposing that the left-hand side of the equation vanishes, one recovers the standard Newtonian expression, and the deviation from the classical prediction appears as an additional correction term [223]:

$$u_0 = b^{-1} \sin\left(\left(1 - \frac{\xi}{2b^2}\right)\varphi\right). \tag{140}$$

Choosing the initial condition $\varphi_0 = 0$ corresponds to a straight-line propagation with no bending. Inserting this zeroth-order path into Equation (139) and expanding in the limit of very small angular deflections ($\varphi \ll 1$) leads to the first-order perturbed expression:

$$u(\varphi) = \frac{1}{b}\sin\left(\left(1 - \frac{\xi}{2b^2}\right)\varphi\right) + \frac{\widetilde{M}}{b^2(1 - \xi/b^2)}\left[1 + \cos^2\left(\left(1 - \frac{\xi}{2b^2}\right)\varphi\right)\right]. \tag{141}$$

When the photon escapes to large distances, its trajectory asymptotically satisfies $u \to 0$ (equivalently $r \to \infty$). The entry and exit angles of the trajectory can be obtained by imposing this asymptotic condition and solving for φ. Allowing small fluctuations in both the angular coordinate and the deformation parameters gives the approximate results $\varphi_{\text{in}} = -\frac{2\bar{M}}{b}$, $\varphi_{\text{ex}} = \pi + \frac{2\bar{M}}{b}$, where the effective mass is given by $\bar{M} = M\left(1 + \frac{5\xi}{2b^2}\right)$. The total change in direction of the light ray is obtained from the difference between the incoming and outgoing angles, giving the deflection angle $\delta = -2\varphi_{u\to 0}$

$$\delta = \frac{4\bar{M}}{b} = 4\frac{M}{b}\left(1 + \frac{5\xi}{2b^2}\right). \tag{142}$$

For a photon skimming the solar limb, the impact parameter is effectively the solar radius, $b \simeq R_\odot = 4.305 \times 10^{43}$, with the Sun's mass being regarded as $M = M_\odot = 9.138 \times 10^{37}$. The effect of the deformed parameter ξ appears through the multiplicative factor $1 + \frac{5\xi}{2b^2}$, which is remarkable in that it does not depend explicitly on M but rather on the impact parameter, and hence is tied to the solar radius.

In standard General Relativity, the expected deflection angle is $\delta_{\text{GR}} = \frac{4M}{b} = 1.7516687''$.

Experimentally, the observed value is reported as $\delta_{\text{Exp}} = \frac{1}{2}(1 + \gamma) \times 1.7516687''$, $\gamma = 0.99992 \pm 0.00012$ [225]. To quantify the contribution from ξ, the above multiplicative factor is matched against the empirical ratio $(1 + \gamma)/2$, resulting in the constraint $-1.94 \times 10^{13}\,\text{m}^2 \leq \xi \leq 3.87 \times 10^{12}\,\text{m}^2$.

11.3. Time Delay of Light

The time delay of light (Shapiro effect) [226] describes the extra propagation time undergone by electromagnetic signals as they pass near a massive object before reaching their destination. In the case of planetary radar ranging, this means that signals released from Earth to an inner planet and reflected back take slightly longer to complete the round trip because spacetime is curved by the Sun's gravitational field.

To quantify this delay, one studies null geodesics derived from Equation (128). Imposing the condition $\eta = 0$ for massless particles and using the conserved energy and angular momentum from Equation (127), the trajectory can be reformulated as shown below:

$$\left(\frac{\mathrm{d}r}{\mathrm{d}t}\right)^2 = \frac{A(r,\xi)r^2 - \frac{L^2}{E^2}A(r,\xi)}{B(r,\xi)^{-1}\,r^2}\,. \tag{143}$$

Following the approach of Ref. [227], the constants of motion can be rewritten using the closest approach of the photon to the Sun, identified with the impact parameter b. This turning point is obtained by enforcing $\dot{r} = 0$, which yields the relation $\frac{L^2}{E^2} = \frac{D(r_{\min},\xi)}{A(r_{\min},\xi)}$. With this identification, the travel time of the signal can properly be derived as a function of radial coordinate terms, resulting in the following integral representation:

$$\mathrm{d}t = \pm\frac{1}{A(r,\xi)}\frac{1}{\sqrt{\frac{1}{A(r,\xi)B(r,\xi)^{-1}} - \frac{r_{\min}^2/A(r_{\min},\xi)}{B(r,\xi)^{-1}r^2}}}\,. \tag{144}$$

To highlight the departure from Minkowski spacetime, subleading pieces are discarded and only the leading contributions proportional to M and ξ are retained. Under this perturbative treatment, integrating Equation (144) yields the compact result

$$\begin{aligned} t = {} & \sqrt{r^2 - r_{\min}^2} + M\left(\sqrt{\frac{r-r_{\min}}{r+r_{\min}}} + 2\ln\left(\frac{r+\sqrt{r^2-r_{\min}^2}}{r_{\min}}\right)\right) \\ & + \xi\left[\frac{M}{r_{\min}}\sqrt{\frac{r-r_{\min}}{r+r_{\min}}}\left(\frac{8}{r_{\min}} + \frac{5}{r}\right) + \arctan\left(\frac{\sqrt{r^2-r_{\min}^2}-r}{r_{\min}}\right)\left(\frac{2}{r_{\min}} - \frac{M}{r_{\min}}\right)\right] \\ & - \xi^{3/2}\left[\frac{M}{2r_{\min}r}\sqrt{\frac{r-r_{\min}}{r+r_{\min}}}\left(\frac{1}{r_{\min}} + \frac{1}{r}\right) - \frac{M}{r_{\min}^3}\arctan\left(\frac{\sqrt{r^2-r_{\min}^2}-r}{r_{\min}}\right)\right] \end{aligned} \tag{145}$$

For distances much larger than the point of closest approach ($r \gg r_{\min}$), the expression simplifies significantly. In this asymptotic regime, the main contribution comes from the standard general relativistic piece together with the first-order correction induced by ξ, which together take the form

$$t(r) = r + M + 2M\ln\left(\frac{2r}{r_{\min}}\right) + \xi\frac{8M}{r_{\min}^2} + \xi^{3/2}\frac{M}{3r^3}\,. \tag{146}$$

Define $t(r_E)$ as the one-way propagation time from the emitter's position until reaching the minimum solar distance, and $t(r_R)$ as the corresponding travel time from that point to the receiver. Using Equation (146), with r_E and r_R specifying the respective radial coordinates, these quantities can be evaluated explicitly. The total round-trip duration is then obtained by doubling both segments, giving $T = 2\,t(r_E) + 2\,t(r_R)$. With this construction, the overall signal travel time can be compactly written as:

$$T = 2(r_E + r_R) + 4M\left[1 + \ln\left(\frac{4r_R r_E}{r_{\min}^2}\right) + \xi\frac{8}{r_{\min}^2} + \xi^{3/2}\frac{1}{6}\left(\frac{1}{r_E^3} + \frac{1}{r_R^3}\right)\right] = T_{\mathrm{flat}} + \delta T\,. \tag{147}$$

Thereby, the Shapiro delay represents the excess time taken by the signal compared to what would be measured if spacetime were flat. Without gravity, the round–trip duration would simply be $T_{\mathrm{flat}} = 2(r_E + r_R)$. In the language of the parameterized post-Newtonian framework, the correction produced by the curvature of spacetime is written as:

$$\delta T = 4M\left(1 + \frac{1+\gamma}{2}\ln\left(\frac{4r_R r_E}{r_{\min}^2}\right)\right). \tag{148}$$

Observations from the Cassini mission [228,229] provided one of the tightest experimental tests of relativistic gravity, constraining the PPN parameter to $|\gamma - 1| < 2.3 \times 10^{-5}$. Working in natural units, the mean Earth–Sun distance is taken as one astronomical unit, $r_E = 1\,\mathrm{AU} = 2.457 \times 10^{45}$.

Throughout the observation period, the spacecraft was located at $r_R = 8.46\,\mathrm{AU}$, while the signal's closest approach to the Sun was $r_{\min} = 1.6\,R_\odot$, $R_\odot = 4.305 \times 10^{43}$. Substituting these values into the expression for the Shapiro delay and keeping only the leading term that depends on ξ, one arrives at the constraint $|\xi| \leq 2.04 \times 10^{14}\,\mathrm{m}^2$. We summarize our main results in Table 9.

Table 9. Constraints on ξ from Solar System observables.

Solar System Test	Constraints (m^2)
Mercury precession	$-9.15 \times 10^{18}\,\mathrm{m}^2 \leq \xi \leq 1.83 \times 10^{18}\,\mathrm{m}^2$
Light deflection	$-1.94 \times 10^{13}\,\mathrm{m}^2 \leq \xi \leq 3.87 \times 10^{12}\,\mathrm{m}^2$
Shapiro time delay	$-2.04 \times 10^{14}\,\mathrm{m}^2 \leq \xi \leq 2.04 \times 10^{14}\,\mathrm{m}^2$

For better visualization, we present all constraints obtained based on Solar System and observational data in Table 10. We have converted all constraints to both dimensional (SI) and dimensionless forms for direct comparison. For the Solar System, ξ/M^2 is computed using $M = GM_\odot/c^2 = 1.477$ km, while for black holes, ξ/M^2 is calculated directly in geometric units. Since the masses involved in the constraint calculations differ by 9–10 orders of magnitude ($M_{\mathrm{Solar}} = M_\odot$ vs. $M_{\mathrm{BH}} \sim 10^6$–$10^9 M_\odot$), the most meaningful comparison is in terms of the dimensional parameter ξ (m^2) (assuming that ξ is constant across scales). The table shows that the Solar System exploration provide tighter bounds on the absolute value of ξ (in m^2) using the light deflection method. Our black hole constraints, when expressed in SI units as $\xi \leq 3.36 \times 10^{19}\,\mathrm{m}^2$ (*Sgr A**) and $\xi \leq 8.38 \times 10^{24}\,\mathrm{m}^2$ (*M87**), are indeed much weaker than all the Solar System bounds. It is worth noting that the comparison between the Solar System and black hole constraints depends on whether ξ is assumed to have the same value at all scales. Under this assumption, the Solar System tests provide the tighter bounds. The black hole results should therefore be regarded as complementary probes of the strong-field regime. A possible variation in ξ between Solar System and black hole scales is not considered here and would require a separate theoretical justification.

Table 10. Comprehensive constraints on the deformation parameter ξ from various gravitational aspects. For Solar System tests, ξ_{SI} is in SI units; ξ/M^2 is computed using $M = GM_\odot/c^2 = 1.477$ km. For black holes, ξ/M^2 is calculated directly in geometric units.

System/Test	Mass ($M_\odot$)	ξ_{SI} (m^2)	ξ/M^2 (Dimensionless)
Solar System Tests			
Light deflection	1	$-1.94 \times 10^{13} \leq \xi \leq 3.87 \times 10^{12}$	$-8.90 \times 10^6 \leq \xi/M^2 \leq 1.77 \times 10^6$
Mercury precession	1	$-9.15 \times 10^{18} \leq \xi \leq 1.83 \times 10^{18}$	$-4.20 \times 10^{12} \leq \xi/M^2 \leq 8.39 \times 10^{11}$
Shapiro time delay	1	$-2.04 \times 10^{14} \leq \xi \leq 2.04 \times 10^{14}$	$-9.35 \times 10^7 \leq \xi/M^2 \leq 9.35 \times 10^7$
Black Hole Lensing			
Sgr A*	4.0×10^6	$0 \leq \xi \leq 3.36 \times 10^{19}$	$0 \leq \xi/M^2 \lesssim 0.963$
M87*	6.5×10^9	$0 \leq \xi \leq 8.38 \times 10^{24}$	$0 \leq \xi/M^2 \lesssim 0.091$

12. Conclusions

In this work, we explored the gravitational features of a recently proposed black hole solution within the framework of higher-order curvature–scalar gravity [92]. The resulting spacetime could be interpreted as a "mix geometry": its g_{tt} component resembled the Reissner–Nordström solution, while its g_{rr} component was similar to that of a Loop Quantum Gravity-inspired black hole.

As a first step, we determined the event horizon, which was approximately $r_h \approx 2M - \frac{\xi^{3/2}}{4M^2}$. Solving $1/g_{rr} = 0$ also revealed an additional real and positive root, corresponding to the Cauchy horizon, given by $r_{\rm cau} \approx \sqrt{\xi} + \frac{\xi}{6M} + \frac{\xi^{3/2}}{12M^2} + \frac{35\xi^2}{648M^3}$. We observed opposite behaviors: increasing ξ reduced r_h but enlarged $r_{\rm cau}$.

The analysis then turned to quasinormal modes. We considered perturbations of all spins—scalar, vector, tensor, and spinorial—by solving the corresponding massless field equations (Klein–Gordon, Proca-like, Dirac, etc.). After separating variables, the effective potentials were extracted and the WKB method was employed to compute the complex frequencies. For all perturbations, larger values of ξ led to less damped oscillations. These results were confirmed by numerical simulations in the time domain.

Next, we studied null geodesics, photon spheres, and black hole shadows. Light-like geodesics were solved numerically, showing that larger ξ values produced weaker light deflection. The photon sphere radius was obtained analytically as $r_{\rm photon} = \frac{1}{2}\left(3M + \sqrt{9M^2 - 8\xi}\right)$, in close analogy with the Reissner–Nordström case. The shadow radius was found to be $R = 3\sqrt{3}M - \frac{\sqrt{3}\xi}{2M} - \frac{7\xi^2}{24\sqrt{3}M^3}$, which decreased as ξ grew.

The gravitational lensing analysis was carried out in both weak and strong deflection regimes. In the weak-field case, we applied the Gauss–Bonnet theorem to compute the deflection angle $\tilde{\alpha}(b, \xi)$, which increased with ξ. In the strong deflection limit, however, the deflection angle $a(b, \xi)$ decreased as ξ grew. This behavior was confirmed by analyzing geodesics near the photon sphere. We also estimated the corresponding lensing observables using Event Horizon Telescope data for $SgrA^*$ and $M87^*$.

Furthermore, we constrained the parameter ξ using Solar System tests, obtaining Mercury perihelion precession: $-9.15 \times 10^{18}\,\mathrm{m}^2 \leq \xi \leq 1.83 \times 10^{18}\,\mathrm{m}^2$; light deflection: $-1.94 \times 10^{13}\,\mathrm{m}^2 \leq \xi \leq 3.87 \times 10^{12}\,\mathrm{m}^2$; and Shapiro time delay: $-2.04 \times 10^{14}\,\mathrm{m}^2 \leq \xi \leq 2.04 \times 10^{14}\,\mathrm{m}^2$. Finally, the constraints on the HOCG parameter, obtained using different gravitational methods and observational data, were compared and discussed.

As a natural continuation of this study, it may be interesting to analyze the metric presented here within the framework of ensemble theory, in line with recent developments reported in the literature [230–233]. In parallel, a comprehensive investigation of greybody factors for scalar, vector, tensor, and spinor perturbations, together with their connection to quasinormal modes and particle creation processes for both bosonic and fermionic fields, is already underway. This latter work, developed following the methodology outlined in Refs. [175,234,235], is in its final stage of revision and is expected to be published soon on arXiv.

Author Contributions: Conceptualization, A.A.A.F.; methodology, A.A.A.F., N.H. and I.P.L.; software, A.A.A.F., N.H. and I.P.L.; validation, A.A.A.F. and N.H.; formal analysis, A.A.A.F. and N.H.; investigation, A.A.A.F., N.H. and I.P.L.; writing—original draft preparation, A.A.A.F., N.H. and I.P.L.; writing—review and editing, A.A.A.F., N.H. and I.P.L.; visualization, A.A.A.F.; supervision, I.P.L.; project administration, A.A.A.F. and I.P.L.; funding acquisition, I.P.L. All authors have read and agreed to the published version of the manuscript.

Funding: A. A. Araújo Filho was supported by Conselho Nacional de Desenvolvimento Científico e Tecnológico (CNPq) and Fundação de Apoio à Pesquisa do Estado da Paraíba (FAPESQ), project numbers 150223/2025-0 and 1951/2025. I. P. L. acknowledges partial financial support from the National

Council for Scientific and Technological Development (CNPq), under grant No. 312547/2023-4. In addition, I. P. L. would like to acknowledge the networking support of the COST Actions BridgeQG (CA23130), RQI (CA23115) and FuSe (CA24101), both funded by COST—the European Cooperation in Science and Technology. N. H. was supported by Conselho Nacional de Desenvolvimento Científico e Tecnológico—CNPq, project number 152891/2025-0. N. H. is grateful for the support provided by three COST Actions: CA21106 (COSMIC WISPers in the Dark Universe: Theory, Astrophysics and Experiments), CA21136 (Addressing Observational Tensions in Cosmology with Systematics and Fundamental Physics, also known as CosmoVerse), and CA23130 (Bridging High and Low Energies in Search of Quantum Gravity, or BridgeQG).

Data Availability Statement: No new data were created or analyzed in this study.

Acknowledgments: The authors thank C. F. S. Pereira and M. V. S. Silva for the fruitful discussions on gravitational lensing incorporated into the revised version of the paper.

Conflicts of Interest: The authors declare no conflicts of interest.

References

1. Penrose, R. Gravitational collapse and spacetime singularities. *Phys. Rev. Lett.* **1965**, *14*, 57. [CrossRef]
2. Hawking, S.W.; Ellis, G.F. *The Large Scale Structure of Space-Time*; Cambridge University Press: Cambridge, UK, 2023.
3. Joshi, P.S. *Gravitational Collapse and Spacetime Singularities*; Cambridge University Press: Cambridge, UK, 2007.
4. Abbott, B.P. et al. [LIGO Scientific and Virgo Collaborations] GW170817: Observation of gravitational waves from a binary neutron star inspiral. *Phys. Rev. Lett.* **2017**, *119*, 161101. [CrossRef] [PubMed]
5. Akiyama, K. et al. [Event Horizon Telescope Collaboration] First M87* event horizon telescope results. I. The shadow of the supermassive black hole. *Astrophys. J. Lett.* **2019**, *875*, L1. [CrossRef]
6. Akiyama, K. et al. [Event Horizon Telescope Collaboration] First Sagittarius A* Event Horizon Telescope results. I. The shadow of the supermassive black hole in the center of the Milky Way. *Astrophys. J. Lett.* **2022**, *930*, L12. [CrossRef]
7. Jetzer, P.; Alvarez-Muniz, J.; Alves Batista, R.; Amelino-Camelia, G.; Antonelli, V.; Arzano, M.; Asorey, M.; Atteia, J.; Bahamonde, S.; Bajardi, F.; et al. Quantum gravity phenomenology at the dawn of the multi-messenger era—A review. *Prog. Part. Nucl. Phys.* **2022**, *125*, 103948. [CrossRef]
8. Alves Batista, R.; Amelino-Camelia, G.; Boncioli, D.; Carmona, J.M.; di Matteo, A.; Gubitosi, G.; Lobo, I.; Mavromatos, N.E.; Pfeifer, C.; Rubiera-Garcia, D.; et al. White paper and roadmap for quantum gravity phenomenology in the multi-messenger era. *Class. Quantum Gravity* **2025**, *42*, 032001. [CrossRef]
9. De Felice, A.; Tsujikawa, S. $f(R)$ theories. *Living Rev. Relativ.* **2010**, *13*, 1–161.
10. Sotiriou, T.P.; Faraoni, V. $f(R)$ theories of gravity. *Rev. Mod. Phys.* **2010**, *82*, 451–497. [CrossRef]
11. Nojiri, S.; Odintsov, S.D. Introduction to modified gravity and gravitational alternative for dark energy. *Int. J. Geom. Methods Mod. Phys.* **2007**, *4*, 115–145. [CrossRef]
12. Cai, Y.F.; Capozziello, S.; De Laurentis, M.; Saridakis, E.N. f(T) teleparallel gravity and cosmology. *Rep. Prog. Phys.* **2016**, *79*, 106901. [CrossRef] [PubMed]
13. Nojiri, S.; Odintsov, S.D.; Oikonomou, V.K. Modified Gravity Theories on a Nutshell: Inflation, Bounce and Late-time Evolution. *Phys. Rep.* **2017**, *692*, 1–104. [CrossRef]
14. Nojiri, S.; Odintsov, S.D.; Oikonomou, V.K. k-essence $f(R)$ gravity inflation. *Nucl. Phys. B* **2019**, *941*, 11–27. [CrossRef]
15. Nashed, G.G. Schwarzschild solution in extended teleparallel gravity. *Europhys. Lett.* **2014**, *105*, 10001. [CrossRef]
16. Faraoni, V.; Capozziello, S. *Beyond Einstein Gravity: A Survey of Gravitational Theories for Cosmology and Astrophysics*; Springer: Berlin/Heidelberg, Germany, 2011.
17. Capozziello, S.; De Laurentis, M. Extended theories of gravity. *Phys. Rep.* **2011**, *509*, 167–321. [CrossRef]
18. El Hanafy, W.; Nashed, G.G. Reconstruction of f(T)-gravity in the absence of matter. *Astrophys. Space Sci.* **2016**, *361*, 197. [CrossRef]
19. Nashed, G.G. Vacuum non–singular black hole solutions in tetrad theory of gravitation. *Gen. Relativ. Gravit.* **2002**, *34*, 1047–1058. [CrossRef]
20. Awad, A.; El Hanafy, W.; Nashed, G.; Saridakis, E.N. Phase Portraits of general f (T) Cosmology. *J. Cosmol. Astropart. Phys.* **2018**, *2018*, 52. [CrossRef]
21. Awad, A.; El Hanafy, W.; Nashed, G.; Odintsov, S.; Oikonomou, V. Constant-roll inflation in f(T) teleparallel gravity. *J. Cosmol. Astropart. Phys.* **2018**, *2018*, 26. [CrossRef]
22. Nashed, G.G. Kerr-NUT black hole thermodynamics in f(T) gravity theories. *Eur. Phys. J. Plus* **2015**, *130*, 124. [CrossRef]
23. Zubair, M.; Abbas, G. Analytic models of anisotropic strange stars in f (T) gravity with off-diagonal tetrad. *Astrophys. Space Sci.* **2016**, *361*, 27. [CrossRef]

24. Zubair, M.; Abbas, G.; Noureen, I. Possible formation of compact stars in f(R,T) gravity. *Astrophys. Space Sci.* **2015**, *361*. [CrossRef]
25. Harko, T.; Lobo, F.S.; Nojiri, S.; Odintsov, S.D. f (R, T) gravity. *Phys. Rev. D* **2011**, *84*, 024020. [CrossRef]
26. Saleem, R.; Kramat, F.; Zubair, M. Interior solutions of compact stars in f (T, T) gravity under Karmarkar condition. *Phys. Dark Universe* **2020**, *30*, 100592. [CrossRef]
27. Cognola, G.; Elizalde, E.; Nojiri, S.; Odintsov, S.D.; Zerbini, S. Dark energy in modified Gauss-Bonnet gravity: Late-time acceleration and the hierarchy problem. *Phys. Rev. D* **2006**, *73*, 084007. [CrossRef]
28. Róis, G.I.; Junior, J.T.S.; Lobo, F.S.; Rodrigues, M.E.; Harko, T. Charged black hole solutions in f(R,T) gravity coupled to nonlinear electrodynamics. *Phys. Rev. D* **2025**, *111*, 124044. [CrossRef]
29. Araújo Filho, A.A.; Heidari, N.; Lobo, I.P.; Bezerra, V. Gravitational signatures of a nonlinear electrodynamics in f (R, T) gravity. *J. Cosmol. Astropart. Phys.* **2025**, *2025*, 15. [CrossRef]
30. De Martino, I.; De Laurentis, M.; Capozziello, S. Constraining $f(R)$ gravity by the large-scale structure. *Universe* **2015**, *1*, 123–157. [CrossRef]
31. Starobinskii, A. Spectrum of relict gravitational radiation and the early state of the universe. *JETP Lett.* **1979**, *30*, 682–685.
32. Astashenok, A.V. Neutron and quark stars in $f(R)$ gravity. In *Proceedings of the International Journal of Modern Physics: Conference Series*; World Scientific: Singapore, 2016; Volume 41, p. 1660130.
33. Astashenok, A.V.; Capozziello, S.; Odintsov, S.D. Maximal neutron star mass and the resolution of the hyperon puzzle in modified gravity. *Phys. Rev. D* **2014**, *89*, 103509. [CrossRef]
34. Astashenok, A.V.; Capozziello, S.; Odintsov, S.D. Further stable neutron star models from $f(R)$ gravity. *J. Cosmol. Astropart. Phys.* **2013**, *2013*, 040. [CrossRef]
35. Astashenok, A.V.; Odintsov, S.D.; De la Cruz-Dombriz, A. The realistic models of relativistic stars in $f(R) = R + \alpha R^2$ gravity. *Class. Quantum Gravity* **2017**, *34*, 205008. [CrossRef]
36. Astashenok, A.V.; Capozziello, S.; Odintsov, S.D. Nonperturbative models of quark stars in $f(R)$ gravity. *Phys. Lett. B* **2015**, *742*, 160–166. [CrossRef]
37. Nashed, G.G.; El Hanafy, W.; Odintsov, S.D.; Oikonomou, V.K. Thermodynamical correspondence of $f(R)$ gravity in the Jordan and Einstein frames. *Int. J. Mod. Phys. D* **2020**, *29*, 2050090. [CrossRef]
38. Nashed, G.G.; Capozziello, S. Anisotropic compact stars in $f(R)$ gravity. *Eur. Phys. J. C* **2021**, *81*, 481. [CrossRef]
39. Stabile, A.; Capozziello, S. Conformal transformations and weak field limit of scalar-tensor gravity. *Phys. Rev. D* **2013**, *88*, 124011. [CrossRef]
40. Capozziello, S.; Mantica, C.A.; Molinari, L.G. Cosmological perfect-fluids in $f(R)$ gravity. *Int. J. Geom. Methods Mod. Phys.* **2019**, *16*, 1950008. [CrossRef]
41. Odintsov, S.; Oikonomou, V. Effects of spatial curvature on the $f(R)$ gravity phase space: No inflationary attractor? *Class. Quantum Gravity* **2019**, *36*, 065008. [CrossRef]
42. Odintsov, S.; Oikonomou, V. $f(R)$ gravity inflation with string-corrected axion dark matter. *Phys. Rev. D* **2019**, *99*, 064049. [CrossRef]
43. Shah, P.; Samanta, G.C. Stability analysis for cosmological models in $f(R)$ gravity using dynamical system analysis. *Eur. Phys. J. C* **2019**, *79*, 414. [CrossRef]
44. Miranda, T.; Escamilla-Rivera, C.; Piattella, O.F.; Fabris, J.C. Generic slow-roll and non-gaussianity parameters in $f(R)$ theories. *J. Cosmol. Astropart. Phys.* **2019**, *5*, 28. [CrossRef]
45. Nascimento, J.R.; Olmo, G.J.; Porfirio, P.J.; Petrov, A.Y.; Soares, A.R. Global Monopole in Palatini $f(R)$ gravity. *Phys. Rev. D* **2019**, *99*, 064053. [CrossRef]
46. Elizalde, E.; Odintsov, S.D.; Paul, T.; Sáez-Chillón Gómez, D. Inflationary universe in $F(R)$ gravity with antisymmetric tensor fields and their suppression during its evolution. *Phys. Rev. D* **2019**, *99*, 063506. [CrossRef]
47. Elizalde, E.; Odintsov, S.D.; Oikonomou, V.K.; Paul, T. Logarithmic-corrected R^2 Gravity Inflation in the Presence of Kalb-Ramond Fields. *J. Cosmol. Astropart. Phys.* **2019**, *2*, 17. [CrossRef]
48. Chen, L. Dynamical analysis of loop quantum R^2 cosmology. *Phys. Rev. D* **2019**, *99*, 064025. [CrossRef]
49. Sbisà, F.; Piattella, O.F.; Jorás, S.E. Pressure effects in the weak-field limit of $f(R) = R + \alpha R^2$ gravity. *Phys. Rev. D* **2019**, *99*, 104046. [CrossRef]
50. Samanta, G.C.; Godani, N. Validation of energy conditions in wormhole geometry within viable $f(R)$ gravity. *Eur. Phys. J. C* **2019**, *79*, 623. [CrossRef]
51. Bombacigno, F.; Montani, G. Big bounce cosmology for Palatini R^2 gravity with a Nieh–Yan term. *Eur. Phys. J. C* **2019**, *79*, 405. [CrossRef]
52. Astashenok, A.V.; Mosani, K.; Odintsov, S.D.; Samanta, G.C. Gravitational collapse in General Relativity and in R 2-gravity: A comparative study. *Int. J. Geom. Methods Mod. Phys.* **2019**, *16*, 1950035. [CrossRef]
53. Nashed, G. Charged solution with equal metric ansatz in Gauss–Bonnet theory coupled to scalar field. *Phys. Dark Universe* **2023**, *41*, 101260. [CrossRef]

54. Nojiri, S.; Odintsov, S.D.; Oikonomou, V.K.; Popov, A.A. Ghost-free $F(R, \mathcal{G})$ gravity. *Nucl. Phys. B* **2021**, *973*, 115617. [CrossRef]
55. de Haro, J.; Nojiri, S.; Odintsov, S.D.; Oikonomou, V.K.; Pan, S. Finite-time cosmological singularities and the possible fate of the Universe. *Phys. Rep.* **2023**, *1034*, 1–114. [CrossRef]
56. Capozziello, S.; Nashed, G.G.L. Charged spherically symmetric black holes in scalar-tensor Gauss–Bonnet gravity. *Class. Quantum Gravity* **2023**, *40*, 205023. [CrossRef]
57. Millano, A.D.; Leon, G.; Paliathanasis, A. Global dynamics in Einstein-Gauss-Bonnet scalar field cosmology with matter. *Phys. Rev. D* **2023**, *108*, 023519. [CrossRef]
58. Nojiri, S.; Odintsov, S.D. F (Q) F(Q) Gravity with Gauss–Bonnet Corrections: From Early-Time Inflation to Late-Time Acceleration. *Fortsch. Phys.* **2024**, *72*, 2400113. [CrossRef]
59. Ilyas, M.; Bamba, K. Traversable wormholes with static spherical symmetry and their stability in higher-curvature gravity. *J. Cosmol. Astropart. Phys.* **2023**, *2023*, 038. [CrossRef]
60. Paul, S.; Gangopadhyay, S.; Saha, A. Gauss–Bonnet AdS planar and spherical black hole thermodynamics and holography. *Class. Quantum Gravity* **2024**, *41*, 235010. [CrossRef]
61. Nashed, G.G.L. Spherically symmetric charged black holes in $f(R)$ gravitational theories. *Eur. Phys. J. Plus* **2018**, *133*, 18. [CrossRef]
62. Nashed, G.G.L. Higher Dimensional Charged Black Hole Solutions in $f(R)$ Gravitational Theories. *Adv. High Energy Phys.* **2018**, *2018*, 7323574. [CrossRef]
63. Multamäki, T.; Vilja, I. Spherically symmetric solutions of modified field equations in $f(R)$ theories of gravity. *Phys. Rev. D* **2006**, *74*, 064022. [CrossRef]
64. Nashed, G. Rotating charged black hole spacetimes in quadratic $f(R)$ gravitational theories. *Int. J. Mod. Phys. D* **2018**, *27*, 1850074. [CrossRef]
65. Basilakos, S.; Capozziello, S.; De Laurentis, M.; Paliathanasis, A.; Tsamparlis, M. Noether symmetries and analytical solutions in f(T) cosmology: A complete study. *Phys. Rev. D* **2013**, *88*, 103526. [CrossRef]
66. Capozziello, S.; Francaviglia, M. Extended theories of gravity and their cosmological and astrophysical applications. *Gen. Relativ. Gravit.* **2008**, *40*, 357–420.
67. Nashed, G.G.; Capozziello, S. Charged spherically symmetric black holes in $f(R)$ gravity and their stability analysis. *Phys. Rev. D* **2019**, *99*, 104018. [CrossRef]
68. de la Cruz-Dombriz, A.; Dobado, A.; Maroto, A.L. Black holes in $f(R)$ theories. *Phys. Rev. D* **2009**, *80*, 124011.
69. Sultana, J.; Kazanas, D. A no-hair theorem for spherically symmetric black holes in R^2 gravity. *Gen. Relativ. Gravit.* **2018**, *50*, 137. [CrossRef]
70. Cañate, P. A no-hair theorem for black holes in $f(R)$ gravity. *Class. Quantum Gravity* **2017**, *35*, 025018. [CrossRef]
71. Yu, S.; Gao, C.J.; Liu, M.J. On static and spherically symmetric solutions of Starobinsky model. *Res. Astron. Astrophys.* **2018**, *18*, 157. [CrossRef]
72. Kehagias, A.; Kounnas, C.; Lüst, D.; Riotto, A. Black hole solutions in R^2 gravity. *J. High Energy Phys.* **2015**, *2015*, 1–20. [CrossRef]
73. Nelson, W. Static solutions for fourth order gravity. *Phys. Rev. D* **2010**, *82*, 104026. [CrossRef]
74. Cañate, P.; Jaime, L.G.; Salgado, M. Spherically symmetric black holes in $f(R)$ gravity: Is geometric scalar hair supported? *Class. Quantum Gravity* **2016**, *33*, 155005. [CrossRef]
75. Resco, M.A.; de la Cruz-Dombriz, Á.; Estrada, F.J.L.; Castrillo, V.Z. On neutron stars in $f(R)$ theories: Small radii, large masses and large energy emitted in a merger. *Phys. Dark Universe* **2016**, *13*, 147–161. [CrossRef]
76. Staykov, K.V.; Popchev, D.; Doneva, D.D.; Yazadjiev, S.S. Static and slowly rotating neutron stars in scalar–tensor theory with self-interacting massive scalar field. *Eur. Phys. J. C* **2018**, *78*, 586. [CrossRef] [PubMed]
77. Doneva, D.D.; Yazadjiev, S.S. Rapidly rotating neutron stars with a massive scalar field—Structure and universal relations. *J. Cosmol. Astropart. Phys.* **2016**, *2016*, 19. [CrossRef]
78. Arapoğlu, S.; Deliduman, C.; Ekşi, K.Y. Constraints on perturbative $f(R)$ gravity via neutron stars. *J. Cosmol. Astropart. Phys.* **2011**, *2011*, 20. [CrossRef]
79. Feng, W.X.; Geng, C.Q.; Kao, W.F.; Luo, L.W. Equation-of-state of neutron stars with junction conditions in the Starobinsky model. *Int. J. Mod. Phys. D* **2018**, *27*, 1750186.
80. Ganguly, A.; Gannouji, R.; Goswami, R.; Ray, S. Neutron stars in the Starobinsky model. *Phys. Rev. D* **2014**, *89*, 064019. [CrossRef]
81. Yazadjiev, S.S.; Doneva, D.D.; Popchev, D. Slowly rotating neutron stars in scalar-tensor theories with a massive scalar field. *Phys. Rev. D* **2016**, *93*, 084038. [CrossRef]
82. Yazadjiev, S.S.; Doneva, D.D.; Kokkotas, K.D. Rapidly rotating neutron stars in R-squared gravity. *Phys. Rev. D* **2015**, *91*, 084018. [CrossRef]
83. Yazadjiev, S.S.; Doneva, D.D.; Kokkotas, K.D.; Staykov, K.V. Non-perturbative and self-consistent models of neutron stars in R-squared gravity. *J. Cosmol. Astropart. Phys.* **2014**, *2014*, 003. [CrossRef]

84. Orellana, M.; García, F.; Teppa Pannia, F.A.; Romero, G.E. Structure of neutron stars in-squared gravity. *Gen. Relativ. Gravit.* **2013**, *45*, 771–783. [CrossRef]
85. Capozziello, S.; De Laurentis, M.; Farinelli, R.; Odintsov, S.D. Mass-radius relation for neutron stars in $f(R)$ gravity. *Phys. Rev. D* **2016**, *93*, 023501. [CrossRef]
86. Cooney, A.; DeDeo, S.; Psaltis, D. Neutron stars in $f(R)$ gravity with perturbative constraints. *Phys. Rev. D-Part. Fields Gravit. Cosmol.* **2010**, *82*, 064033. [CrossRef]
87. O'Hanlon, J. Intermediate-range gravity: A generally covariant model. *Phys. Rev. Lett.* **1972**, *29*, 137. [CrossRef]
88. Chiba, T. $1/R$ gravity and scalar-tensor gravity. *Phys. Lett. B* **2003**, *575*, 1–3. [CrossRef]
89. Chakraborty, S.; SenGupta, S. Gravity stabilizes itself. *Eur. Phys. J. C* **2017**, *77*, 166. [CrossRef]
90. Brans, C.; Dicke, R.H. Mach's principle and a relativistic theory of gravitation. *Phys. Rev.* **1961**, *124*, 925. [CrossRef]
91. Chakraborty, S.; SenGupta, S. Solving higher curvature gravity theories. *Eur. Phys. J. C* **2016**, *76*, 552. [CrossRef]
92. Nashed, G.G.L.; Zafar, U.; Bamba, K. An innovative black hole solution and thermodynamic properties in higher-order curvature gravity with a scalar field. *Phys. Dark Universe* **2025**, *50*, 102061. [CrossRef]
93. Kanti, P.; Mavromatos, N.E.; Rizos, J.; Tamvakis, K.; Winstanley, E. Dilatonic black holes in higher curvature string gravity. *Phys. Rev. D* **1996**, *54*, 5049–5058. [CrossRef] [PubMed]
94. Nojiri, S.; Odintsov, S.D. Modified Gauss-Bonnet theory as gravitational alternative for dark energy. *Phys. Lett. B* **2005**, *631*, 1–6. [CrossRef]
95. Abbott, B.P. et al. [LIGO Scientific and Virgo Collaborations] Observation of gravitational waves from a binary black hole merger. *Phys. Rev. Lett.* **2016**, *116*, 061102. [CrossRef] [PubMed]
96. Contigiani, O. Lensing efficiency for gravitational wave mergers. *Mon. Not. R. Astron. Soc.* **2020**, *492*, 3359–3363. [CrossRef]
97. Mukherjee, S.; Wandelt, B.D.; Silk, J. Probing the theory of gravity with gravitational lensing of gravitational waves and galaxy surveys. *Mon. Not. R. Astron. Soc.* **2020**, *494*, 1956–1970. [CrossRef]
98. Darwin, C.G. The gravity field of a particle. *Proc. R. Soc. Lond. Ser. A Math. Phys. Sci.* **1959**, *249*, 180–194. [CrossRef]
99. Atkinson, R.d. On light tracks near a very massive star. *Astron. J.* **1965**, *70*, 517. [CrossRef] [PubMed]
100. Mohan, G.; Karmakar, R.; Borah, R.J.; Goswami, U.D. Strong Lensing Effect and Quasinormal Modes of Oscillations of Black Holes in $f(R,T)$ Gravity Theory. *arXiv* **2025**, arXiv:2503.08402.
101. Cunningham, C.T.; Bardeen, J.M. The Optical Appearance of a Star Orbiting an Extreme Kerr Black Hole. *Astrophys. J.* **1973**, *183*, 237–264. [CrossRef] [PubMed]
102. Falcke, H.; Melia, F.; Agol, E. Viewing the shadow of the black hole at the GalacticCenter. *Astrophys. J.* **1999**, *528*, L13.
103. Khodadi, M.; Vagnozzi, S.; Firouzjaee, J.T. Event Horizon Telescope observations exclude compact objects in baseline mimetic gravity. *Sci. Rep.* **2024**, *14*, 26932. [CrossRef] [PubMed]
104. Allahyari, A.; Khodadi, M.; Vagnozzi, S.; Mota, D.F. Magnetically charged black holes from non-linear electrodynamics and the Event Horizon Telescope. *J. Cosmol. Astropart. Phys.* **2020**, *2*, 3. [CrossRef]
105. Nojiri, S.; Odintsov, S.D. Improving mimetic gravity with non-trivial scalar potential: Cosmology, black holes, shadow and photon sphere. *Phys. Dark Universe* **2024**, *46*, 101669. [CrossRef]
106. Afrin, M.; Kumar, R.; Ghosh, S.G. Parameter estimation of hairy Kerr black holes from its shadow and constraints from M87*. *Mon. Not. R. Astron. Soc.* **2021**, *504*, 5927–5940. [CrossRef]
107. Khodadi, M.; Lambiase, G.; Mota, D.F. No-hair theorem in the wake of Event Horizon Telescope. *J. Cosmol. Astropart. Phys.* **2021**, *9*, 28. [CrossRef]
108. Afrin, M.; Ghosh, S.G. Testing Horndeski gravity from EHT observational results for rotating black holes. *Astrophys. J.* **2022**, *932*, 51. [CrossRef]
109. Khodadi, M.; Lambiase, G. Probing Lorentz symmetry violation using the first image of Sagittarius A*: Constraints on standard-model extension coefficients. *Phys. Rev. D* **2022**, *106*, 104050. [CrossRef]
110. Kumar, R.; Ghosh, S.G.; Wang, A. Gravitational deflection of light and shadow cast by rotating Kalb-Ramond black holes. *Phys. Rev. D* **2020**, *101*, 104001. [CrossRef]
111. Afrin, M.; Vagnozzi, S.; Ghosh, S.G. Tests of loop quantum gravity from the event horizon telescope results of Sgr A*. *Astrophys. J.* **2023**, *944*, 149. [CrossRef]
112. Afrin, M.; Ghosh, S.G. EHT observables as a tool to estimate parameters of supermassive black holes. *Mon. Not. R. Astron. Soc.* **2023**, *524*, 3683–3691. [CrossRef]
113. Fu, Q.M.; Zhang, X. Gravitational lensing by a black hole in effective loop quantum gravity. *Phys. Rev. D* **2022**, *105*, 064020. [CrossRef]
114. Ghosh, S.G.; Afrin, M. An upper limit on the charge of the black hole Sgr A* from EHT observations. *Astrophys. J.* **2023**, *944*, 174. [CrossRef]
115. Vagnozzi, S.; Visinelli, L. Hunting for extra dimensions in the shadow of M87*. *Phys. Rev. D* **2019**, *100*, 024020. [CrossRef]
116. Liu, W.; Wu, D.; Wang, J. Shadow of slowly rotating Kalb-Ramond black holes. *J. Cosmol. Astropart. Phys.* **2025**, *5*, 17. [CrossRef]

117. Nojiri, S.; Odintsov, S.D. Black holes and their shadows in $F(R)$ gravity. *Phys. Dark Universe* **2025**, *47*, 101785. [CrossRef]
118. Nojiri, S.; Odintsov, S.D. Black holes, photon sphere, and cosmology in ghost-free $f(G)$ gravity. *Phys. Dark Universe* **2024**, *46*, 101702. [CrossRef]
119. Bambi, C.; Freese, K.; Vagnozzi, S.; Visinelli, L. Testing the rotational nature of the supermassive object M87* from the circularity and size of its first image. *Phys. Rev. D* **2019**, *100*, 044057. [CrossRef]
120. Afrin, M.; Ghosh, S.G.; Wang, A. Testing EGB gravity coupled to bumblebee field and black hole parameter estimation with EHT observations. *Phys. Dark Universe* **2024**, *46*, 101642. [CrossRef]
121. Virbhadra, K.S.; Ellis, G.F. Schwarzschild black hole lensing. *Phys. Rev. D* **2000**, *62*, 084003. [CrossRef]
122. Perlick, V. Theoretical gravitational lensing–beyond the weak-field small-angle approximation. In *Proceedings of the Eleventh Marcel Grossmann Meeting: On Recent Developments in Theoretical and Experimental General Relativity, Gravitation and Relativistic Field Theories (In 3 Volumes)*; World Scientific: Singapore, 2008; pp. 680–699.
123. Bozza, V.; Capozziello, S.; Iovane, G.; Scarpetta, G. Strong field limit of black hole gravitational lensing. *Gen. Relativ. Gravit.* **2001**, *33*, 1535–1548. [CrossRef]
124. Bozza, V. Gravitational lensing in the strong field limit. *Phys. Rev. D* **2002**, *66*, 103001. [CrossRef]
125. Frittelli, S.; Kling, T.P.; Newman, E.T. Spacetime perspective of Schwarzschild lensing. *Phys. Rev. D* **2000**, *61*, 064021. [CrossRef]
126. Metcalf, R.B.; Meneghetti, M.; Avestruz, C.; Bellagamba, F.; Bom, C.R.; Bertin, E.; Cabanac, R.; Courbin, F.; Davies, A.; Decencière, E.; et al. The strong gravitational lens finding challenge. *Astron. Astrophys.* **2019**, *625*, A119. [CrossRef]
127. Grespan, M.; Biesiada, M. Strong gravitational lensing of gravitational waves: A review. *Universe* **2023**, *9*, 200. [CrossRef]
128. Kuang, X.M.; Övgün, A. Strong gravitational lensing and shadow constraint from M87* of slowly rotating Kerr-like black hole. *Ann. Phys.* **2022**, *447*, 169147. [CrossRef]
129. Pantig, R.C.; Övgün, A. Testing dynamical torsion effects on the charged black hole's shadow, deflection angle and greybody with M87* and Sgr A* from EHT. *Ann. Phys.* **2023**, *448*, 169197. [CrossRef]
130. Övgün, A. Light deflection by Damour-Solodukhin wormholes and Gauss-Bonnet theorem. *Phys. Rev. D* **2018**, *98*, 044033. [CrossRef]
131. Chakraborty, S.; SenGupta, S. Strong gravitational lensing—A probe for extra dimensions and Kalb-Ramond field. *J. Cosmol. Astropart. Phys.* **2017**, *2017*, 045. [CrossRef]
132. Araújo Filho, A.A. Antisymmetric tensor influence on charged black hole lensing phenomena and time delay. *J. High Energy Astrophys.* **2025**, *47*, 100401. [CrossRef]
133. Shaikh, R.; Kar, S. Gravitational lensing by scalar-tensor wormholes and the energy conditions. *Phys. Rev. D* **2017**, *96*, 044037. [CrossRef]
134. Araújo Filho, A.A.; Nascimento, J.R.; Petrov, A.Y.; Porfírio, P.J. Gravitational lensing by a Lorentz-violating black hole. *arXiv* **2024**, arXiv:2404.04176.
135. Heidari, N.; Hassanabadi, H.; Araújo Filho, A.A.; Kriz, J.; Zare, S.; Porfírio, P. Gravitational signatures of a non–commutative stable black hole. *Phys. Dark Universe* **2023**, *43*, 101382. [CrossRef]
136. Övgün, A.; Jusufi, K.; Sakallı, İ. Exact traversable wormhole solution in bumblebee gravity. *Phys. Rev. D* **2019**, *99*, 024042. [CrossRef]
137. Tsukamoto, N.; Harada, T.; Yajima, K. Can we distinguish between black holes and wormholes by their Einstein-ring systems? *Phys. Rev. D* **2012**, *86*, 104062. [CrossRef]
138. Shaikh, R.; Banerjee, P.; Paul, S.; Sarkar, T. Strong gravitational lensing by wormholes. *J. Cosmol. Astropart. Phys.* **2019**, *2019*, 28. [CrossRef]
139. Gibbons, G.W.; Vyska, M. The application of Weierstrass elliptic functions to Schwarzschild null geodesics. *Class. Quantum Gravity* **2012**, *29*, 065016. [CrossRef]
140. Tsukamoto, N. Retrolensing by a wormhole at deflection angles π and 3 π. *Phys. Rev. D* **2017**, *95*, 084021. [CrossRef]
141. Lobo, I.P.; Richarte, M.G.; Morais Graça, J.P.; Moradpour, H. Thin-shell wormholes in Rastall gravity. *Eur. Phys. J. Plus* **2020**, *135*, 550. [CrossRef]
142. Tsukamoto, N. Strong deflection limit analysis and gravitational lensing of an Ellis wormhole. *Phys. Rev. D* **2016**, *94*, 124001. [CrossRef]
143. Virbhadra, K. Conservation of distortion of gravitationally lensed images. *Phys. Rev. D* **2024**, *109*, 124004. [CrossRef]
144. Konoplya, R.A.; Zhidenko, A. Decay of a charged scalar and Dirac fields in the Kerr-Newman-de Sitter background. *Phys. Rev. D* **2007**, *76*, 084018. Erratum in *Phys. Rev. D* **2014**, *90*, 029901. [CrossRef]
145. Konoplya, R.A.; Zhidenko, A. Massive charged scalar field in the Kerr-Newman background I: Quasinormal modes, late-time tails and stability. *Phys. Rev. D* **2013**, *88*, 024054. [CrossRef]
146. Karmakar, R.; Goswami, U.D. Quasinormal modes, thermodynamics and shadow of black holes in Hu–Sawicki $f(R)$ gravity theory. *Eur. Phys. J. C* **2024**, *84*, 969. [CrossRef]

147. Konoplya, R.; Zhidenko, A.; Zinhailo, A. Higher order WKB formula for quasinormal modes and grey-body factors: Recipes for quick and accurate calculations. *Class. Quantum Gravity* **2019**, *36*, 155002. [CrossRef]
148. Karmakar, R.; Gogoi, D.J.; Goswami, U.D. Quasinormal modes and thermodynamic properties of GUP-corrected Schwarzschild black hole surrounded by quintessence. *Int. J. Mod. Phys. A* **2022**, *37*, 2250180. [CrossRef]
149. Konoplya, R.A.; Zhidenko, A. Quasinormal modes of black holes: From astrophysics to string theory. *Rev. Mod. Phys.* **2011**, *83*, 793–836. [CrossRef]
150. Kokkotas, K.D.; Konoplya, R.A.; Zhidenko, A. Quasinormal modes, scattering and Hawking radiation of Kerr-Newman black holes in a magnetic field. *Phys. Rev. D* **2011**, *83*, 024031. [CrossRef]
151. Jusufi, K. Connection Between the Shadow Radius and Quasinormal Modes in Rotating Spacetimes. *Phys. Rev. D* **2020**, *101*, 124063. [CrossRef]
152. Konoplya, R.; Zhidenko, A. Correspondence between grey-body factors and quasinormal frequencies for rotating black holes. *Phys. Lett. B* **2025**, *861*, 139288. [CrossRef]
153. Konoplya, R.A.; Zhidenko, A. Correspondence between grey-body factors and quasinormal modes. *J. Cosmol. Astropart. Phys.* **2024**, *9*, 68. [CrossRef]
154. Franchini, N.; Völkel, S.H. Testing general relativity with black hole quasi-normal modes. In *Recent Progress on Gravity Tests: Challenges and Future Perspectives*; Springer: Berlin/Heidelberg, Germany, 2024; pp. 361–416.
155. Nojiri, S.; Nashed, G.G.L. Hayward black hole in scalar-Einstein-Gauss-Bonnet gravity in four dimensions. *Phys. Rev. D* **2023**, *108*, 024014. [CrossRef]
156. Nashed, G.G.L.; Nojiri, S. Multihorizons black hole solutions, photon sphere, and perihelion shift in weak ghost-free Gauss-Bonnet theory of gravity. *Phys. Rev. D* **2022**, *106*, 044024. [CrossRef]
157. Lewandowski, J.; Ma, Y.; Yang, J.; Zhang, C. Quantum oppenheimer-snyder and swiss cheese models. *Phys. Rev. Lett.* **2023**, *130*, 101501. [CrossRef] [PubMed]
158. Nozari, K.; Saghafi, S.; Hajebrahimi, M.; Jusufi, K. Circular orbits and accretion disk around a deformed-Schwarzschild black hole in loop quantum gravity. *Phys. Dark Universe* **2025**, *49*, 102027. [CrossRef]
159. Iyer, S.; Will, C.M. Black-hole normal modes: A WKB approach. I. Foundations and application of a higher-order WKB analysis of potential-barrier scattering. *Phys. Rev. D* **1987**, *35*, 3621. [CrossRef] [PubMed]
160. Iyer, S. Black-hole normal modes: A WKB approach. II. Schwarzschild black holes. *Phys. Rev. D* **1987**, *35*, 3632. [CrossRef] [PubMed]
161. Konoplya, R. Quasinormal behavior of the D-dimensional Schwarzschild black hole and the higher order WKB approach. *Phys. Rev. D* **2003**, *68*, 024018. [CrossRef]
162. Chandrasekhar, S. *The Mathematical Theory of Black Holes*; Oxford University Press: Oxford, UK, 1998; Volume 69.
163. Bouhmadi-López, M.; Brahma, S.; Chen, C.Y.; Chen, P.; Yeom, D.h. A consistent model of non-singular Schwarzschild black hole in loop quantum gravity and its quasinormal modes. *J. Cosmol. Astropart. Phys.* **2020**, *7*, 66. [CrossRef]
164. Gogoi, D.J.; Övgün, A.; Koussour, M. Quasinormal modes of black holes in f(Q) gravity. *Eur. Phys. J. C* **2023**, *83*, 700. [CrossRef]
165. Baruah, A.; Sekhmani, Y.; Maurya, S.K.; Deshamukhya, A.; Jasim, M.K. Quasinormal modes, greybody factors, and Hawking radiation sparsity of black holes influenced by a global monopole charge in Kalb-Ramond gravity. *J. Cosmol. Astropart. Phys.* **2025**, *8*, 23. [CrossRef]
166. Durand, L.; Fishbane, P.M.; Simmons, L., Jr. Expansion formulas and addition theorems for Gegenbauer functions. *J. Math. Phys.* **1976**, *17*, 1933–1948. [CrossRef]
167. Amourah, A.; Alamoush, A.; Al-Kaseasbeh, M. Gegenbauer polynomials and bi-univalent functions. *Palest. J. Math.* **2021**, *10*, 625–632.
168. Lohöfer, G. Inequalities for Legendre functions and Gegenbauer functions. *J. Approx. Theory* **1991**, *64*, 226–234. [CrossRef]
169. Cohl, H.S. On a generalization of the generating function for Gegenbauer polynomials. *Integral Transform. Spec. Funct.* **2013**, *24*, 807–816. [CrossRef]
170. Liu, W.; Wang, L.L. Asymptotics of the generalized Gegenbauer functions of fractional degree. *J. Approx. Theory* **2020**, *253*, 105378. [CrossRef]
171. Ashtekar, A.; Olmedo, J.; Singh, P. Quantum extension of the Kruskal spacetime. *Phys. Rev. D* **2018**, *98*, 126003. [CrossRef]
172. Ashtekar, A.; Olmedo, J.; Singh, P. Quantum transfiguration of Kruskal black holes. *Phys. Rev. Lett.* **2018**, *121*, 241301. [CrossRef] [PubMed]
173. Araújo Filho, A.A. Analysis of a nonlinear electromagnetic generalization of the Reissner–Nordström black hole. *Eur. Phys. J. C* **2025**, *85*, 454. [CrossRef]
174. Chen, C.Y.; Chen, P. Gravitational perturbations of nonsingular black holes in conformal gravity. *Phys. Rev. D* **2019**, *99*, 104003. [CrossRef]
175. Araújo Filho, A.A. How does non-metricity affect particle creation and evaporation in bumblebee gravity? *J. Cosmol. Astropart. Phys.* **2025**, *2025*, 026. [CrossRef]

176. Newman, E.; Penrose, R. An approach to gravitational radiation by a method of spin coefficients. *J. Math. Phys.* **1962**, *3*, 566–578. [CrossRef]
177. Chandrasekhar, S. The mathematical theory of black holes. In Proceedings of the General Relativity and Gravitation: Invited Papers and Discussion Reports of the 10th International Conference on General Relativity and Gravitation, Padua, Italy, 3–8 July 1983; Springer: Berlin/Heidelberg, Germany, 1984; pp. 5–26.
178. Albuquerque, S.; Lobo, I.P.; Bezerra, V.B. Massless Dirac perturbations in a consistent model of loop quantum gravity black hole: Quasinormal modes and particle emission rates. *Class. Quantum Gravity* **2023**, *40*, 174001. [CrossRef]
179. Al-Badawi, A.; Jha, S.K. Massless Dirac perturbations of black holes in f (Q) gravity: Quasinormal modes and a weak deflection angle. *Commun. Theor. Phys.* **2024**, *76*, 095403. [CrossRef]
180. Arbey, A.; Auffinger, J.; Geiller, M.; Livine, E.R.; Sartini, F. Hawking radiation by spherically-symmetric static black holes for all spins: Teukolsky equations and potentials. *Phys. Rev. D* **2021**, *103*, 104010. [CrossRef]
181. Devi, S.; Roy, R.; Chakrabarti, S. Quasinormal modes and greybody factors of the novel four dimensional Gauss–Bonnet black holes in asymptotically de Sitter space time: Scalar, electromagnetic and Dirac perturbations. *Eur. Phys. J. C* **2020**, *80*, 760. [CrossRef]
182. Gundlach, C.; Price, R.H.; Pullin, J. Late time behavior of stellar collapse and explosions: 1. Linearized perturbations. *Phys. Rev. D* **1994**, *49*, 883–889. [CrossRef] [PubMed]
183. Skvortsova, M. Ringing of extreme regular black holes. *Gravit. Cosmol.* **2024**, *30*, 279–288. [CrossRef]
184. Bolokhov, S.V. Late time decay of scalar and Dirac fields around an asymptotically de Sitter black hole in the Euler–Heisenberg electrodynamics. *Eur. Phys. J. C* **2024**, *84*, 634. [CrossRef]
185. Guo, W.D.; Tan, Q.; Liu, Y.X. Quasinormal modes and greybody factor of a Lorentz-violating black hole. *J. Cosmol. Astropart. Phys.* **2024**, *7*, 8. [CrossRef]
186. Yang, Z.H.; Xu, C.; Kuang, X.M.; Wang, B.; Yue, R.H. Echoes of massless scalar field induced from hairy Schwarzschild black hole. *Phys. Lett. B* **2024**, *853*, 138688. [CrossRef]
187. Baruah, A.; Övgün, A.; Deshamukhya, A. Quasinormal modes and bounding greybody factors of GUP-corrected black holes in Kalb–Ramond gravity. *Ann. Phys.* **2023**, *455*, 169393. [CrossRef]
188. Shao, C.Y.; Zhang, C.; Zhang, W.; Shao, C.G. Scalar fields around a loop quantum gravity black hole in de Sitter spacetime: Quasinormal modes, late-time tails and strong cosmic censorship. *Phys. Rev. D* **2024**, *109*, 064012. [CrossRef]
189. Hamil, B.; Lütfüoğlu, B. Thermodynamics and Shadows of quantum-corrected Reissner–Nordström black hole surrounded by quintessence. *Phys. Dark Universe* **2023**, *42*, 101293. [CrossRef]
190. Araújo Filho, A.A.; Jusufi, K.; Cuadros-Melgar, B.; Leon, G.; Jawad, A.; Pellicer, C. Charged black holes with Yukawa potential. *Phys. Dark Universe* **2024**, *46*, 101711. [CrossRef]
191. Zeng, X.X.; Li, G.P.; He, K.J. The shadows and observational appearance of a noncommutative black hole surrounded by various profiles of accretions. *Nucl. Phys. B* **2022**, *974*, 115639. [CrossRef]
192. Araújo Filho, A.A. Remarks on a nonlinear electromagnetic extension in AdS Reissner-Nordström spacetime. *J. Cosmol. Astropart. Phys.* **2025**, *2025*, 72. [CrossRef]
193. Ball, D.; Chen, S.; Jing, J.; Qian, W.; Wang, B. Black hole images: A review. *Sci. China Phys. Mech. Astron.* **2023**, *66*, 260401. [CrossRef]
194. Gralla, S.E. Can the EHT M87* results be used to test general relativity. *Phys. Rev. D* **2021**, *103*, 024023. [CrossRef]
195. Akiyama, K. et al. [Event Horizon Telescope Collaboration] First M87* event horizon telescope results. V. Physical origin of the asymmetric ring. *Astrophys. J. Lett.* **2019**, *875*, L5. [CrossRef]
196. Gibbons, G.W.; Werner, M.C. Applications of the Gauss-Bonnet theorem to gravitational lensing. *Class. Quantum Gravity* **2008**, *25*, 235009. [CrossRef]
197. Qiao, C.K.; Li, M. Geometric approach to circular photon orbits and black hole shadows. *Phys. Rev. D* **2022**, *106*, L021501. [CrossRef]
198. Heidari, N.; Araújo Filho, A.A.; Lobo, I.P. Non-commutativity in Hayward spacetime. *arXiv* **2025**, arXiv:2503.17789.
199. Qiao, C.K. Curvatures, photon spheres, and black hole shadows. *Phys. Rev. D* **2022**, *106*, 084060. [CrossRef]
200. Araújo Filho, A.A.; Heidari, N.; Reis, J.A.A.S.; Hassanabadi, H. The impact of an antisymmetric tensor on charged black holes: Evaporation process, geodesics, deflection angle, scattering effects and quasinormal modes. *Class. Quantum Gravity* **2025**, *42*, 065026. [CrossRef]
201. Qiao, C.K. The Existence and Distribution of Photon Spheres Near Spherically Symmetric Black Holes—A Geometric Analysis. *arXiv* **2024**, arXiv:2407.14035.
202. Araújo Filho, A.A.; Heidari, N.; Lobo, I.P.; Shi, Y. Optical Phenomena in a Non-Commutative Kalb-Ramond Black Hole Spacetime. *arXiv* **2025**, arXiv:2508.08889.
203. Araújo Filho, A.A.; Nascimento, J.R.; Petrov, A.Y.; Porfírio, P.J.; Övgün, A. Effects of non-commutative geometry on black hole properties. *Phys. Dark Universe* **2024**, *46*, 101630. [CrossRef]

204. Araújo Filho, A.A.; Heidari, N.; Övgün, A. Geodesics, accretion disk, gravitational lensing, time delay, and effects on neutrinos induced by a non-commutative black hole. *J. Cosmol. Astropart. Phys.* **2025**, *2025*, 62. [CrossRef]
205. Heidari, N.; Araújo Filho, A.A.; Pantig, R.C.; Övgün, A. Absorption, scattering, geodesics, shadows and lensing phenomena of black holes in effective quantum gravity. *Phys. Dark Universe* **2025**, *47*, 101815. [CrossRef]
206. Tsukamoto, N. Deflection angle in the strong deflection limit in a general asymptotically flat, static, spherically symmetric spacetime. *Phys. Rev. D* **2017**, *95*, 064035. [CrossRef]
207. Hasse, W.; Perlick, V. Gravitational lensing in spherically symmetric static spacetimes with centrifugal force reversal. *Gen. Rel. Grav.* **2002**, *34*, 415–433. [CrossRef]
208. Akiyama, K. et al. [Event Horizon Telescope Collaboration] First Sagittarius A* Event Horizon Telescope results. IV. Variability, morphology, and black hole mass. *Astrophys. J. Lett.* **2022**, *930*, L15. [CrossRef]
209. Akiyama, K. et al. [Event Horizon Telescope Collaboration] First Sagittarius A* event horizon telescope results. VI. Testing the black hole metric. *Astrophys. J. Lett.* **2022**, *930*, L17. [CrossRef]
210. Perlick, V.; Tsupko, O.Y. Calculating black hole shadows: Review of analytical studies. *Phys. Rep.* **2022**, *947*, 1–39. [CrossRef]
211. Kumar, R.; Ghosh, S.G. Rotating black holes in 4D Einstein-Gauss-Bonnet gravity and its shadow. *J. Cosmol. Astropart. Phys.* **2020**, *2020*, 53. [CrossRef]
212. Xu, M.; Li, R.; Lu, J.; Yang, S.; Wu, S.M. Optical appearance and shadow of Kalb–Ramond black hole: Effects of plasma and accretion models. *Eur. Phys. J. C* **2025**, *85*, 676. [CrossRef]
213. Heydari-Fard, M. Effect of quintessence dark energy on the shadow of Hayward black holes with spherical accretion. *Indian J. Phys.* **2024**, *98*, 3019–3032. [CrossRef]
214. Blakeslee, J.P.; Jordán, A.; Mei, S.; Côté, P.; Ferrarese, L.; Infante, L.; Peng, E.W.; Tonry, J.L.; West, M.J. The ACS Fornax cluster survey. V. Measurement and recalibration of surface brightness fluctuations and a precise value of the Fornax–Virgo relative distance. *Astrophys. J.* **2009**, *694*, 556. [CrossRef]
215. Gebhardt, K.; Adams, J.; Richstone, D.; Lauer, T.R.; Faber, S.; Gültekin, K.; Murphy, J.; Tremaine, S. The black hole mass in M87* from Gemini/NIFS adaptive optics observations. *Astrophys. J.* **2011**, *729*, 119. [CrossRef]
216. Bird, S.; Harris, W.E.; Blakeslee, J.P.; Flynn, C. The inner halo of M87*: A first direct view of the red-giant population. *Astron. Astrophys.* **2010**, *524*, A71. [CrossRef]
217. Akiyama, K. et al. [Event Horizon Telescope Collaboration] First M87* event horizon telescope results. VI. The shadow and mass of the central black hole. *Astrophys. J. Lett.* **2019**, *875*, L6. [CrossRef]
218. Abuter, R. et al. [GRAVITY Collaboration] Mass distribution in the Galactic Center based on interferometric astrometry of multiple stellar orbits. *Astron. Astrophys.* **2022**, *657*, L12. [CrossRef]
219. Abuter, R. et al. [GRAVITY Collaboration] Detection of the Schwarzschild precession in the orbit of the star S2 near the Galactic centre massive black hole. *Astron. Astrophys.* **2020**, *636*, L5. [CrossRef]
220. Banerjee, I.; Sau, S.; SenGupta, S. Do shadows of Sgr A* and M87* indicate black holes with a magnetic monopole charge? *arXiv* **2022**, arXiv:2207.06034.
221. Amelino-Camelia, G. Quantum-Spacetime Phenomenology. *Living Rev. Rel.* **2013**, *16*, 5. [CrossRef] [PubMed]
222. Casana, R.; Cavalcante, A.; Poulis, F.P.; Santos, E.B. Exact Schwarzschild-like solution in a bumblebee gravity model. *Phys. Rev. D* **2018**, *97*, 104001. [CrossRef]
223. Yang, K.; Chen, Y.Z.; Duan, Z.Q.; Zhao, J.Y. Static and spherically symmetric black holes in gravity with a background Kalb-Ramond field. *Phys. Rev. D* **2023**, *108*, 124004. [CrossRef]
224. Goldstein, H.; Poole, C.; Safko, J. *Classical Mechanics*, 3rd ed.; Addison-Wesley: San Francisco, CA, USA, 2002.
225. Lambert, S.; Le Poncin-Lafitte, C. Improved determination of γ by VLBI. *Astron. Astrophys.* **2011**, *529*, A70. [CrossRef]
226. Shapiro, I.I. Fourth Test of General Relativity. *Phys. Rev. Lett.* **1964**, *13*, 789–791. [CrossRef]
227. Wang, R.B.; Ma, S.J.; Deng, J.B.; Hu, X.R. Estimating the strength of Lorentzian distribution in non-commutative geometry by solar system tests. *arXiv* **2024**, arXiv:2411.06628.
228. Bertotti, B.; Iess, L.; Tortora, P. A test of general relativity using radio links with the Cassini spacecraft. *Nature* **2003**, *425*, 374–376. [CrossRef] [PubMed]
229. Will, C.M. The confrontation between general relativity and experiment. *Living Rev. Relativ.* **2014**, *17*, 1–117. [CrossRef] [PubMed]
230. Araújo Filho, A.A.; Furtado, J.; Reis, J.A.A.S.; Silva, J.E.G. Thermodynamical properties of an ideal gas in a traversable wormhole. *Class. Quantum Gravity* **2023**, *40*, 245001. [CrossRef]
231. Furtado, J.; Hassanabadi, H.; Reis, J.A.A.S. Thermal analysis of photon-like particles in rainbow gravity. *arXiv* **2023**, arXiv:2305.08587.
232. Araújo Filho, A.A.; Reis, J.A.A.S. How does geometry affect quantum gases? *Int. J. Mod. Phys. A* **2022**, *37*, 2250071. [CrossRef]
233. Araújo Filho, A.A.; Reis, J.A.A.S.; Övgün, A. Modified particle dynamics and thermodynamics in a traversable wormhole in bumblebee gravity. *Eur. Phys. J. C* **2025**, *85*, 83. [CrossRef]

234. Araújo Filho, A.A. Particle creation and evaporation in Kalb-Ramond gravity. *J. Cosmol. Astropart. Phys.* **2025**, *2025*, 76. [CrossRef]
235. Araújo Filho, A.A. Particle production induced by a Lorentzian non–commutative spacetime. *Ann. Phys.* **2025**, *481*, 170167. [CrossRef]

Disclaimer/Publisher's Note: The statements, opinions and data contained in all publications are solely those of the individual author(s) and contributor(s) and not of MDPI and/or the editor(s). MDPI and/or the editor(s) disclaim responsibility for any injury to people or property resulting from any ideas, methods, instructions or products referred to in the content.